Ultrafast Coherent Diffractive Imaging of Nano-Scale Dynamics Using High Harmonic Sources

by

Robert Maurice Karl, Jr.

B.S., Rochester Institute of Technology, 2014

M.S., University of Colorado Boulder, 2017

A thesis submitted to the

Faculty of the Graduate School of the

University of Colorado in partial fulfillment

of the requirements for the degree of

Doctor of Philosophy

Department of Physics

2019

This thesis entitled:
Ultrafast Coherent Diffractive Imaging of Nano-Scale Dynamics Using High Harmonic Sources
written by Robert Maurice Karl, Jr.
has been approved for the Department of Physics

_____
Prof. Margaret Murnane

_____
Prof. Henry Kapteyn

Date _____

The final copy of this thesis has been examined by the signatories, and we find that both the content and the form meet acceptable presentation standards of scholarly work in the above mentioned discipline.

Karl, Jr., Robert Maurice (Ph.D., Physics)

Ultrafast Coherent Diffractive Imaging of Nano-Scale Dynamics Using High Harmonic Sources

Thesis directed by Prof. Margaret Murnane

Imaging at the nano-scale is increasingly important for a host of applications. In order to fully characterize nano-scale processes, their dynamics must be studied at their characteristic length and time scales. When harnessed with coherent diffractive imaging techniques, especially ptychography, extreme ultraviolet light can image these processes at these scales.

This thesis extends ptychography to a higher throughput modality by developing the technique of multiple beam ptychography. This is first demonstrated with beams of different wavelengths, and then with beams of different polarization states. This allows for large field of view imaging and for simultaneous polarization resolved imaging. This thesis then develops these techniques for the case of beams of the same wavelength and polarization by leveraging the aliasing of the measured signal.

Colloidal crystals are important as templates for inverse lattice materials. These crystals are measured using newly developed small angle extreme ultraviolet scattering techniques and ptychographic imaging. These measurements reveal the local and extended symmetries present in the crystal arrangement paving the way for full characterization of novel materials.

Finally, full-field, time-resolved imaging is performed, harnessing the ultrafast nature of high harmonic generation. 10 fs temporal resolution, 100 nm transverse spatial resolution, and 50 pm axial resolution are attained by combining ptychography imaging with pump-probe spectroscopy. This time-resolved microscope directly images acoustic waves traveling in isolated nano-structures. The thermal and acoustic dynamics of these nano-structures are measured. This new capability for measurement at the nano-scale allows for previously impossible measurements of novel materials.

Dedication

To my partner, Michelle Poirier.

Acknowledgements

I have had the benefit of spending the past few years among some of the most intelligent, interesting, and insightful people I've ever met. Margaret Murnane and Henry Kapteyn have been such incredible advisors. No matter what guidance I've needed, they've provided it. The KM group has been such a supportive home. I want to thank the entire KM imaging team: Daniel Adams, Dennis Gardner, Elisabeth Shanblatt, Giulia Mancini, Bosheng Zhang, Matt Seaberg, Christina Porter, Michael Tanksalvala, Charlie Bevis, Bin Wang, Peter Johnsen, Yuka Esashi, Guan Gui, Zhe 'Joe' Zhang, Jeremy Thurston, Nick Jenkins, Chen-Ting Liao, Emma Cating-Subramanian, Michael Gerrity, and Michael Hemmer. I can't list them all, but I want to thank some others in the KM group: Josh Knobloch, Christian Gentry, Travis Frazer, Begoña Abad, and Nico Hernandez-Charpak. I'm grateful to my collaborators for their help and their samples. From Penn State: Jennifer Russel, Thomas Mallouk, and John Badding. From NIST: Hans Nembach, Justin Shaw, and Thomas Silva. From UCLA: Mike Lo, Arjun Rana, and John Miao. From CU Boulder: Omar Khatib, Eric Muller, Jun Nishida, and Markus Raschke. The STROBE community has given me many opportunities that I wouldn't have thought to seek. Thanks to Tess Eidem, Lauren Mason, Ellen Keister, and Sarah Schreiner for making these opportunities a reality. Both near and far, my friends of Left Right TIM have had my back over these five years. I want to thank my undergraduate mentors, especially Michael Pierce, for guiding me and believing in me. My family, who have always supported and believed in me, I cannot thank you enough for all you've done. Finally, Michelle Poirier, my love: thank you for always being by my side.

Contents

Chapter

Tables

Table

Figures

Figure

Chapter 1

Introduction

Progress in the fields of nano-fabrication and materials science has paved the way for new breeds of materials with exotic behaviors. These may be familiar materials that exhibit new phenomena when patterned at the nano-scale, or they may be materials with nano-scopic features, the geometry of which manifests itself in novel dynamics. In order to understand the function of these nano-scale materials, it is necessary to measure them at their natural length and time scales. For these systems, those length scales are sub-100 nm and the time scales are on the order of picoseconds down to femtoseconds. In this thesis, the development of an ultrafast, time-resolved microscope with sub-100 nm resolution is reported. This dynamic microscope is then used to study nano-scale systems. This microscope uses extreme ultraviolet (EUV) light created through the process of high harmonic generation (HHG). The wavelength of this light, 30 nm, is ideally suited for probing sub-100 nm features. More importantly, the temporal duration of these pulses, 10 fs, allows for deeply sub-ps time resolution. Because this microscope uses EUV light, it cannot use a traditional, lens based imaging system. Instead, it is a computational microscope employing coherent diffractive imaging algorithms to form an image from diffraction measurements. Repeatable dynamics are then induced and measured using a pump-probe technique.

This thesis is organized as follows. An introduction to coherent diffractive imaging, culminating in a discussion of ptychography is presented in chapter 2. In chapter 3, ptychography with multiple wavelengths is shown, along with its application towards multiple

beam ptychography. The extension of multiple beam ptychography to use identical beams of the same wavelength is developed in chapter 4. The process of high harmonic generation is the subject of chapter 5. The application of a high harmonic source to study colloidal crystals using ptychography and scatterometry is presented in chapter 6. The development and characterization of the time resolved EUV microscope, and an experiment measuring nano-antennas is contained in chapter 7. This thesis concludes with future outlook in chapter 8.

1.1 The Theory of Diffraction

In this section, the basic elements of diffraction theory are derived. The interested reader is directed towards [82, 105], from which these derivations are adapted, for a more detailed treatment.

1.1.1 Maxwell's Equations and the Wave Equation

Since light is fundamentally an electromagnetic wave, its behavior can be described through electromagnetic theory. This theory is captured by the equations of Maxwell.

$$\vec{\nabla} \cdot \vec{B} = 0 \tag{1.1}$$

$$\vec{\nabla} \cdot \vec{D} = \rho \tag{1.2}$$

$$\vec{\nabla} \times \vec{E} = -\frac{\partial \vec{B}}{\partial t} \tag{1.3}$$

$$\vec{\nabla} \times \vec{H} = \vec{j} + \frac{\partial \vec{D}}{\partial t} \tag{1.4}$$

In these equations, $\vec{E}$ and $\vec{D}$ are representations of the electric field, $\vec{B}$ and $\vec{H}$ of the magnetic field, ρ are free charges, and $\vec{j}$ are free currents. In a linear dielectric, the different fields are related through the permittivity (ϵ) and permeability (μ) of the material.

$$\vec{D} = \epsilon \vec{E} \tag{1.5}$$

$$\vec{B} = \mu \vec{H} \tag{1.6}$$

From these equations, the behavior of light can be derived. Taking the curl of Faraday's Law (Equation 1.3) yields

$$\vec{\nabla} \times \vec{\nabla} \times \vec{E} = -\vec{\nabla} \times \frac{\partial \vec{B}}{\partial t} \tag{1.7}$$

Using the following vector identity, this expression can be simplified.

$$\vec{\nabla} \times \vec{\nabla} \times \vec{A} = \vec{\nabla}(\vec{\nabla} \cdot \vec{A}) - \vec{\nabla}^2 \vec{A} \tag{1.8}$$

Applying this identity to the curl of Faraday's law and reversing the order of the curl and time derivative on the right hand side yields

$$\vec{\nabla}(\vec{\nabla} \cdot \vec{E}) - \vec{\nabla}^2 \vec{E} = -\frac{\partial \vec{\nabla} \times \vec{B}}{\partial t} \tag{1.9}$$

The curl of the magnetic field is present in Ampere's Law (Equation 1.4), and thus may be substituted. Likewise, the divergence of the electric field is present in Gauss's Law (Equation 1.2). Applying these substitutions yields the following.

$$\frac{1}{\epsilon}\vec{\nabla}\rho - \vec{\nabla}^2 \vec{E} = -\mu \frac{\partial \vec{j}}{\partial t} - \mu \frac{\partial^2 \vec{D}}{\partial t^2} \tag{1.10}$$

For the case propagation through vacuum, which is the condition under which the work in this thesis is performed, the permittivity and permeability simplify to those of free space. The absence of free changes and free currents allows for further simplification. Applying these conditions, the above expression simplifies to a wave equation.

$$\vec{\nabla}^2 \vec{E} - \mu_0 \epsilon_0 \frac{\partial^2 \vec{E}}{\partial t^2} = 0 \tag{1.11}$$

For these waves, the wave velocity is given by

$$v = \sqrt{\frac{1}{\mu_0 \epsilon_0}} = c \tag{1.12}$$

which is the speed of light in vacuum.

This derivation can be repeated beginning with the curl of Ampere's Law (Equation 1.4) and proceeding in an identical manner. This results in a wave equation for the magnetic field. While the rest of this section will deal with the electric field, the results therein are equally applicable to the magnetic field.

1.1.2 The Helmholtz Equation

The wave equation (Equation 1.11) is separable in time. For a single wavelength of light the solution to the wave equation may be written as

$$\vec{E}(\vec{r},t) = \vec{E}(\vec{r})e^{i(\omega t+\phi)} \tag{1.13}$$

where ω is the frequency of the wave, and ϕ is an arbitrary, time independent phase. Substituting this solution into the wave equation yields a simpler equation that governs the time independent portion of the solution.

$$\vec{\nabla}^2\vec{E} + \mu_0\epsilon_0\omega^2\vec{E} = 0 \tag{1.14}$$

This can be rewritten in terms of the wavevector $k = \frac{2\pi}{\lambda}$ to realize the Helmholtz equation

$$\vec{\nabla}^2\vec{E} + k^2\vec{E} = 0 \tag{1.15}$$

For a polychromatic treatment of the wave equation, a Fourier series of different wavelengths is more appropriate. However, it will suffice for the work in this thesis to consider multiple wavelengths of light as orthogonal modes as the interactions between the different wavelengths are too fast to be measured by modern detectors.

This Helmholtz equation is a vector equation, yet it is also separable. As such, each vector component of the electric and magnetic fields also obeys the scalar Helmholtz equation. Because of this, future treatment of the Helmholtz equation will use the scalar version, using the variable U as a stand-in for any of the components of the field.

1.1.3 Kirchhoff Diffraction Theory

In order to work with the Helmholtz equation (Equation 1.15), it is beneficial to make use of Green's theorem.

$$\iiint_V \left(U\vec{\nabla}^2G - G\vec{\nabla}^2U\right)dv = \iint_S \left(U\frac{\partial G}{\partial n} - G\frac{\partial U}{\partial n}\right)ds \tag{1.16}$$

In this expression, n is the outward normal vector at each point on the surface S, which contains the volume V, and G is a Green's function of the differential equation. This Green's function is the response function to a point source. In the case of the Helmholtz equation it can be chosen to be a unit amplitude spherical wave

$$G(P_0) = \frac{e^{ikr_{01}}}{r_{01}} \tag{1.17}$$

where P_0 is the point at which the field is calculated, P_1 is the location of a point source, and r_{01} is the distance between these points.

Since both U and G are solutions to the Helmholtz equation, the Laplacians in the left hand side of Green's theorem (Equation 1.16) can be substituted, resulting in the entire volume integral being equal to zero. This leaves the remaining expression

$$0 = \iint_S \left(U\frac{\partial G}{\partial n} - G\frac{\partial U}{\partial n} \right) ds \tag{1.18}$$

Notably, the choice of Green's function is not continuous at the point P_0. This issue is addressed by constructing the surface S so that it contains a spherical shell surrounding the point P_0 of radius ϵ. The limit as ϵ approaches zero is taken so that only the point P_0 is excluded from consideration. The result of this is that an additional term of $4\pi U(P_0)$ is present from the integral. With the inclusion of this consideration, the integral theorem of Helmholtz and Kirchhoff is reached.

$$U(P_0) = \frac{1}{4\pi} \iint_S \left(G\frac{\partial U}{\partial n} - U\frac{\partial G}{\partial n} \right) ds \tag{1.19}$$

Boundary conditions must be applied to this equation in order to solve for the measured field. It is convenient to consider a plane upon which the field is defined within an aperture and zero outside of the aperture. For this configuration, the surface S can be deformed so that it lies along this plane on one side and forms a hemisphere on the other side, with this hemisphere extending out to infinity. Thus the surface S can be considered as two parts: the plane (S_1) and the hemisphere (S_2). This surface is shown, in two dimensions, in figure 1.1, but should be thought of as the three-dimensional extension of this sketch.

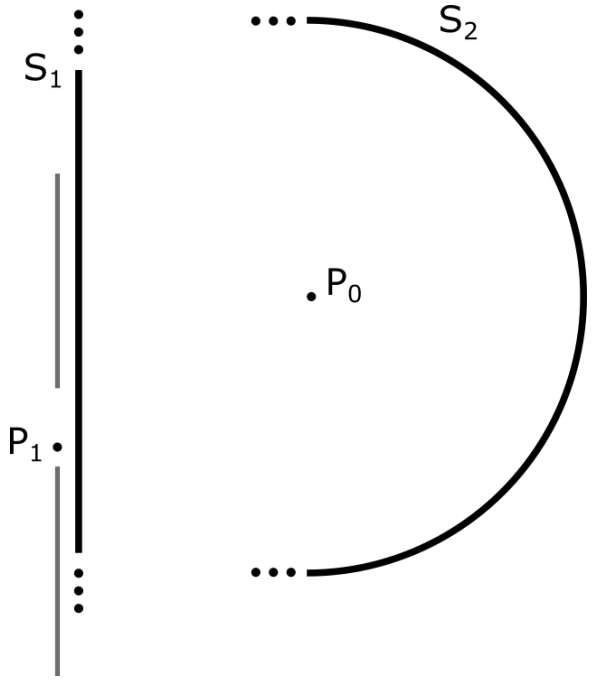

Figure 1.1: Surface for the Helmholtz Equation Boundary Conditions. The boundary conditions for the Helmholtz equation are applied to this surface. The left side of the surface is the plane S_1, which coincides with an aperture. The right hand side of the surface, S_2, is an infinite hemisphere centered at the point of observation, P_0.

Considering only the contribution from the hemisphere, the Green's function and its derivative can be evaluated directly.

$$G(S_2) = \frac{e^{ikR}}{R} \tag{1.20}$$

$$\frac{\partial G(S_2)}{\partial n} = \left(ik - \frac{1}{R}\right)\frac{e^{ikR}}{R} \tag{1.21}$$

where R is the radius of the hemisphere. The contribution from the hemisphere to the Helmholtz equation is given by the following.

$$\frac{1}{4\pi}\iint_{S_2}\left(G\frac{\partial U}{\partial n} - U\frac{\partial G}{\partial n}\right)ds = \frac{1}{4\pi}\int_{\Omega}\left(G\frac{\partial U}{\partial n} - UikG\right)R^2 d\omega \tag{1.22}$$

where Ω is the solid angle subtended by the hemisphere. In order for this integral to be zero, it is required that the integrand vanish sufficiently fast. This condition is met if there are only outgoing waves incident on S_2, which is precisely the scenario. Thus the only portion of the Helmholtz equation remaining is on the plane boundary, S_1.

$$U(P_0) = \frac{1}{4\pi}\iint_{S_1}\left(\frac{\partial U}{\partial n}G - U\frac{\partial G}{\partial n}\right)ds \tag{1.23}$$

1.1.4 Rayleigh-Sommerfeld Diffraction Theory

In order to properly assert boundary conditions on the plane, it is not sufficient to define part of the plane to have both U and its derivative equal to zero. Instead, a slightly different Green's function may be used

$$G_-(P_1) = \frac{e^{ikr_{01}}}{r_{01}} - \frac{e^{ik\tilde{r}_{01}}}{\tilde{r}_{01}} \tag{1.24}$$

In this expression the tilde makes reference to a point $\tilde{P}_0$, which is the mirror image of P_0 reflected over the plane S_1. These points are shown in figure 1.2. On the surface S_1, this new Green's function is identically zero, though its derivative is not. Because of this, the boundary condition on the Helmholtz equation can be applied without inconsistency. Satisfying this boundary condition gives this expression, known as the First Rayleigh-Sommerfeld solution.

$$U(P_0) = \frac{1}{4\pi}\iint_{S_1}\left(-U\frac{\partial G_-}{\partial n}\right)ds \tag{1.25}$$

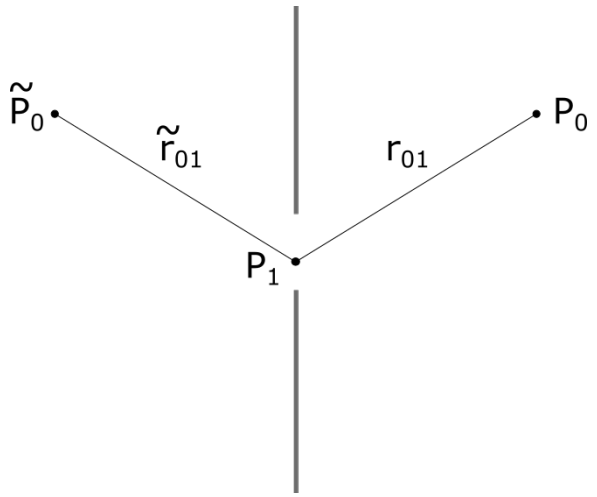

Figure 1.2: Geometry for Rayleigh-Sommerfeld Green's Function. The point P_0 is mirrored about the boundary plane to create the point $\tilde{P}_0$. The distance between these points and a given point on the plane, P_1 is given by r_{01} and $\tilde{r}_{01}$, respectively.

The Second Rayleigh-Sommerfeld solution is obtained by taking a summation of two point sources to form the Green's function instead of the difference. The two results are similar in the case of far-field diffraction, which will suffice for the work in this thesis. Thus, only the first solution will be considered here.

The derivative of the Green's function is exactly given by

$$\frac{\partial G_-}{\partial n} = 2\cos\left(n, \vec{r}_{01}\right)\left(ik - \frac{1}{r_{01}}\right)\frac{e^{ikr_{01}}}{r_{01}} \tag{1.26}$$

where the cosine is the cosine of the angle between the two vectors. For simplicity, the point of observation, P_0 is taken to be multiple wavelengths distant from the boundary so that the $\frac{1}{r_{01}}$ term may be neglected. Under this approximation, the expression for the measured field is

$$U(P_0) = \frac{1}{i\lambda}\iint_{S_1}\left(U(P_1)\frac{e^{ikr_{01}}}{r_{01}}\cos\left(\vec{n}, \vec{r}_{01}\right)\right)ds \tag{1.27}$$

This is the Rayleigh-Sommerfeld diffraction formula.

1.1.5 Fresnel Diffraction

A useful approximation to the Rayleigh-Sommerfeld diffraction formula is the near-field, or Fresnel, approximation. This approximation requires that the point of observation be sufficiently far from the boundary. To arrive at this approximation, the Rayleigh-Sommerfeld formula is first cast into Cartesian coordinates. Two planes are described in this way: the boundary plane (S_1) which has coordinates ξ and η, and the observation plane (the plane containing P_0) which has coordinates x and y. The two planes are separated by some distance z. These coordinate systems are shown in figure 1.3

In this coordinate system the cosine term can be written simply.

$$\cos\left(\vec{n}, \vec{r}_{01}\right) = \frac{z}{r_{01}} \tag{1.28}$$

The quantity r_{01} can be written explicitly in this coordinate system.

$$r_{01} = \sqrt{z^2 + (x-\xi)^2 + (y-\eta)^2} \tag{1.29}$$

This expression can be simplified using a binomial expansion in the limit that z is much larger than any of the lateral dimensions. Under this approximation, the Rayleigh-Sommerfeld formula simplifies to

$$U(x,y) = \frac{e^{ikz}}{i\lambda z} e^{\frac{i\pi}{\lambda z}\left(x^2+y^2\right)} \mathcal{F}_{\frac{x}{\lambda z}, \frac{y}{\lambda z}} \left(U(\xi,\eta) e^{\frac{i\pi}{\lambda z}\left(\xi^2+\eta^2\right)} \right) \tag{1.30}$$

where the Fourier transform is from the (ξ,η) coordinates to new coordinates ($\frac{x}{\lambda z}$,$\frac{y}{\lambda z}$). The matter of determining the field given the field at a boundary is now reduced to computing a single Fourier transform with the inclusion of quadratic phase terms. This is known as Fresnel diffraction, and it is this approximation that will be used for the propagation of light throughout the course of this thesis.

1.1.6 Fraunhofer Diffraction

It is worth noting that in the far-field, the diffraction computation becomes yet simpler. In the limit of extremely large z compared to the aperture size, the quadratic phase becomes

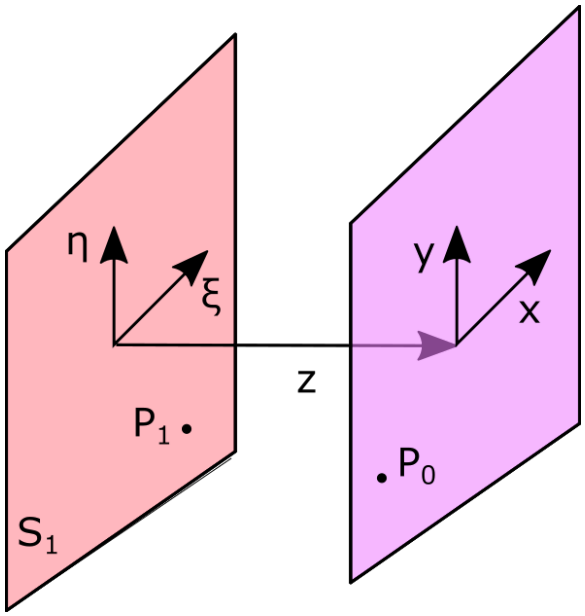

Figure 1.3: Fresnel Diffraction Coordinate System. These are the planes used to define coordinates for the case of Fresnel diffraction. The (ξ,η) plane is the plane where boundary conditions are imposed. The (x,y) plane is where the resulting field is observed. The two planes are separated by the propagation distance z.

negligible.

$$z >> \frac{k(\xi^2 + \eta^2)}{2} \tag{1.31}$$

This leads to the relationship between the boundary field and the far-field to be governed by a single Fourier transform.

$$U(x,y) = \frac{e^{ikz}}{i\lambda z} e^{\frac{i\pi}{\lambda z}\left(x^2+y^2\right)} \mathcal{F}_{\frac{x}{\lambda z},\frac{y}{\lambda z}}\left(U(\xi,\eta)\right) \tag{1.32}$$

1.2 Imaging with X-rays

Since the discovery of x-rays in the 1800's [196], their ability to penetrate objects has been noted and exploited. The ability to form an image using x-rays is useful for studying the internal structure of objects. Furthermore, the short wavelength of x-rays allows for extremely high resolution imaging. The inherent ability of x-rays to pass through objects unimpeded has the disadvantage of making it difficult to build a lens with which to form an image. In this section, various methods to circumvent this challenge are reviewed. For a more detailed review, the reader is directed towards these review articles [33, 200].

1.2.1 Refractive Optics

The index of refraction for most materials is less than unity for x-rays, thus a conventional lens design would not yield a powerful enough lens to focus an x-ray beam, let alone form an image. Yet since the index of refraction is not exactly one, a refractive optic can still be formed. A compound refractive lens [23, 218, 219] is a solid object with a series of spherical holes inside of it. Between each of these holes, the remaining solid mass forms a concave lens. Since the index of refraction of this material is less than unity, the concave lens focuses the x-ray beam. By having a series of these holes, the focusing power of the optic is made stronger. These optics are effective for focusing high energy x-rays that are not readily absorbed by materials, but they are not feasible for lower energy x-rays and extreme ultraviolet light because the absorption of the light is too strong.

A different approach to using the index of refraction of materials to form a focusing optic is the capillary x-ray lens [121]. A bundle of glass capillaries redirect the light using total external reflection within the capillary. The capillaries are then curved so as to redirect the light to one point. This optic is useful for focusing an x-ray beam, but does not form an image, so it cannot serve as an image forming optic. However, it can be used within an x-ray microscope [255].

1.2.2 Reflective Optics

A variety of x-ray optics can be made using reflective optics. Schwarzschild telescopes [207] have been used at synchrotron facilities to achieve focusing of x-ray beams [28]. These operate with a pair of normal incidence reflective mirrors that first expand the beam, and then focus the beam with a higher numerical aperture afforded by the initial expansion.

Most reflective x-ray optics operate near grazing incidence because the reflectivity of materials to x-rays is higher closer to grazing [93]. KB mirrors, named after inventors Kirkpatrick and Baez [114], use a pair of near grazing curved mirrors. Each of these mirrors focuses the beam in one dimension. The resulting beam is focused in both dimensions and has some amount of astigmatism.

Other two mirror designs were developed by Wolter that use parabolic, hyperbolic, and ellipsoidal mirrors in combination to achieve a focusing telescope with only grazing incidence optics [252].

1.2.3 Diffractive Optics

While x-rays do not refract much on interaction with matter, coherent x-rays will diffract. This diffraction can be exploited by careful design to cause constructive interference in only one location, i.e. focusing the beam. This can be achieved using a Fresnel zone plate [12, 254]. A zone plate is a transmissive optic with alternating transparent and opaque annuli. The radii of these annuli are determined based upon interference. All of the radii

for which transmitted light would destructively interfere are prevented from transmitting, whereas the light that will constructively interfere is permitted. For the simplified case of focusing a plane wave, the radii at which the transmission of the zone plate changes are given by the following equation [8].

$$r_n^2 = n\lambda\left(f + \frac{n\lambda}{4}\right) \tag{1.33}$$

where f is the focal length of the zone plate.

In order to achieve maximum resolution, the zone plate must be as large as possible while still retaining high quality fabrication in the outer-most ring. The zone plate forms images directly [171, 205], much in the same way that a lens does for visible light. Sufficiently high quality zone plates enable high resolution x-ray imaging [30].

A different type of diffractive optic that addresses these fabrication challenges is the Laue lens [43, 107, 152]. A Laue lens is a one-dimensional analog to the Fresnel zone plate. An alternating stack of thin films are deposited in accordance to the Fresnel zone plate geometry, to obtain the same focusing. By combining two orthogonally oriented Laue lenses, the beam can be fully focused in two dimensions.

1.2.4 Scanning Transmission X-Ray Microscopy

Some of the above focusing optics can be used to directly form an image using x-ray light. Others, however, do not form an image directly, but only focus the beam. These latter focusing optics are still useful in image formation. A specific imaging modality that makes use of these is scanning transmission x-ray microscopy [115, 186]. In this modality, the beam is focused through an aperture and scanned across the sample. At each scan position, the amount of light transmitted through the sample is measured. These measurements each represent one pixel in the resulting image.

1.2.5 Fourier Transform Holography

It is possible to make use of the diffraction of coherent x-rays to circumvent the need for a focusing optic altogether. The technique of Fourier transform holography [155] makes use of a reference beam that is spatially separated from the sample of interest. The interference between the exit surface wave from the sample and the reference is measured along with the intensity of each. Taking a Fourier transform of the resulting intensity will spatially separate the autocorrelation of the sample and the reference from the cross-correlation of the two. By choosing the reference to be similar to a delta function, this cross-correlation reduces to the complex field of the sample's exit surface wave, thus yielding an image of the sample.

1.2.6 Transport of Intensity

Complex images can also be formed through exploitation of the transport of intensity equation. This equation is a consequence of the Helmholtz equation (Equation 1.15) under the paraxial approximation (Equation 1.34).

$$\frac{\partial^2 U}{\partial z^2} \approx 2ik\frac{\partial U}{\partial z} - k^2 U \tag{1.34}$$

Under this approximation, the Helmholz equation is given by the following

$$2ik\frac{\partial U}{\partial z} + \vec{\nabla}_\perp^2 U = 0 \tag{1.35}$$

The field can be expressed in terms of the intensity and phase explicitly ($U = \sqrt{I}e^{i\phi}$), and the transverse derivatives can be calculated. Once done, the real and imaginary terms of that expression can be separated (owing to the fact that k, I, and ϕ must be real over all space). This yields these two equations

$$-4kI\frac{\partial \phi}{\partial z} - \frac{1}{2}\frac{\vec{\nabla} I \cdot \vec{\nabla} I}{I} + \vec{\nabla}^2 I - 2I\vec{\nabla}\phi \cdot \vec{\nabla}\phi = 0 \tag{1.36}$$

$$2ik\frac{\partial I}{\partial z} + 2i\vec{\nabla}\phi \cdot \vec{\nabla} I + 2i\vec{\nabla}^2\phi = 0 \tag{1.37}$$

The imaginary equation can be rewritten as the transport of intensity equation (Equation 1.38) [224, 229].

$$-k\frac{\partial I}{\partial z} = \vec{\nabla}\cdot\left(I\vec{\nabla}\phi\right) \tag{1.38}$$

In the scenario where I is uniform, the case of a phase only object, the right hand side of the equation simplifies to only derivatives of the phase. Because of this, it is possible to use measurements of the derivative of the intensity to recover the phase [84]. This is a deterministic method, in contrast to the iterative methods discussed in chapter 2. However, this technique is limited by the requirement of the intensity of the sample to be uniform and by the paraxial approximation.

1.3 Ultrafast Measurements

With x-ray microscopy, it becomes possible to measure samples at the nano-scale. The dynamics of systems at this length scale are on the order of femtoseconds to picoseconds. Because of this, different techniques are needed to access the ultrafast dynamics.

Attempts to measure phenomena faster than the human eye can detect have a long history [119]. The idea of using a bright flash of light to isolate a moment in time began with Toepler [120, 237], who used a spark to create shock waves, which he then measured with a second, delayed spark. This was improved upon by Abraham and Lemoine, who used a single spark for driving and measuring the Kerr effect [3]. The notion behind these experiments is that light can be used to isolate a moment in time. Furthermore, by driving dynamics synchronously with the light used for measurement, and varying the time delay between the two, multiple different instances in time of the same dynamics can be measured. This is the concept behind pump-probe measurements, wherein a pulse initiates dynamics and then a delayed pulse measures those dynamics. A generalized schematic of this idea is shown in figure 1.4. This pump-probe technique has been extended to much shorter time scales [119, 256]. These improvements to the temporal resolution are limited by the duration

of the pulses and the synchronization between the two pulses [14, 71].

Since the first demonstration of the laser [144], there has been continuous development of shorter laser pulses. In the years just after the initial demonstration, the q-switching technique was demonstrated, enabling pulses of nanosecond duration [154]. The development of mode-locked lasers [46, 50, 89, 253] reduced that lower limit to the femtosecond scale (A review of these developments can be found in [90]). For dye lasers, this culminated in a record of 6 fs duration by use of spectral phase corrections [71]. Shortly after this landmark, the development of mode-locking in Ti:Sapphire laser systems [221] progressed rapidly, soon achieving 5 fs duration [14]. These Ti:Sapphire systems have enabled yet shorter pulses through high harmonic generation (chapter 5), reaching the attosecond time scale.

One alternative to pump-probe measurements is the use of a streak camera [24, 204]. The principle behind such a camera is that some optic before the sensor is actuated so that the light pulse is incident on a different part of the sensor at each moment in time. This results in the pulse being streaked across the sensor, isolating different times. This technique is typically limited to the picosecond timescale, however.

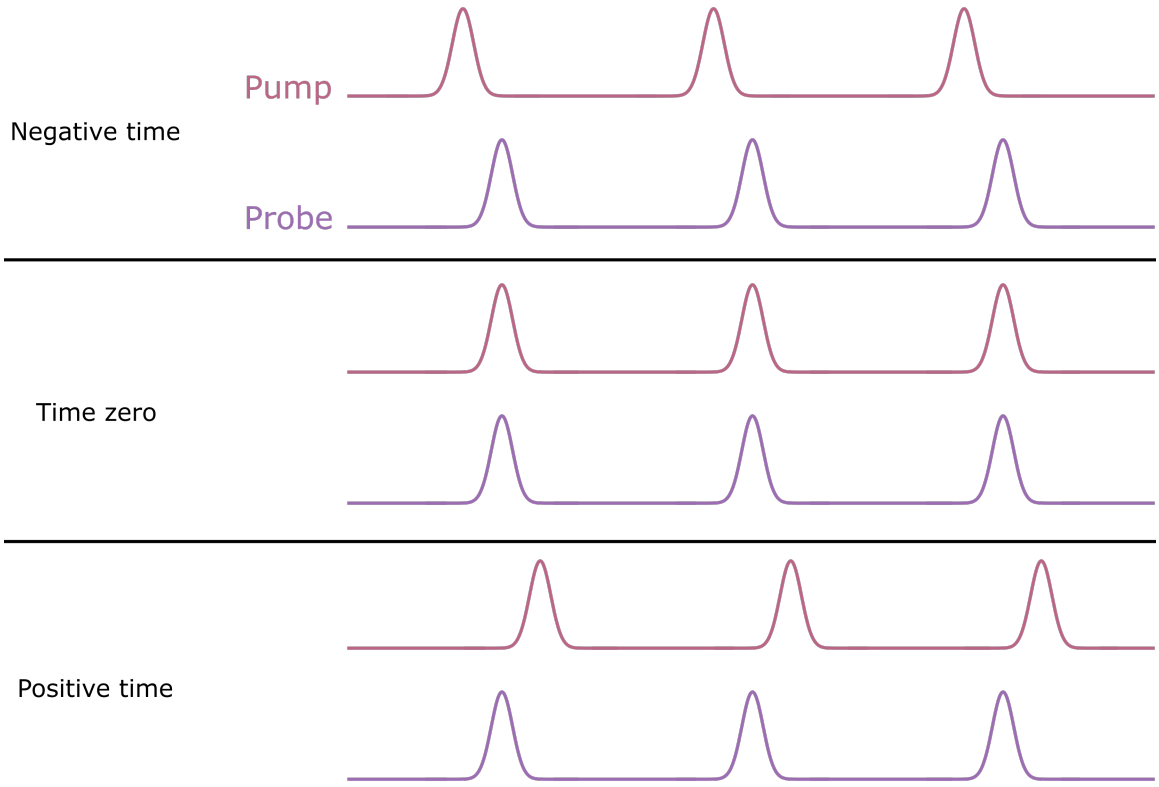

Figure 1.4: Sketch of Pump-Probe Measurement. The pump and probe pulses are both incident on the sample, but the timing between them may be changed. When the probe is incident on the sample before the pump, no dynamics are observed as they have yet to be excited; this is negative time (top). The two pulses are coincident on the sample at time zero (middle). Dynamics are observed when the probe pulse is delayed relative to the pump pulse; this is positive time (bottom).

Chapter 2

Coherent Diffractive Imaging

2.1 Introduction

Coherent diffractive imaging (CDI) is a broad assortment of techniques that deal with reconstructing a real space image from one or more measurements of scattered light. These techniques are especially useful in the fields of x-ray and extreme ultraviolet imaging, in which traditional lenses are not available to form an image directly. In this chapter, we review the development of CDI techniques and discuss the algorithms used.

Due to the high frequency of light, the phase of the light cannot be directly measured. The idea that one can retrieve the phase from a single intensity measurement was initially proposed by Sayre [203], commenting on Shannon's sampling theorem [210]. The possibility of retrieving the phase in the one-dimensional case was considered, however it was found that the ambiguities inherent in one-dimensional phase retrieval grow as 2^N where N is the size of the object in question [18, 25, 241]. A practical algorithm for two-dimensional phase retrieval was first put forward by Gerchberg and Saxton [77]. Fienup developed various algorithms to make these algorithms more broadly applicable [67–69]. These algorithms were implemented on experimental data, demonstrating coherent diffractive imaging in 1988 [27].

All of the above CDI algorithms work by taking intensity measurements and recovering the missing phase information. Once the phase and intensity are both known, the light field can be propagated back to the plane of the sample, thus forming an image. In order for the phase to be retrieved, the measurement of the diffracted light must be sampled at the

Nyquist frequency. This requirement on the fine spacing of the measurements in diffraction space puts a limit on the maximum separation in the object space. For a given pixelated detector with a pixel separation of δX, the highest frequency that can be Nyquist sampled is given by

$$f_{max} = \frac{1}{2\delta X} \tag{2.1}$$

The spatial frequency resulting from a pair of delta functions separated by a distance D is given by

$$f = \frac{D}{\lambda z} \tag{2.2}$$

where λ is the wavelength of the light and z is the propagation distance between the sample and the detector. The highest frequency allowed by Nyquist sampling sets the limit on the largest separation in the object

$$\frac{1}{2\delta X} \geq \frac{D}{\lambda z} \tag{2.3}$$

This can be rearranged so that we can define the oversampling of the diffraction pattern σ

$$\sigma = \frac{\lambda z}{\delta X D} \geq 2 \tag{2.4}$$

The requirement that the oversampling be greater than 2 is a necessary condition for phase retrieval [158, 159, 161, 165, 220].

2.2 Reconstruction Algorithms

The earliest phase retrieval algorithm is that of Gerchberg and Saxton [77]. This algorithm uses multiple measurements of the intensity at different planes in order to reconstruct the phase. This work was built upon by Fienup [68] who removed the additional intensity measurements.

The algorithm presented by Fienup called Input-Output [68] illustrates the general flow of most iterative phase retrieval algorithms. An initial guess of the reconstructed object is used as an initialization. This guess is propagated to the plane of the detector. The amplitude

of the propagated guess is replaced with the measured amplitude, refining the guess. Then this refined guess is propagated back to the plane of the object. At this point, the guess for the object is forced to adhere to some condition. In the case of the Gerchberg-Saxton algorithm, the condition is another measurement of the amplitude [77]. However, in the case of Input-Output and other techniques where only one diffraction pattern is measured, this is not possible. Instead, the object is constrained to exist only within a finite region, called a support. The size of this support is determined by the oversampling requirements discussed in the previous section. Once the object guess has been updated according to this constraint, the entire process is repeated, until eventually the algorithm converges on the correct, retrieved phase. This iterative procedure is shown diagrammatically in figure 2.1.

Since the initial development of these coherent diffractive imaging techniques, various improvements have been made to the reconstruction algorithms used. Iterative refinement of the support used in the object constraint improved reconstruction speed [150]. Other techniques modified the algorithms so that the sample did not need to be physically isolated, either by tightly focusing the illumination [1, 247, 248], or by applying an aperture the illuminating light [75, 87]. Development in the nature of the algorithms themselves also brought improvements to reconstruction speed and reliability [4, 137, 151]. These techniques have also been considered in the case of background noise [236] and partial coherence [244, 249].

The techniques of coherent diffractive imaging have found a welcome home in the field of x-ray imaging where it is challenging to manufacture image forming optics. In 1999, the first demonstrations of coherent diffractive imaging with x-ray sources were performed [160, 189]. Since then, the applications of coherent diffractive imaging techniques to x-ray imaging have been numerous and varied [33, 164]. Applications include studies on nano-crystalline structure [179, 190, 246], integrated circuits [2], and biological samples [163, 211]. Concurrently, Zuo et al. developed coherent diffractive imaging using electron sources [262].

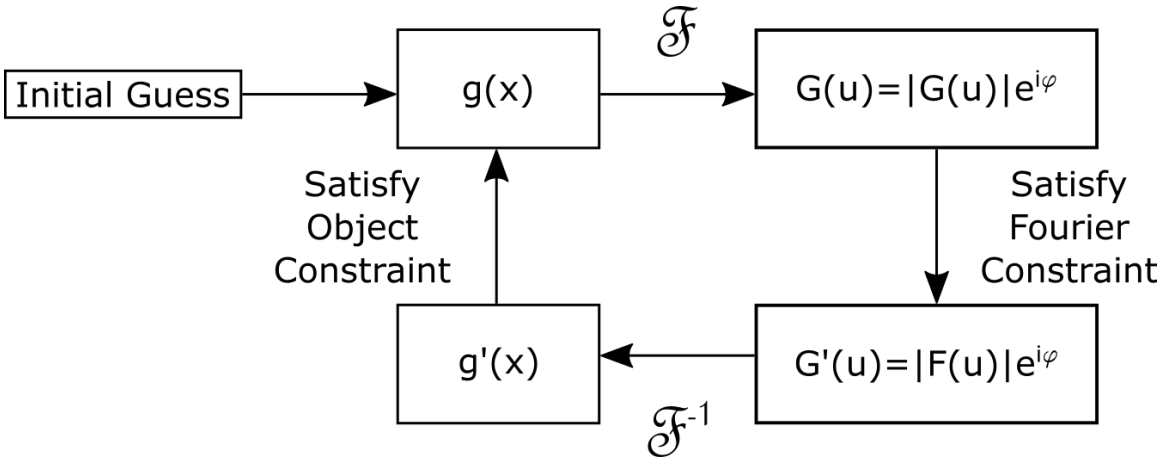

Figure 2.1: Input-Output Algorithm. The phase of the optical field is recovered by iterating between the detector plane and the sample plane by means of the Fourier transform. In each of these planes, a constraint is enforced. In the detector plane, the Fourier constraint is applied, forcing the reconstruction to match the measured data. In the object plane an isolation or non-negativity constraint is applied. This single iteration of the algorithm is repeated until the algorithm converges on a single solution.

2.3 Ptychography

The previously discussed algorithms use a single diffraction pattern measurement to reconstruct the phase. These techniques require minimal data, yet they are not particularly robust. Additional robustness can be achieved in CDI by measuring multiple diffraction patterns to reconstruct a single image. This multiplicity of measurements is used in a technique called ptychography, which is a more robust CDI technique. In ptychography, multiple diffraction patterns are measured as the beam is scanned across the sample. Each position of the beam overlaps somewhat with the other positions. This overlap introduces a redundancy in the measurement, which increases the robustness of the entire technique. The curious reader can find a more robust review of the development of ptychography in [191, 192].

The concept of ptychography began with the work of Hoppe, who considered the problem of phase retrieval for electron interference [99, 101, 102]. This is the origin of the idea of recording multiple diffraction patterns with a translational shift between them in order to overcome ambiguities in phase retrieval. This technique became known as ptychography [91, 92, 100] from the Greek word 'ptycho' ($\pi\tau\nu\xi$) meaning to fold. This is because the German word for 'convolution' ('Faulung') is the same word as 'to fold' [192].

Early alterations to the classical ptychography scheme involved the use of Wigner distribution deconvolutions [19, 193], which was experimentally realized in optical, electron, and x-ray microscopes [31, 72, 153].

Ptychographic phase retrieval began to gain popularity after the development of iterative phase retrieval algorithms [64, 83, 194]. These preliminary algorithms required that the functional form of the illumination be known *a priori*. This limitation was lifted when improved algorithms were developed that not only reconstructed the sample, but also deconvolved it from the probe, allowing for simultaneous probe retrieval [143, 233, 234].

Since then, many improvements have been made to the ptychography technique. Con-

stant improvements to the underlying algorithm have yielded improved robustness and faster reconstructions [133, 141, 232]. Algorithms have been designed to correct for errors in the recorded scan positions, allowing for more flexible experimental designs [140, 259]. Alternative scanning patterns have been designed, most notably the Fermat spiral pattern [104], to counter the gridding artifacts present in the technique [233] and to better image periodic objects [74]. Even the oversampling requirement of phase retrieval has been relaxed using a ptychographic measurement [20, 58]. In a similar vein, the resolution achieved through ptychographic imaging, previously limited by the numerical aperture of the detector, can be computationally extended, allowing for super-resolution imaging [142]. Furthermore, the effects of a beamblock have been investigated, showing that ptychography algorithms can recover the lost, low frequency information [135].

Ptychographic reconstructions have also been used to study three-dimensional samples in both a multi-slice modality [80, 139, 213, 227] and by combining ptychography with tomography [49, 51, 62, 73, 96]. Recently these two approaches have been merged [132]. In addition, surface studies have been performed by applying single diffraction pattern coherent diffractive imaging techniques [197, 226, 263], and later ptychography [75, 148, 182] to a reflection geometry, which has found great application in extreme ultraviolet surface imaging [88, 126, 208, 257].

Even the inherent drawback of ptychography, the slowness resulting from scanning, has been improved upon. The need for individual, isolated scan positions has been relaxed, allowing for continuous motion scanning to collect the ptychography dataset [41, 47, 103, 172, 177]. Yet the need for scanning at all has also been reduced. By carefully grooming the illumination profile, multiple scan positions can be collected simultaneously by dividing the detector into smaller sections, enabling single-shot ptychography [174, 214].

2.4 Derivation of Ptychography Update

In the case of single diffraction pattern coherent diffractive imaging, the iterative algorithms used transferred between the object domain and the detector domain (also called the Fourier domain), applying a constraint on each of these domains. Ptychography coherent diffractive imaging also does this. The Fourier domain constraint is the same: the amplitude must match the measured intensity. The object domain constraint is less obvious. One approach to updating the object space representation is to define an error metric, and act to minimize that error. In this instance, each diffraction pattern from the ptychography dataset is treated sequentially, and thus this derivation will focus on only one scan location, but is applicable to each location. It is possible to create an implementation of ptychography that updates all positions in parallel.

The error metric is defined as

$$\mathcal{E}(u) = \Sigma_u \left(|G(u)| - |F(u)| \right)^2 \tag{2.5}$$

where $G(u)$ is the current guess of the field at the detector and $F(u)$ is the measured amplitude at the detector. In the case of ptychography, the field at the detector can be written as

$$G(u) = |G(u)| \, e^{i\phi} = \int O(x) P(x - x_0) e^{2\pi i u x} dx \tag{2.6}$$

where O is the object, P is the probe, x is the spatial dimension of the object, x_0 is the current probe position, and u is the frequency dimension of the Fourier domain. Note that this derivation is being performed in one dimension, yet it can be readily extended to the requisite two dimensions for ptychography. Minimizing this error with respect to the object requires the calculation of the first derivative of the error with respect to the real part of the object. This process can be repeated for the imaginary part of the object, which has been omitted from this derivation.

$$\frac{\partial \mathcal{E}}{\partial \mathcal{R}O(x)} = 2\Sigma_u \left(|G(u)| - |F(u)| \right) \frac{\partial |G(u)|}{\partial \mathcal{R}O(x)} \tag{2.7}$$

This final derivative can be expressed as

$$\begin{aligned}\frac{\partial|G(u)|}{\partial\mathcal{R}O(x)} &= \frac{\partial}{\partial O(x)}\sqrt{G(u)G^*(u)} \\ &= \frac{1}{2|G(u)|}\left(G(u)\int P^*(x-x_0)e^{-2\pi iux}dx + G^*(u)\int P(x-x_0)e^{2\pi iux}dx\right)\end{aligned} \tag{2.8}$$

At this point, it is helpful to define the field after the constraint has been applied in the detector plane, $G'(u)$

$$G'(u) = G(u)\frac{|F(u)|}{|G(u)|} \tag{2.9}$$

Inserting this definition into the expression for the derivative of the error metric yields

$$\begin{aligned}\frac{\partial\mathcal{E}}{\partial\mathcal{R}O(x)} &= \int P^*(x-x_0)\Sigma_u G(u)e^{-2\pi iux}dx + \int P(x-x_0)\Sigma_u G^*(u)e^{2\pi iux}dx \\ &\quad - \int P^*(x-x_0)\Sigma_u G'(u)e^{-2\pi iux}dx - \int P(x-x_0)\Sigma_u G'^*(u)e^{2\pi iux}dx\end{aligned} \tag{2.10}$$

Each of these terms is a discrete, inverse Fourier transform, which will bring all of the field expressions to the object domain, where they are denoted by lowercase letters g and g'.

$$\begin{aligned}\frac{\partial\mathcal{E}}{\partial\mathcal{R}O(x)} &= \int P^*(x-x_0)g(x)dx + \int P(x-x_0)g^*(x)dx \\ &\quad - \int P^*(x-x_0)g'(x)dx - \int P(x-x_0)g'^*(x)dx\end{aligned} \tag{2.11}$$

This derivative is then set equal to zero and the definition for $g(x) = O(x)P(x-x_0)$ and $g'(x) = O'(x)P'(x-x_0)$ are invoked. Further, the integrand in the above equation is taken to be equal to zero, as opposed to the full integral.

$$2\mathcal{R}\left(P^*(x-x_0)O(x)P(x-x_0)\right) = 2\mathcal{R}\left(P^*(x-x_0)O'(x)P'(x-x_0)\right) \tag{2.12}$$

This equation can be rewritten into the form

$$\mathcal{R}(O(x)) = \frac{\mathcal{R}\left(P^*(x-x_0)O'(x)P'(x-x_0)\right)}{|P(x-x_0)|^2} \tag{2.13}$$

A similar derivation using the derivative with respect to the imaginary part of the object yields a similar result, quoted here without derivation

$$i\mathcal{I}(O(x)) = \frac{i\mathcal{I}\left(P^*(x-x_0)O'(x)P'(x-x_0)\right)}{|P(x-x_0)|^2} \tag{2.14}$$

Combining these two results yields a single expression for the update of the complex object.

$$O(x) = \frac{P^*(x - x_0)P'(x - x_0)O'(x)}{|P(x - x_0)|^2} \tag{2.15}$$

Using the definition of the full field $g(x) = P(x - x_0)O(x)$, this expression can be written in a more usable format.

$$O(x) = O(x) + \frac{P^*(x - x_0)}{|P(x - x_0)|^2} (g'(x) - g(x)) \tag{2.16}$$

Due to the inherent symmetry between the object and the probe, a similar update can be used on the probe

$$P(x) = P(x) + \frac{O^*(x + x_0)}{|O(x + x_0)|^2} (g'(x) - g(x)) \tag{2.17}$$

These two update expressions can be used iteratively along with the Fourier update condition to form the entirety of a basic ptychography algorithm. Typically the denominators of these update expressions are modified in order to remove the possibility of dividing by zero. The standard way to do this is by using the maximum value of the object or probe in the denominator as in [143].

Chapter 3

Multiple Mode Ptychography

3.1 Introduction

The technique of ptychography discussed in chapter 2 can be extended to account for multiple different incoherent modes [20, 235]. In this chapter, we review the technique of multiple mode ptychography, and then extend this technique by introducing spatial separation between the different modes, as published in [110].

In the case of multiple wavelengths [20], the measured diffraction pattern is treated as an incoherent sum of the scatter from each independent wavelength. These different wavelengths can be separated through a slightly modified ptychography algorithm. This algorithm makes use of the fact that when incident on the same object, different wavelengths scatter to different angles. The error metric that is optimized in multiple wavelength ptychography is

$$E = \Sigma_u \left[\Sigma_m \left|G_m(u)\right| - \left|F(u)\right|\right]^2 \tag{3.1}$$

where each $G_m(u)$ is the reconstructed field for each wavelength, and $F(u)$ is the measured amplitude at the detector. Through a similar derivation as that in chapter 2, the new update conditions in the object domain are given by

$$O_m(x) = O_m(x) + \frac{P_m^*(x - x_0)}{|P_m(x - x_0)|^2} \left(g'_m(x) - g_m(x)\right) \tag{3.2}$$

$$P_m(x) = P_m(x) + \frac{O_m^*(x + x_0)}{|O_m(x + x_0)|^2} \left(g'_m(x) - g_m(x)\right) \tag{3.3}$$

There is also a slight modification to the Fourier domain constraint, as there must be since the incoherent sum of all independent modes is measured, not the individual intensities. This update condition is now

$$G'_m(u) = \frac{|F(u)|}{\sqrt{\Sigma_m |G_m(u)|^2}} G_m(u) \tag{3.4}$$

Both of these sets of update equations are used sequentially to form a single iteration of a multiple mode ptychography algorithm. This algorithm, or others like it, can be used to separate the different modes present in an arbitrary illumination profile. The idea of multi-modal ptychography has been used in the case of extreme ultraviolet light [258], broad-bandwidth radiation [13, 60], vortex beams [61], with more applications besides [212]. In this chapter, multiple mode ptychography is applied for use in a multiple beam geometry.

3.2 Spatial Separation

The original treatment of the multiple color ptychography used a beam of different colors that were all incident on the sample in the same location [20]. Based on the formulation of the algorithm, this requirement is not necessary. In fact, not only do the probes of different wavelengths not need to be overlapped, they can be completely separated spatially [109, 110].

3.2.1 Wavelength Multiplexing

In order to test this spatial multiplexed ptychography, we constructed a visible light ptychography microscope. A schematic view of this microscope is shown in figure 3.1. A beamsplitting cube is used to combine two narrow bandwidth lasers of different wavelengths. These are then separated, while remaining parallel through use of a pair of diffraction gratings. A pinhole is used to block all of the other orders diffracted from these gratings. A lens is used to image the beams onto the sample and thus set the size of the beam to obey the oversampling requirement. The sample measured in this experiment is a USAF1951 Air

Force test pattern. One lens is placed after the sample to take the Fourier transform of the exit surface wave of the sample. This final lens is not strictly necessary, yet its inclusion allows for a more compact design.

Diffraction patterns were recorded at multiple exposure times and then combined to artificially increase the dynamic range of the detector. The multi-wavelength ptychography algorithm from [20] was used to reconstruct the field of view of the red beam and the blue beam simultaneously. The two areas imaged (shown in figure 3.2) are separated by a distance of 175±5 μm. This corresponds to the spatial separation of the beams imaged directly onto the camera. Furthermore, by propagating the recovered probes, the distance from the sample plane to the focal planes of the two different beams can be determined. The propagated beams are shown in figure 3.3. The distance between the two focal planes was found to be 550±100 μm, which is in agreement with the distance expected from the chromatic aberration of the lens (420±4 μm).

3.2.2 Polarization Multiplexing

The previous section dealt with using multiple, spatially separated probes of different wavelengths. The different wavelengths were needed so that the two probes did not interfere at the detector. This is not the only way to achieve a lack of interference; any non-interfering modes will work [235]. In this section, the spatial multiplexing of multiple probes in ptychography is achieved using orthogonally polarized beams [110].

A single laser beam was spatially separated into two parallel beams of orthogonal polarizations through use of a beta barium borate (BBO) crystal. These two beams are incident on the same USAF resolution target as shown in figure 3.4. The separation of these beams is measured to be 233 μm, verified by direct imaging of the beams in figure 3.5. The diffraction from these two beams is recorded on a pixelated detector and reconstructed using the multiple mode ptychography algorithm.

The reconstructed images are displayed in figure 3.6. The parallel polarization was

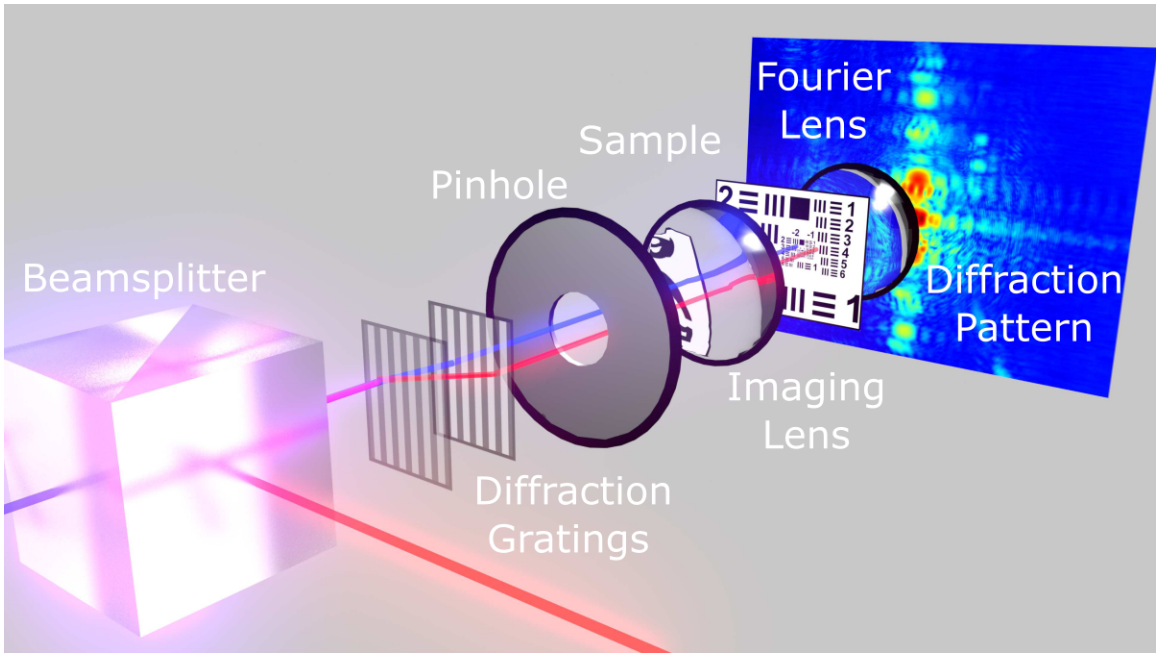

Figure 3.1: Spatially Separated Multi-Wavelength Ptychography Schematic. This schematic shows the experimental design for a visible light ptychography microscope that uses two illuminating beams of different colors. The two beams are combined with a beamsplitter and then spatially separated, while remaining parallel, by use of a pair of diffraction gratings. The two beams are them imaged onto the sample, a US Air Force test pattern. The resulting diffraction is measured on a pixelated detector.

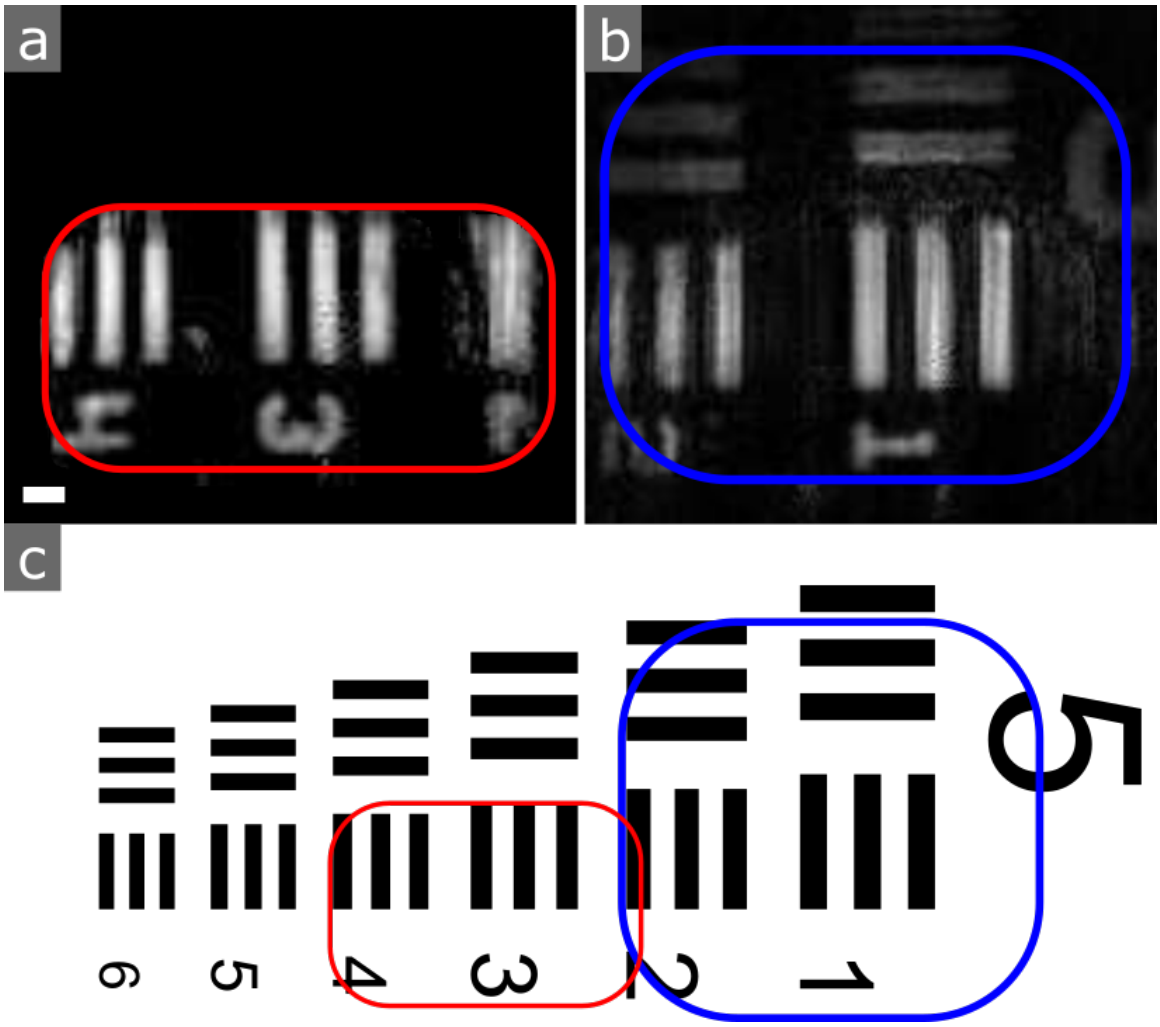

Figure 3.2: Spatially Separated Multi-Wavelength Reconstruction. Reconstructions for the red (a) and blue (b) beams. These areas correspond to the areas shown diagrammatically in (c). These reconstructions demonstrate that multiple mode ptychography algorithms can be used in a situation where the two modes are entirely spatially separated. The scale bar is 20 μm.

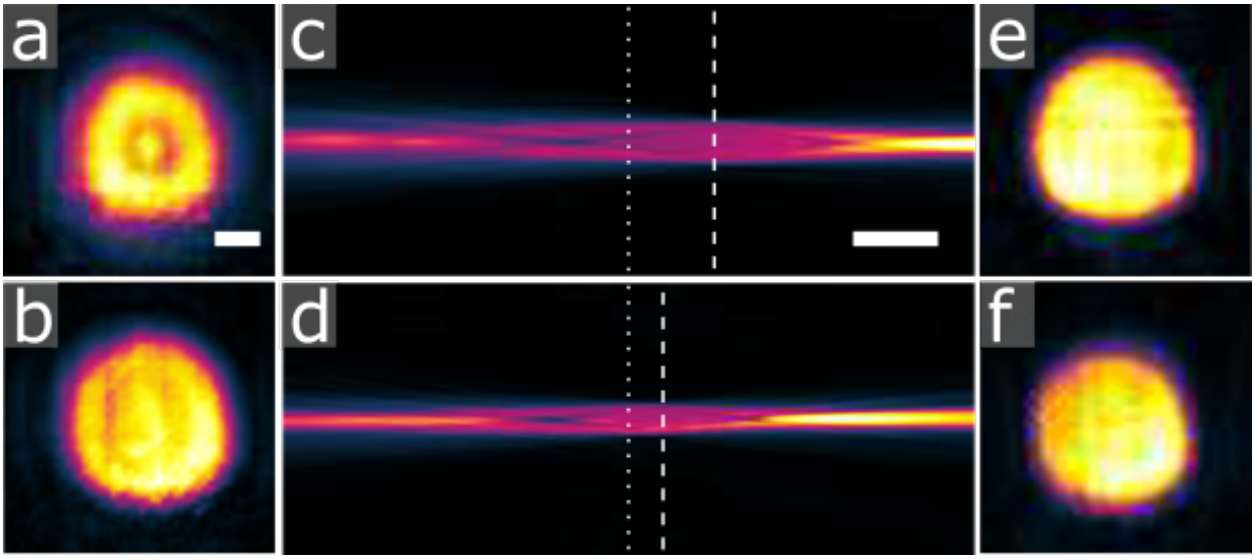

Figure 3.3: Propagation of Spatially Separated Probes. In order to verify the accuracy of the reconstructions, the reconstructed probes for each of the beams is propagated to the focal plane. The distance between the two focal planes is the same as the expected distance given the chromatic aberration in the lens. The scale bar in (c) is 1 mm and is shared with (d). The scale bar in (a) is 20 μm and is shared with (b), (e), and (f).

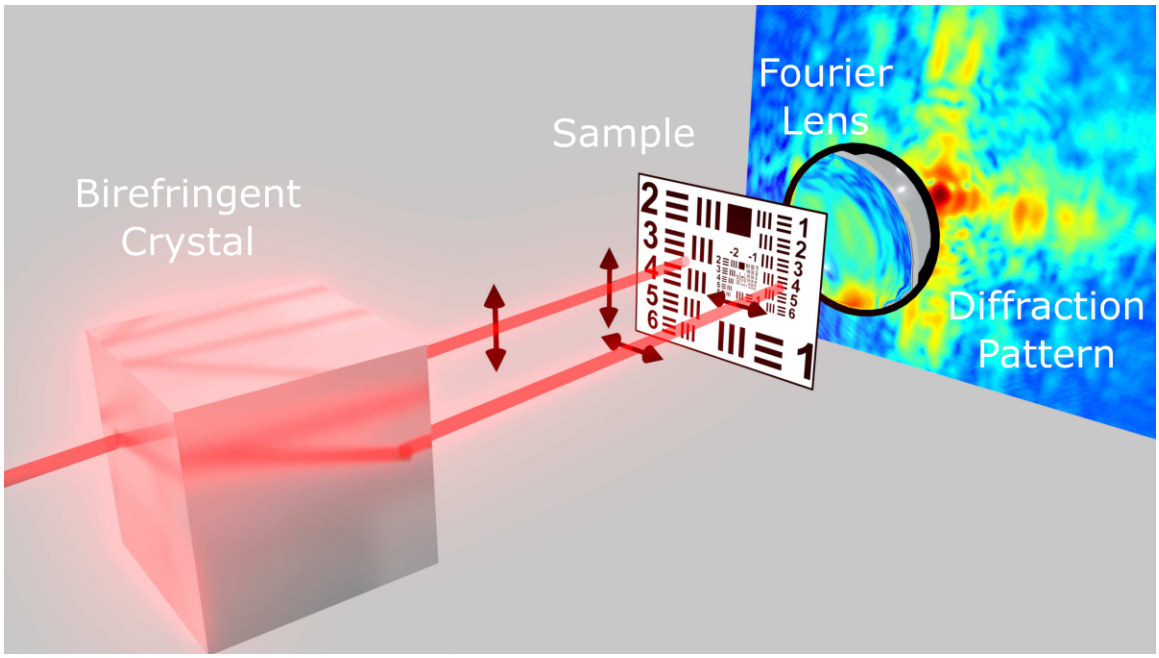

Figure 3.4: Spatially Separated Multi-Polarization Ptychography Schematic. In order to test multiple beam ptychography with different polarization states, a single beam is separated into two orthogonally polarized beams by use of a birefringent crystal. These two beams are incident on the sample and a Fourier transform lens is used to form a diffraction pattern on a pixelated detector.

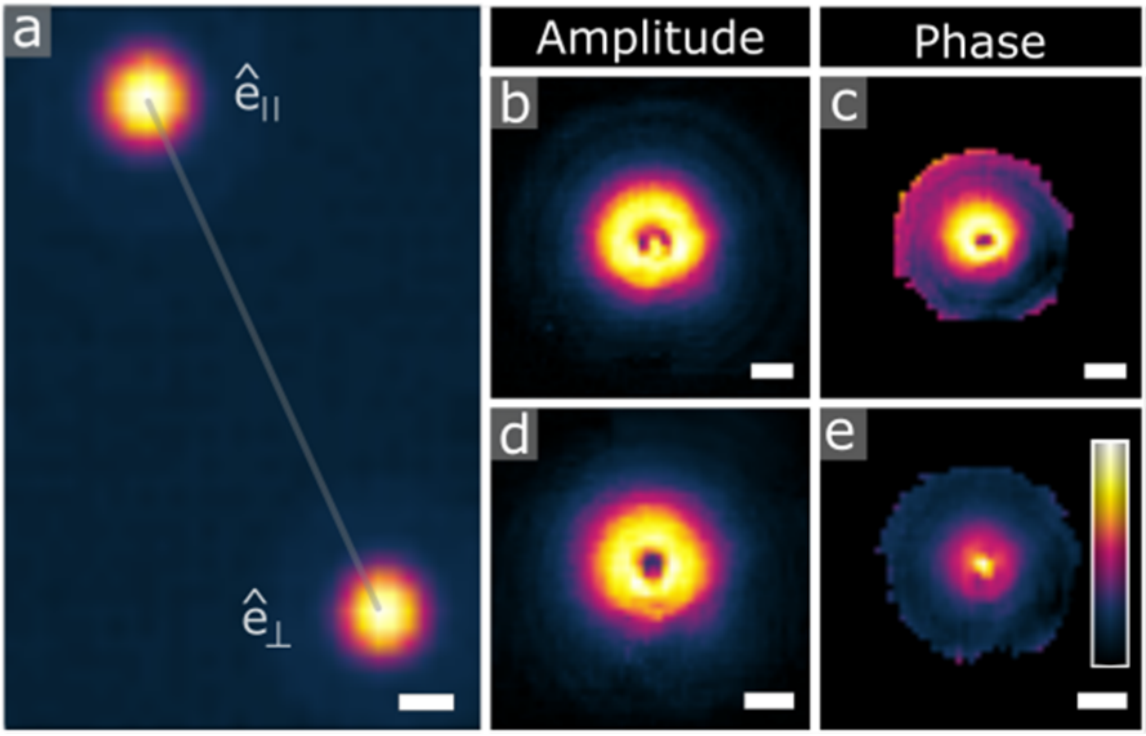

Figure 3.5: Reconstructed Multi-Polarization Probes. Direct image of the two beams showing the spatial separation between them. (b-c) Reconstruction of the probe in amplitude and phase, for the $\hat{e}_{||}$ polarized beam. (d-e) Reconstruction of the probe in amplitude and phase, for the $\hat{e}_{\perp}$ polarized beam. The scale bar is 20 μm.

incident on group 6 of the resolution target, while the perpendicular polarization was incident on group 7. In the group 7 image, subgroup 5 is resolved, indicating that the resolution of the microscope is at worst 2.46 μm, which is equivalent to the Abbe diffraction limit [242]. Since the resolution is at the theoretical limit, the multiple mode ptychography technique must not adversely affect the resolution.

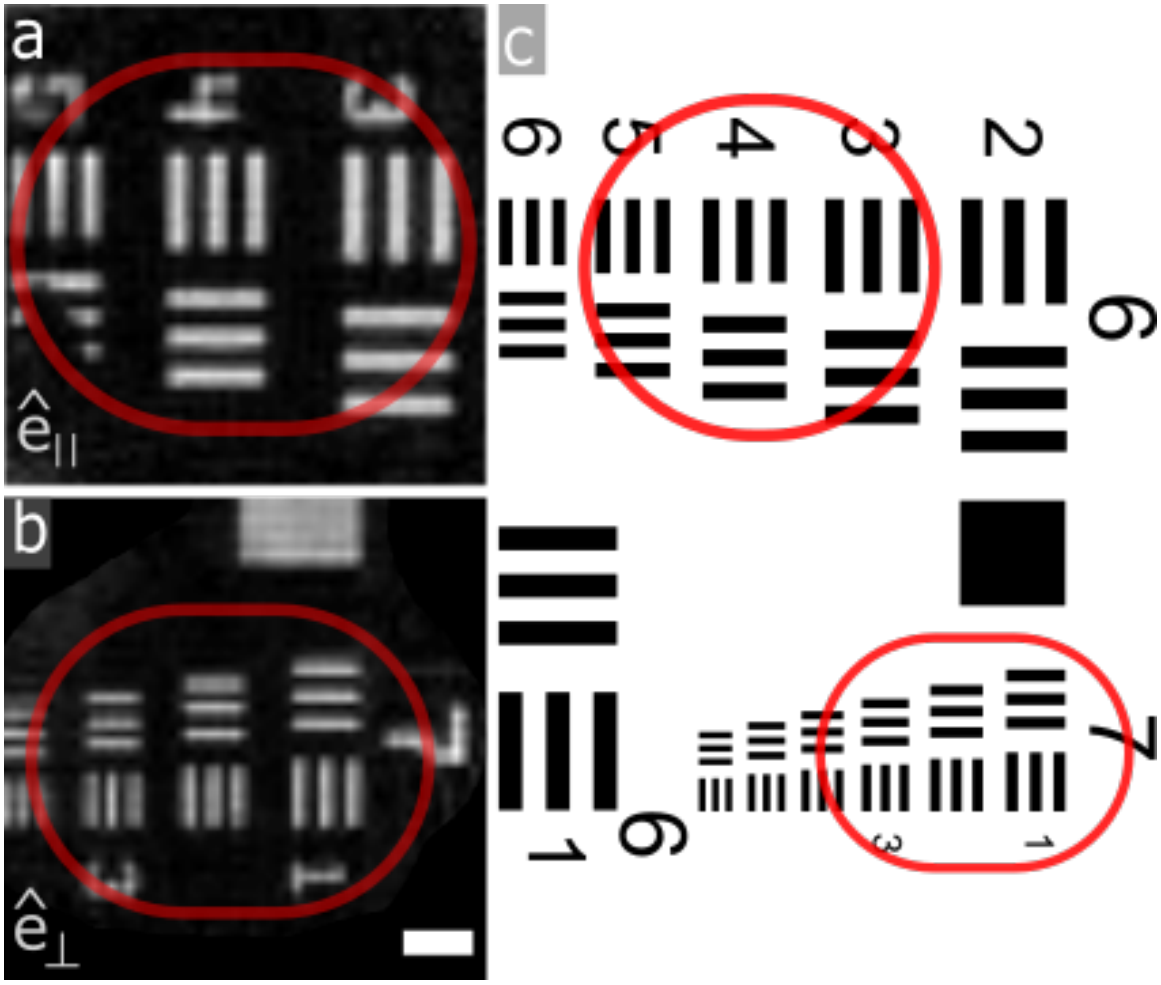

Figure 3.6: Spatially Separated Multi-Polarization Reconstruction. The left hand side shows the reconstructed objects for the parallel and perpendicular polarized beams. The right hand side shows, diagrammatically, the structure of the sample. The spatial separation between these two areas is in agreement with the measured separation of the beams. This indicates that multiple beams of orthogonal polarization states can be used in a multiple mode ptychography scan. The scale bar is 20 μm.

Chapter 4

Multiple Beam Ptychography

4.1 Introduction

The previous chapter discussed ptychography coherent diffractive imaging (CDI) with multiple modes and the application of this algorithm to the case of spatially separated beams that do not interfere [110]. In this chapter, multiple beams that do interfere with each other are considered and methods are developed to use the multiple mode ptychography algorithm [20, 235] in these situations. We published these techniques in [21, 109].

The experimental realizations of these concepts are also presented in this chapter. For each of these demonstrations, the setup in figure 4.1 is used with different pinhole sizes and separations in the pinhole array.

4.2 Autocorrelation Filtering

4.2.1 Theory

When two spatially separated beams that can interfere are incident on a sample, the exit surface wave can be written as

$$\psi(x) = E_1(x)O(x) + E_2(x + \Delta x)O(x) \tag{4.1}$$

where ψ is the exit surface wave, E_j is the jth probe function, O is the sample (or object), and Δx is the spatial separation of the beams. Note that this derivation uses a single dimension,

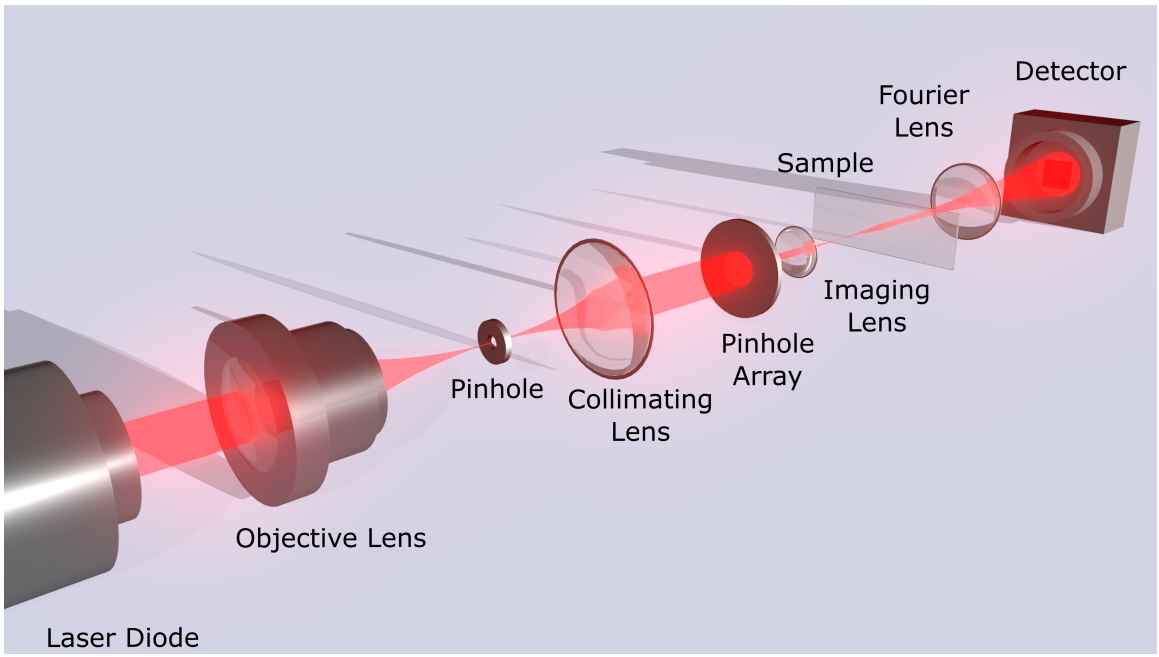

Figure 4.1: Schematic for Multiple Beam Ptychography. A visible laser is used for these experiments. The beam is spatially filtered with two lenses and a pinhole. Then the beam is incident on a pinhole array. This pinhole array varies depending on the specific technique being used. An imaging lens images the pinhole array onto the sample. A Fourier transform lens is used to propagate the light to the far-field, creating the diffraction pattern that is recorded on the detector.

but can be trivially extended to two dimensions. This exit surface wave is measured in the far-field. The intensity that is measured is given by

$$I(u) = |\Psi(u)|^2 = |\mathcal{F}\{E_1(x)O(x) + E_2(x+\Delta x)O(x)\}|^2 \tag{4.2}$$

where I is the measured intensity, u is the spatial frequency coordinate and Ψ is the Fourier transform (denoted $\mathcal{F}$) of ψ. These Fourier transforms can be expanded by use of the Fourier shift theorem and the convolution theorem to arrive at

$$I(u) = \left|\tilde{E}_1(u) \otimes \tilde{O}(u)\right|^2 + \left|\tilde{E}_2(u)e^{i2\pi u\Delta x} \otimes \tilde{O}(u)\right|^2 + 2\mathcal{R}\left[\tilde{E}_1(u) \otimes \tilde{O}(u) \times \tilde{E}_2(u)e^{i2\pi u\Delta x} \otimes \tilde{O}(u)\right] \tag{4.3}$$

where $\otimes$ is a convolution, $\mathcal{R}$ indicates the real component and the notation $\tilde{O}(u)$ is shorthand for $\mathcal{F}\{O(x)\}$. This intensity measurement can be compared with the same measurement of two beams that do not interfere. Doing so reveals that the only difference between the expressions is in the final term. Thus, if the final term of equation 4.3 is eliminated, the resulting intensity is the incoherent sum of the two propagated beams. Under a Fourier transform, this term is spatially separated from the other terms, and therefore removable.

Similar to the technique in [128], a Fourier transform is performed to isolate the final term of the expression for intensity. This yields the autocorrelation of the exit surface wave

$$\begin{aligned}\mathcal{A}(\xi) = \mathcal{F}\Bigg\{&\left|\tilde{E}_1(u) \otimes \tilde{O}(u)\right|^2 + \left|\tilde{E}_2(u)e^{i2\pi u\Delta x} \otimes \tilde{O}(u)\right|^2 \\ &+2\mathcal{R}\left[\tilde{E}_1(u) \otimes \tilde{O}(u) \times \tilde{E}_2(u)e^{i2\pi u\Delta x} \otimes \tilde{O}(u)\right]\Bigg\}\end{aligned} \tag{4.4}$$

where $\mathcal{A}$ is the autocorrelation, and ξ is the variable in autocorrelation space (ξ has units of space, just as x does). Using the convolution theorem and the Fourier shift theorem, it can be shown that

$$\begin{aligned}\mathcal{A}(\xi) = &\left(\bar{E}_1(\xi)\bar{O}(\xi)\right) \otimes \left(\bar{E}_1^*(\xi)\bar{O}^*(\xi)\right) + \left(\bar{E}_2(\xi+\Delta x)\bar{O}(\xi)\right) \otimes \left(\bar{E}_2^*(\xi-\Delta x)\bar{O}^*(\xi)\right) \\ &+ \left(\bar{E}_1(\xi)\bar{O}(\xi)\right) \otimes \left(\bar{E}_2^*(\xi-\Delta x)\bar{O}^*(\xi)\right) + \left(\bar{E}_1^*(\xi)\bar{O}^*(\xi)\right) \otimes \left(\bar{E}_2(\xi+\Delta x)\bar{O}(\xi)\right)\end{aligned} \tag{4.5}$$

where the notation $\bar{O}(\xi) = \mathcal{F}\left\{\tilde{O}(u)\right\}$. The first two terms will both be centered at $\xi = 0$ while the third and fourth term will be centered at $\xi = \pm\Delta x$. These are referred to as DC

terms and AC terms, respectively. Taking only the DC terms and performing an inverse Fourier transform on them, the filtered intensity is obtained

$$I_{af}(u) = \mathcal{F}^{-1}\left\{\left(\bar{E}_1(\xi)\bar{O}(\xi)\right) \otimes \left(\bar{E}_1^*(\xi)\bar{O}^*(\xi)\right) + \left(\bar{E}_2(\xi+\Delta x)\bar{O}(\xi)\right) \otimes \left(\bar{E}_2^*(\xi-\Delta x)\bar{O}^*(\xi)\right)\right\} \tag{4.6}$$

where I_{af} is the autocorrelation filtered intensity. This expression simplifies to

$$I_{af}(u) = \left|\tilde{E}_1(u) \otimes \tilde{O}(u)\right|^2 + \left|\tilde{E}_2(u)e^{i2\pi u\Delta x} \otimes \tilde{O}(u)\right|^2 \tag{4.7}$$

This expression is identical to the intensity measured for two non-interfering beams. Therefore, by removing the AC terms in autocorrelation space, the interference between the beams can be removed. Note that following this same procedure, the method of autocorrelation filtering can be readily extended to two dimensions and more than two beams.

This autocorrelation filtering is depicted diagrammatically in figure 4.2. Two beams illuminate the object. The resulting diffraction pattern is measured in intensity. This diffraction pattern contains high frequency fringes that result from the interference between the two beams. The Fourier transform of the diffraction pattern has three distinct peaks. Of these peaks, only the DC peak is kept, thus filtering the autocorrelation. An inverse Fourier transform is performed on the filtered autocorrelation, yielding the original diffraction pattern with the high frequency fringes removed. This diffraction pattern is identical to the diffraction pattern that would be measured if the multiple beams did not interfere.

The DC terms can be isolated provided that all of the interference terms are separated from the DC terms in the autocorrelation. The condition that the autocorrelation peaks do not overlap is a condition on the size of the beams and the separation. Specifically, this condition forces the separation to be larger than twice the beam size. The reason that twice the beam size is the relevant parameter is because the autocorrelation of the beam has double the diameter of the beam itself. Defining the beam diameter as D, we have the condition

$$\Delta x \geq 2D \tag{4.8}$$

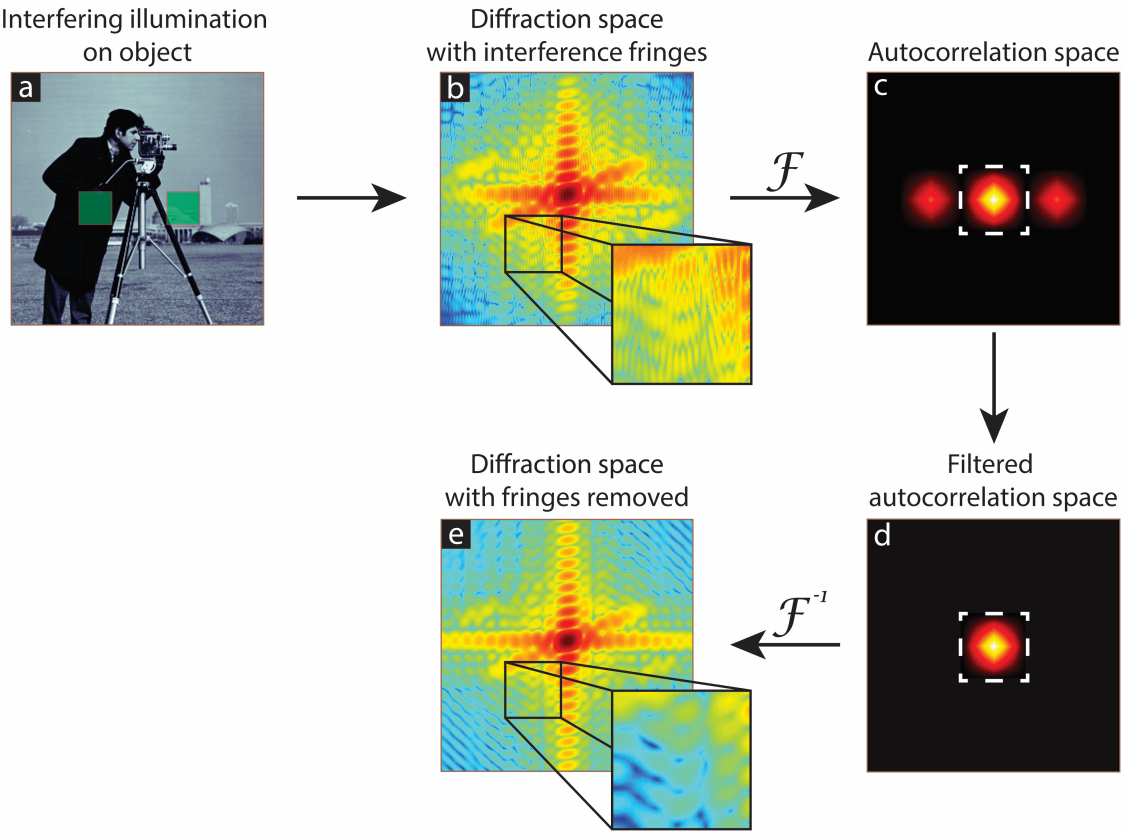

Figure 4.2: Autocorrelation Filtering Procedure. A single object is illuminated by two beams that are capable of interference. These beams are the green squares in (a). (b) That light propagates to the far-field and is measured as an intensity pattern that contains high frequency fringes from the two beam interference. (c) A Fourier transform is performed on the intensity pattern, yielding the autocorrelation of the exit surface wave. (d) The autocorrelation is low-pass filtered, leaving only the DC peak. (e) The filtered autocorrelation is inverse Fourier transformed, yielding a diffraction pattern with only the inter-beam interference removed. This diffraction pattern may then be fed into multiple mode ptychography algorithms.

where Δx is the beam separation. This constraint on the beam separation is not sufficient as it does not necessarily allow enough space for the AC terms. In order for the DC and AC terms to not overlap, the beams must be sufficiently small. The full extent of autocorrelation space is determined by the measurement geometry and is given by $\mathbb{X} = \frac{\lambda z}{p}$ where λ is the wavelength of light, z is the propagation distance between the sample and the detector, and p the pixel separation on the detector. The ratio between this maximum size and the actual size of the beam is known as the oversampling ratio, and is denoted as $\sigma = \mathbb{X}/D$. Typically, $\sigma = 2$ is required for CDI [18, 159]. The DC peaks and the AC peaks, all of which have a width of $2D$, must fit within the autocorrelation space window without overlap. The optimal way to do this requires that $\sigma = 4$, forcing the beam to be half of its otherwise maximum size.

One further consideration is that as the separation between the beams is increased, the resulting interference fringes will increase in spatial frequency. Eventually this frequency will become higher than the spatial frequency of the detector's pixels. When this occurs, the interference fringes will alias. Initially, this will cause the AC peaks to overlap with the DC peak, preventing autocorrelation filtering. However, if the separation is further increased, the interference frequency will alias back to an acceptable frequency, thus permitting autocorrelation filtering once again. The effects of aliasing on autocorrelation filtering (and on other techniques) are shown in figure 4.3.

The condition on the beam separation must include this aliasing effect. Therefore, it is best expressed as

$$2 \leq \mathrm{mod}\left(\frac{\Delta x}{D}, \sigma\right) \leq \sigma - 2 \tag{4.9}$$

where mod is the modulus operator.

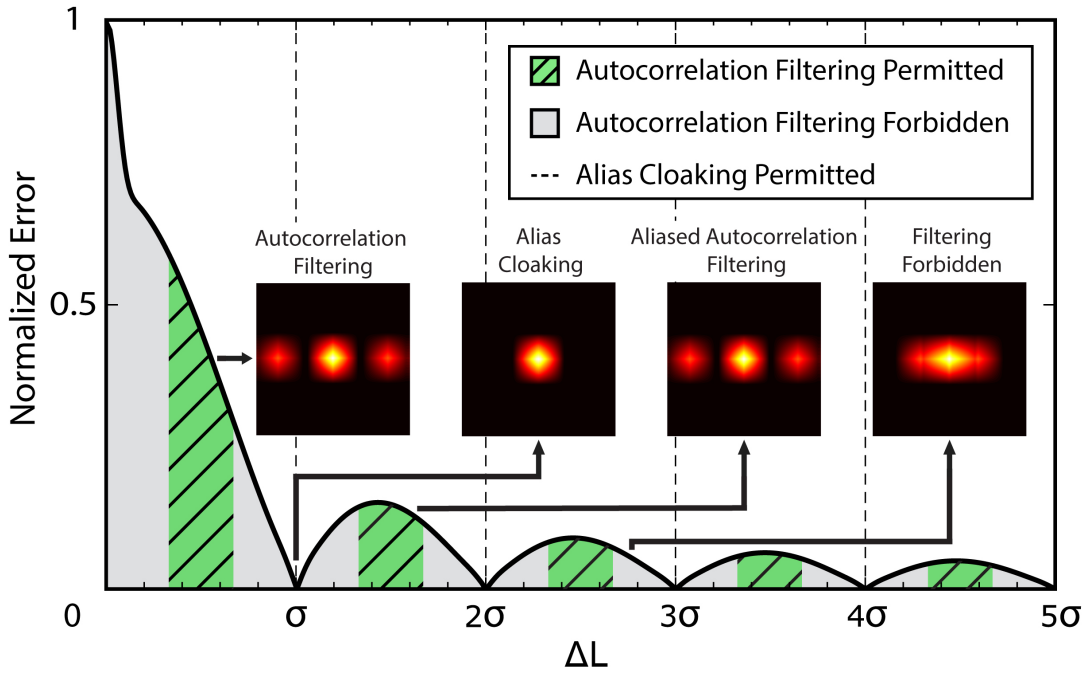

Figure 4.3: Effects of Aliasing on Autocorrelation Filtering. The difference between the intensity with interference and the intensity without interference is plotted as a function of beam separation. The areas in green correspond to beam separations for which autocorrelation filtering can occur. The areas in gray correspond to areas where autocorrelation filtering cannot occur because the AC and DC peaks overlap. There are multiple peaks to this function due to the aliasing of the interference terms. This allows for multiple regions where autocorrelation filtering can occur. There are also locations where the error drops to zero. In these locations, the interference frequency of the separated beams exactly matches the measurement frequency of the detector and thus is measured as a uniform background. In these locations, alias cloaking is permitted.

4.2.2 Experimental Demonstration

In this section, the feasibility of autocorrelation filtering is demonstrated experimentally. The setup shown in figure 4.1 is used with a three pinhole array. These three pinholes are in the form of a right triangle, with each pinhole at one vertex. This setup is displayed in figure 4.4. The pinhole mask was crafted from anodized aluminum foil [Thorlabs, BKF12] in which three holes were punched using a pushpin [Staples, 32014]. The diameter of the pinhole ranges from 90-175 μm. The separations of the holes are roughly 0.75 mm. These are imaged onto the sample with a magnification of 1. The Fourier transform lens has a 2 cm focal length. With these system parameters, the oversampling of each beam is between 10 and 15, with $\frac{\Delta x}{D}$ falling between 7.8 and 11.8. These parameters satisfy equation 4.9 without any aliasing on the detector.

121 diffraction patterns were recorded by moving the sample along an 11×11 rectilinear grid with 20% random offsets. The random offsets are introduced to avoid periodic artifacts in ptychography [51]. Each frame was a combination of exposures ranging from 0.05 ms to 750 ms, which were then combined together [188] to extend the dynamic range of the recorded diffraction pattern. The process of autocorrelation filtering for the experimental data is shown in figure 4.5. Because there are three beams in an 'L' formation, there should be six AC peaks. In reality, there are more than this, due to back-reflections of the diffracted light. These additional AC peaks do not influence the reconstructions because they are also filtered out of the data during this process.

The reconstructed objects and probes are shown in figure 4.6. The probes and objects are displayed in complex amplitude with amplitude mapped as brightness and phase as hue. The three reconstructed regions correspond to three different areas of the USAF test pattern.

A further test of the autocorrelation filtering method was performed. This test took advantage of the aliasing of the interference to use a larger beam separation. The setup for this experiment is shown in figure 4.7. A new pinhole was machined with 0.4 mm

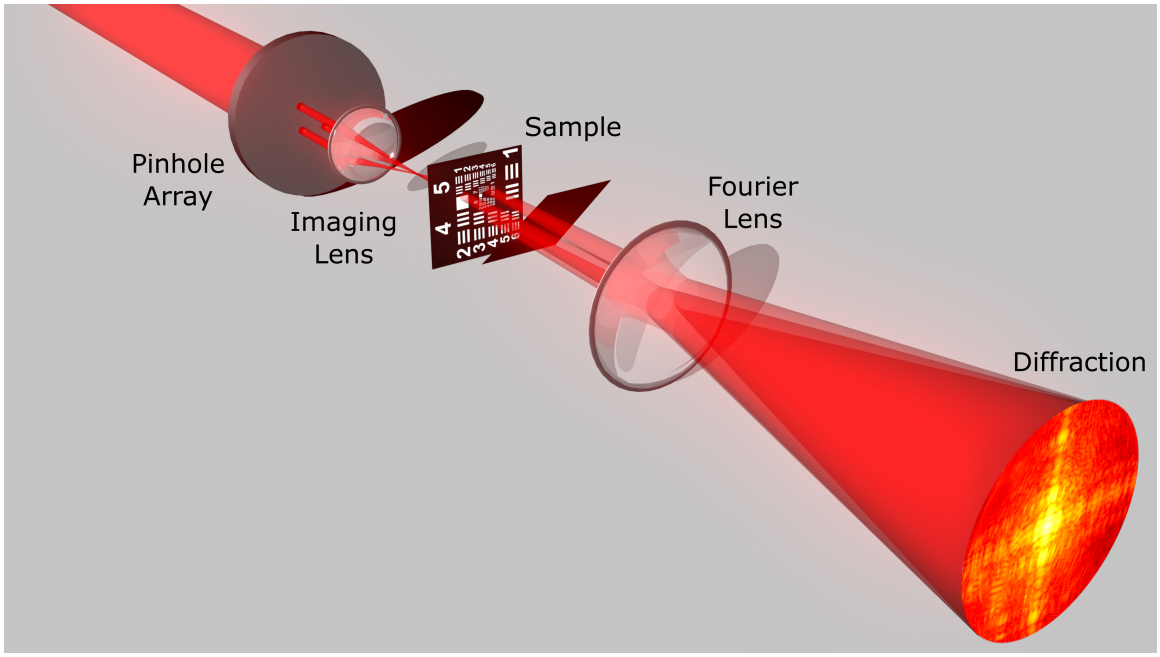

Figure 4.4: Experimental Setup for Autocorrelation Filtering. This figure shows the experimental geometry used to test the feasibility of the autocorrelation filtering technique. Three pinholes were punched in an 'L' shaped array that was imaged onto the sample. The sample is a US Air Force resolution test pattern. A ptychography data set was measured for this configuration and then processed to remove the interference between the three beams so that existing multiple mode ptychography algorithms could be used.

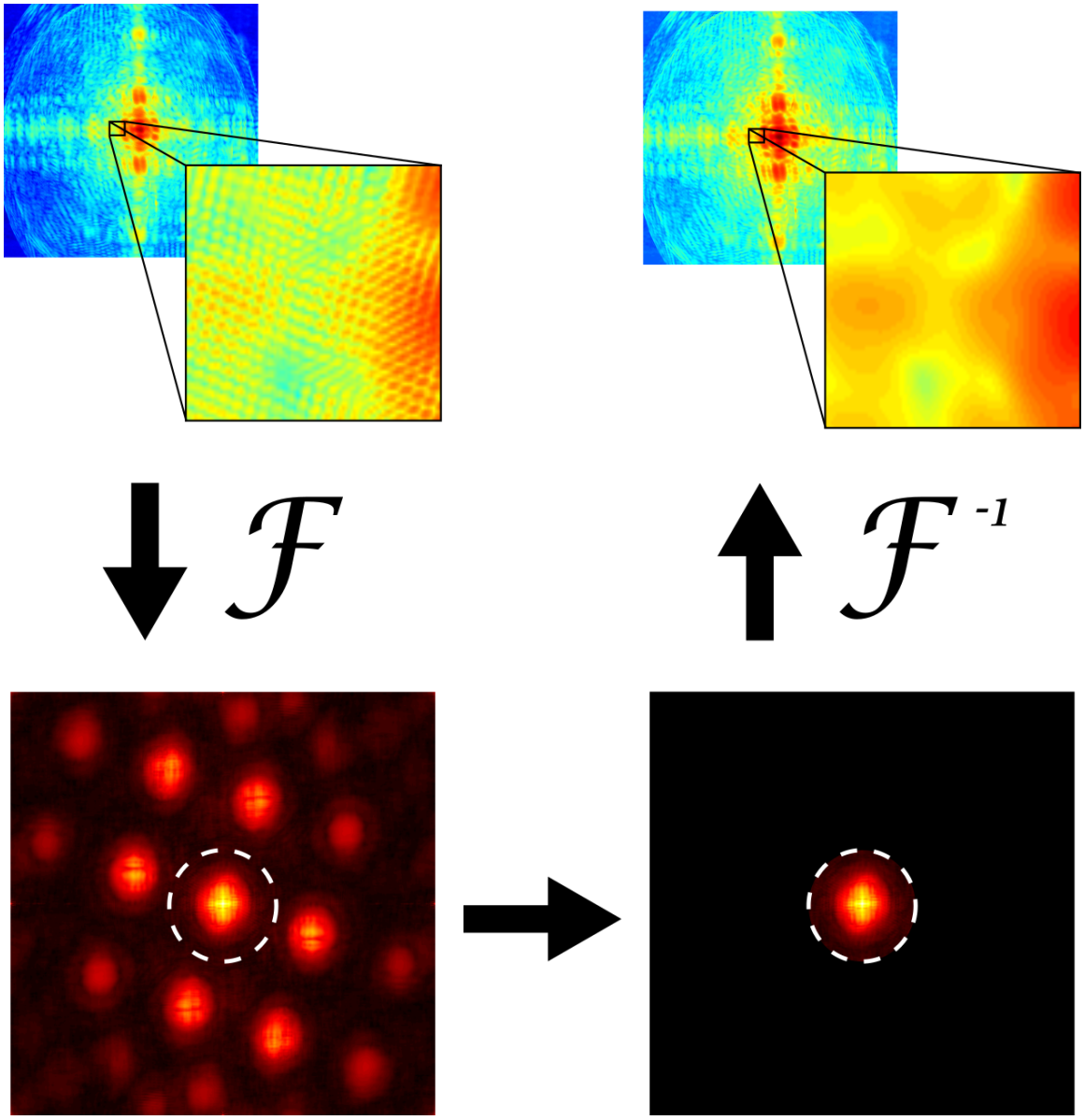

Figure 4.5: Autocorrelation Filtering of Experimental Data. The raw diffraction pattern data is shown in the top left. In the inset, the high frequency interference fringes can be observed. These are caused by the interference between the separate beams. A Fourier transform is performed, yielding the autocorrelation of the exit surface wave (bottom left). Only the central (DC) peak is kept (bottom right), the rest is filtered to suppress the inter-beam interference. An inverse Fourier transform is performed, which yields the original diffraction pattern with only the high frequency interference removed. This diffraction pattern can then be used for multiple mode ptychography.

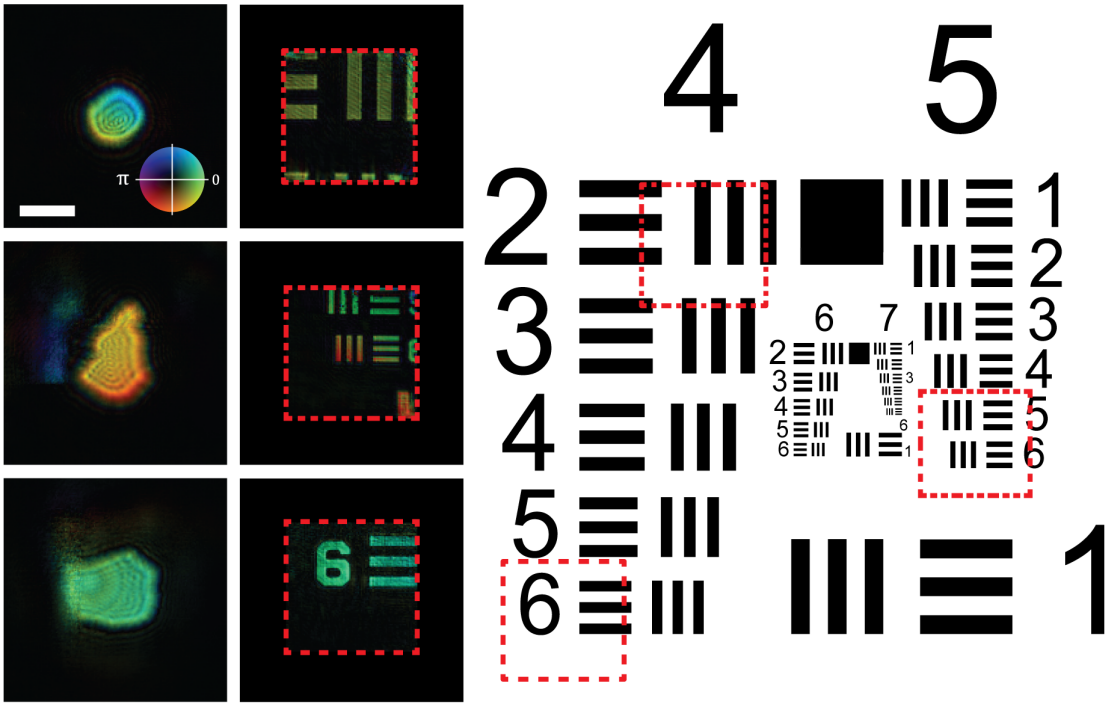

Figure 4.6: Reconstruction from Autocorrelation Filtered Ptychography. The reconstructed probes and corresponding objects are shown, displaying that the autocorrelation filtering technique allows for multiple field-of-view imaging. The three regions that were imaged correspond to the three regions indicated in the schematic on the right hand side. The scale bar is common to all of the reconstructions and is 200 μm wide. The brightness is amplitude; the hue is phase.

diameter holes separated by 3.7 mm. This gives a value of $\sigma = 6.3$. These parameters satisfy equation 4.9 placing this configuration in the second allowed region of figure 4.3. In this setup, the pinhole mask was not imaged onto the sample, but rather was placed close to the sample so that minimal diffraction could occur. The sample used was a slice through a stem of nymphaea of aqustio, preserved in cedar wood oil [AmScope PS25].

A 64 position ptychography scan was recorded with 20% random offsets. The data were processed as before to extend the dynamic range and to filter the autocorrelation. The reconstructed probes and sample are shown in figure 4.8.

4.3 Alias Cloaking

4.3.1 Theory

In figure 4.3, the effects of aliasing on the interference fringe frequency were discussed. In addition to the shifting of the frequency of the fringes, the aliasing also causes a decrease in the amplitude of the fringes. To capture this effect, figure 4.3 shows a normalized error for each beam separation. This error is the difference between the diffraction pattern that includes the interference between the two beams and the the diffraction pattern that does not include this interference. This can be written

$$\mathcal{E}_{\text{rms}}(\Delta L) = \sqrt{\frac{1}{M}\sum_{m}\left[S_I(\Delta L) - S_N(\Delta L)\right]^2} \tag{4.10}$$

where $\mathcal{E}_{\text{rms}}$ is the root mean squared error, M is the number of elements in the signal, S_I is the signal with the interference fringes, S_N is the signal without this interference, and ΔL is a dimensionless parameter related to the beam separation: $\Delta L = \Delta x/D$.

As the beam separation is increased, the error generally decreases. This is due to the suppression of the inter-beam interference fringes through aliasing. When the beam separation increases, eventually the period of the interference fringes falls below the extent of a single pixel. Within this single pixel, only the average value of that fringe is measured. If the beam separation is taken towards an infinite extent, then the averaging will be perfect

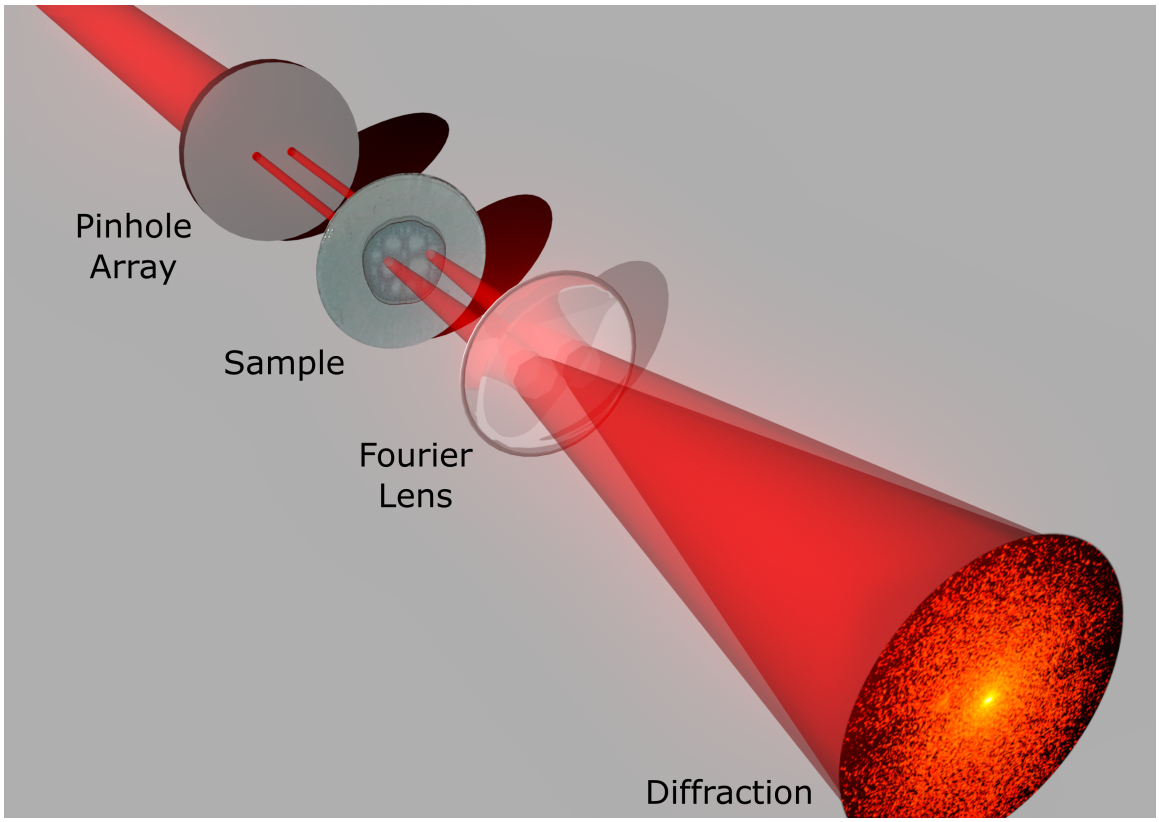

Figure 4.7: Setup for Aliased Autocorrelation Filtering Experiment. In order to test the aliased autocorrelation filtering technique, the pinholes are spaced far enough apart that the interference fringes produced from the separation alias on the detector. This separation is engineered so that the aliased frequency will permit autocorrelation filtering. These two beams are incident on a water lily stem and ptychography data are collected.

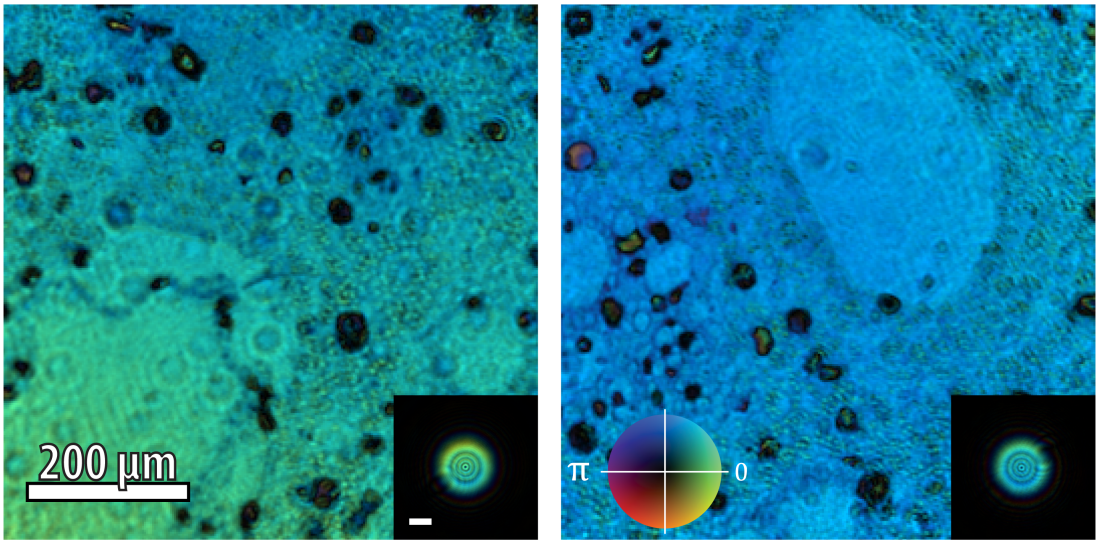

Figure 4.8: Reconstructions from Aliased Autocorrelation Filtering. The efficacy of the aliased autocorrelation filtering technique is demonstrated by reconstructing the field-of-view from each beam. Shown here are the reconstructed images of the water lily sample for the two regions illuminated in the aliased autocorrelation filtering experiment. The brightness is amplitude, the hue is phase. The scale bar for the probes is 200 μm.

and the fringes will add a constant value to every pixel. This is evident in the general decreasing trend of the error for larger ΔL; as the interference between the two beams is averaged away, the diffraction pattern approaches the case where the beams do not interfere.

If the pixel size is equal to an integer number of fringe periods, then there is no difference in the averaging of the fringes from one pixel to the next, thus the interference fringe appears as a uniform background. These beam separations are where the error drops to zero in figure 4.3. At these points, the aliasing naturally cloaks the inter-beam interference. The resulting diffraction pattern is the incoherent sum of the contributions from each beam, and can thus be reconstructed with multiple mode ptychography algorithms. These points occur when the beam separation is equal to a critical beam separation of

$$\Delta x_c = \frac{N\lambda z}{p} \tag{4.11}$$

where N is an integer.

Interference fringes at integer multiples of the sampling frequency are completely cloaked through aliasing. Fringes of a frequency close to this condition are not completely suppressed. These fringes are partially suppressed, however. This partial suppression is increased the more aliasing occurs. This is evident in the curve in figure 4.3 near the zeros. This gives the technique of alias cloaking improved resistance to misalignment as the beam separation is increased. Furthermore, as the beam separation is extended to extremely large values, the interference fringes are not detectable for any separation; thus any sufficiently large separation allows for alias cloaking.

Because the interference fringes are naturally suppressed, they do not require any space in the autocorrelation. Thus, the earlier restriction on the oversampling for autocorrelation filtering (that $\sigma \geq 4$) is lifted, and only the traditional oversampling requirements of CDI apply. This allows for the beam used in alias cloaking to be as large as is allowed by CDI techniques.

4.3.2 Experimental Demonstration

The feasibility for alias cloaking in multiple beam ptychography is tested experimentally. The setup for this experiment uses the laser system from figure 4.1 with the microscope setup shown in figure 4.9. The pinhole array for this experiment was designed with three holes in a linear pattern. These holes have a diameter of 1.26 mm and a separation of Δx =2.5 mm. This makes the oversampling $\sigma \approx 2$ and satisfies equation 4.11 with $N = 1$. Note that due to the relatively large peripheral error at this beam separation, this experimental setup depicts the least ideal scenario for alias cloaking.

The sample used in this experiment was a thin transverse slice of a rabbit testicle preserved in cedar wood oil [AmScope PS25]. An optical microscope image of this sample is shown in figure 4.10. On this sample, a 784 position ptychography scan was recorded with a step size of $D/12$ (105 μm) and a 20% random offset; this scan is shown in figure 4.11. This scan is a relatively large scan chosen so that the three fields of view overlap to image the entire sample. Since the diffraction limited resolution of each reconstruction is independent of the other beams, the high resolution of each image is maintained. This ultimately yields a high resolution, large field of view image.

The reconstructed images are shown in figure 4.12. In this figure, the three fields of view are stitched together to create one large image. In the original reconstructions, a quadratic phase was present across the image. This indicates slight curvature of the sample. This curvature was verified using measurements from a Zygo GPI XP laser interferometer. The interferometric phase data are shown in figure 4.13 along with a cubic fit to these data. The cubic fit shows that there is a quadratic phase. For display purposes, this quadratic phase has been removed from the image in figure 4.12.

Once this quadratic phase had been removed, the three different fields of view were stitched together. Because there were only three images, they could be registered manually. Once aligned the overlapped regions were averaged using a cosine smoothing, so that the

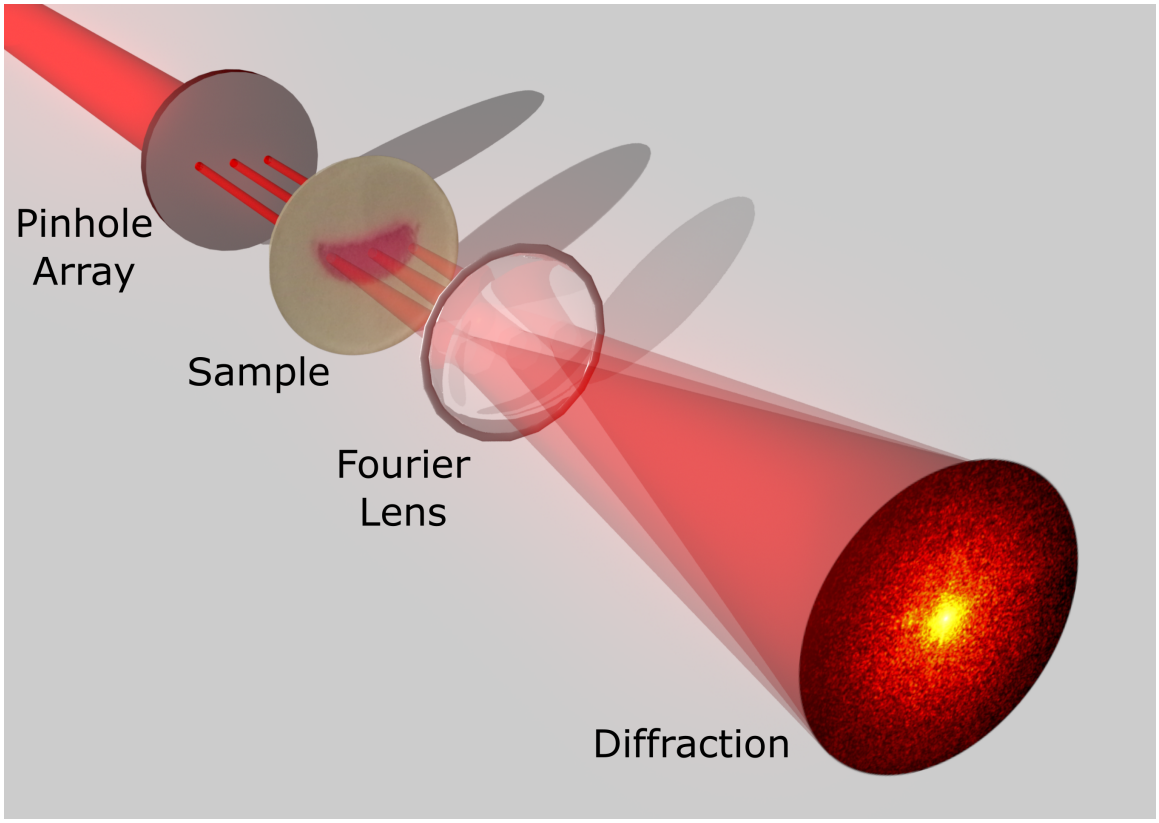

Figure 4.9: Experimental Setup for Alias Cloaking. The pinhole array is designed so that the maximum beam size allowed by CDI is achieved and so that the beam separation satisfies the conditions for alias cloaking. The beams are incident on a rabbit cell sample, and the diffraction pattern is measured. This diffraction pattern does not contain the interference fringes that arise from the inter-beam interference as those are suppressed through alias cloaking. This allows for the multiple mode ptychography algorithms to be used without any filtering.

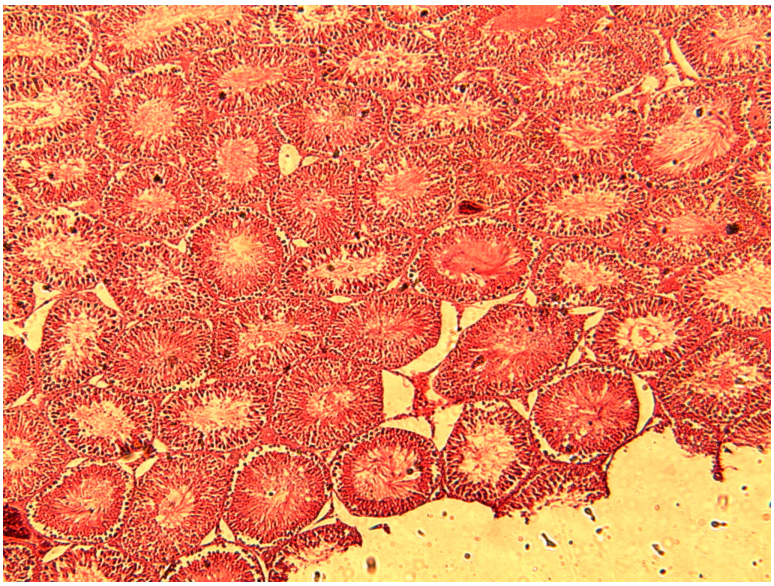

Figure 4.10: Optical Microscope Image of Rabbit Cells. Complementary image of the rabbit cells taken with a traditional optical microscope. The features observed in this image are likewise present in the CDI reconstructions.

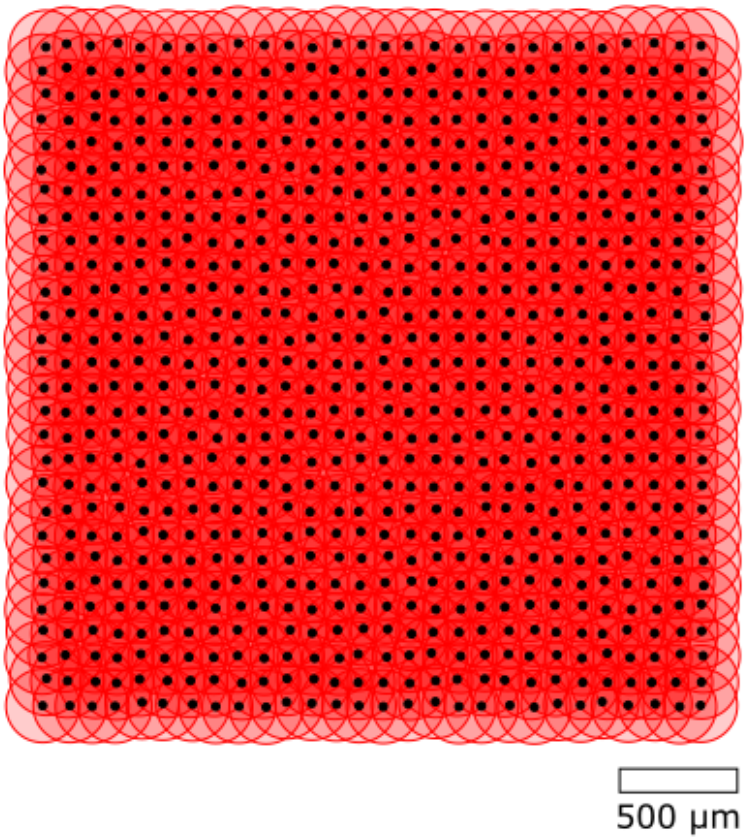

Figure 4.11: Rectilinear Ptychography Scan. The scan positions used in the ptychography scan of the rabbit cells are displayed as black dots. The overlapping red circles show the idealized extent of the probe at each of these positions. There is a 20% random offset from a perfect rectilinear grid in order to prevent artifacts.

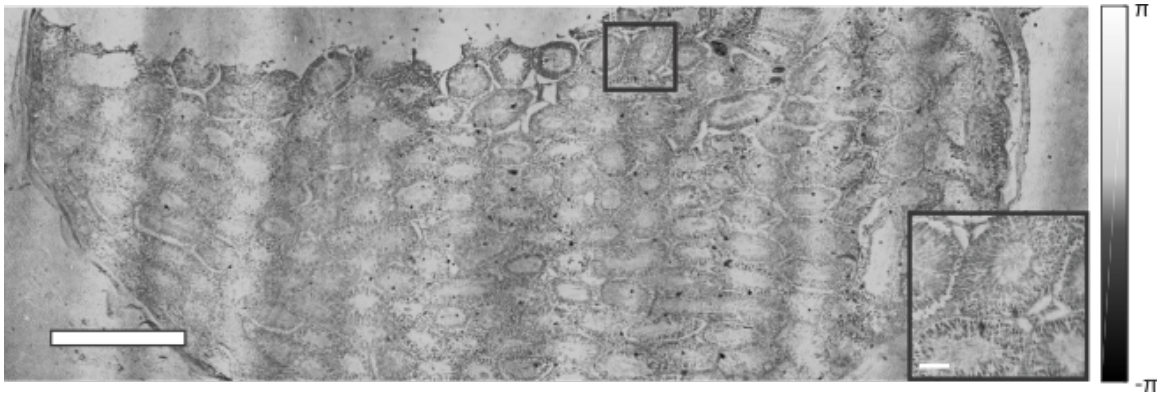

Figure 4.12: Alias Cloaking Ptychography Reconstruction. Using the alias cloaking technique, an extremely large field-of-view image can be measured in a single scan. This is the phase image of the rabbit cell sample. Three fields of view were stitched together to form this image. The individual images are the reconstructions from multiple beam ptychography with alias cloaking. The scale bar is 1 mm. Inset: a zoomed in region of the sample showing the fine features that are resolved. Scale bar 200 μm.

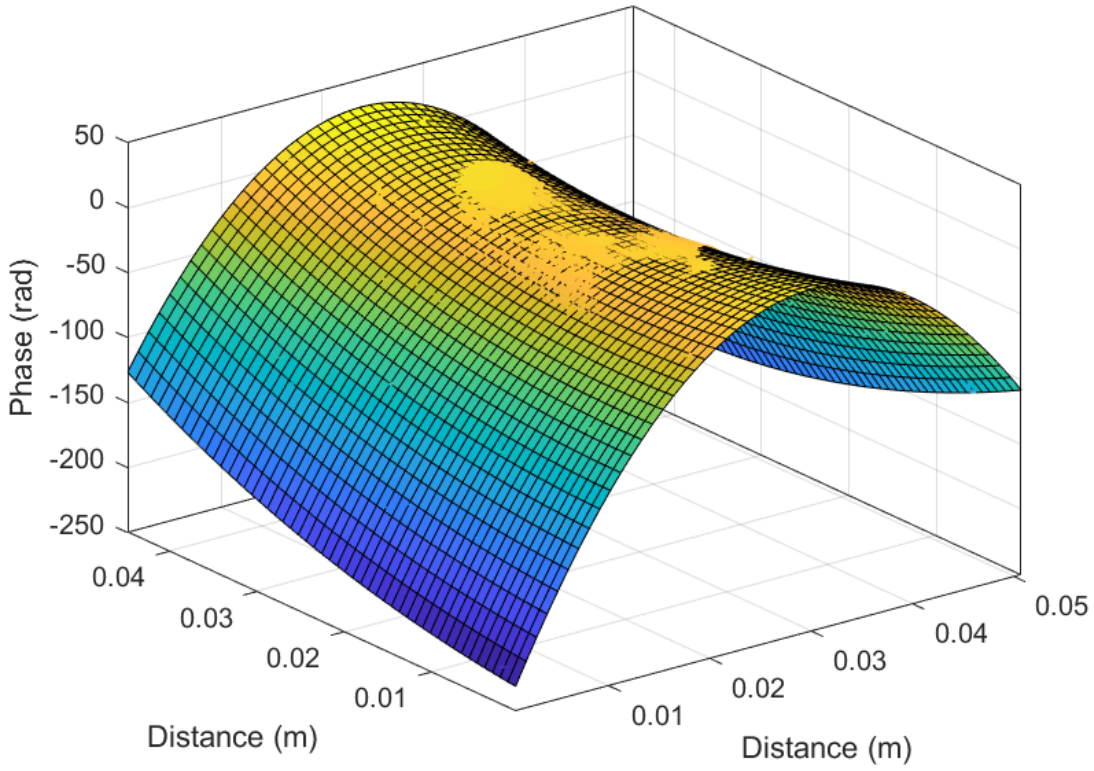

Figure 4.13: Laser Interferometry Data on Rabbit Cells. Phase data measured with a laser interferometer are shown along with a two-dimensional cubic fit to these data. This demonstrates that there is a quadratic phase present in the rabbit cell sample, which is consistent with the quadratic phase measured in the ptychography reconstructions.

overlap region further into each individual image was weighted more heavily than the overlap region closer to the periphery. This was done because the ptychography scan has more overlap in the interior of the scan and thus higher image quality.

4.4 Effect on Image Fidelity

In order to measure the effect these filtering techniques have on the reconstruction quality, an equivalent field of view is obtained using a multiple beam geometry and a single beam geometry. These reconstructions are shown in figure 4.15. By eye, the images look identical with the exception of the periodic modulation on the multiple beam reconstruction. Incidentally, that modulation is due to an anomalous back reflection on the detector and thus is not an effect of the multiple beam techniques.

To compare the two reconstructions, the phase retrieval transfer function [32, 245, 257] is used. This function is defined as

$$\mathrm{PRTF}(f_r) = \left\langle \frac{\left\langle \sum_n \left| \langle \psi_n^{rec}(x_j) \rangle_i \right| \right\rangle_j}{\left\langle \sqrt{I^{meas}(x_j)} \right\rangle_j} \right\rangle_\varphi \tag{4.12}$$

where $\psi_n^{rec}(x_j)$ is the jth reconstructed diffraction pattern generated by the nth probe, $I^{meas}(x_j)$ is the intensity measurement of the jth scan position, $\langle\rangle_m$ corresponds to an average over the parameter m, i iterates over the different beams, j is the scan position, φ is the azimuthal angle of the diffraction pattern. For this calculation, the phase retrieval transfer function calculation used 100 independent ptychography reconstructions consisting of 500 iterations apiece. The phase retrieval transfer function for the multiple beam reconstructions and for the single beam reconstructions are shown in figure 4.14. Typically, the resolution is calculated by the spatial frequency at which the phase retrieval transfer function falls below 0.5 [195]. For these reconstructions, the threshold occurs at similar spatial frequencies, which indicates that there is not an appreciable difference in the achieved resolution. The estimated spatial resolution from the phase retrieval transfer function is 2.85 μm for the multiple beam

reconstruction, and is 2.70 μm for the single beam reconstruction. The theoretical, Abbe diffraction limited resolution is 2.48 μm [242].

The different modalities are compared again using a calculation of the power spectral density. The power spectral density is a measure of the average power as a function of spatial frequency. This was calculated for identical fields of view for a single beam reconstruction and for a multiple beam reconstruction. The reconstructions used for this comparison are shown in figure 4.15, along with a plot of the power spectral densities. The two spectra are nearly identical; the average ratio between them is 0.98.

It is expected that due to the finite dynamic range of the detector, at some point an upper limit to the number of beams will be reached for multiple beam ptychography as is the case for multiplexed holography [55]. An experiment with four beams was performed using the alias cloaking method. The reconstructions from this experiment are shown in figure 4.16. The exact constraints on the upper limit are still unknown, but instead provide a fruitful avenue for further investigation.

Ptychographic imaging systems are inherently limited in their throughput because ptychography is a scanning technique. With these techniques to increase the throughput of ptychography without compromising resolution and image fidelity, the applicability of ptychography is improved.

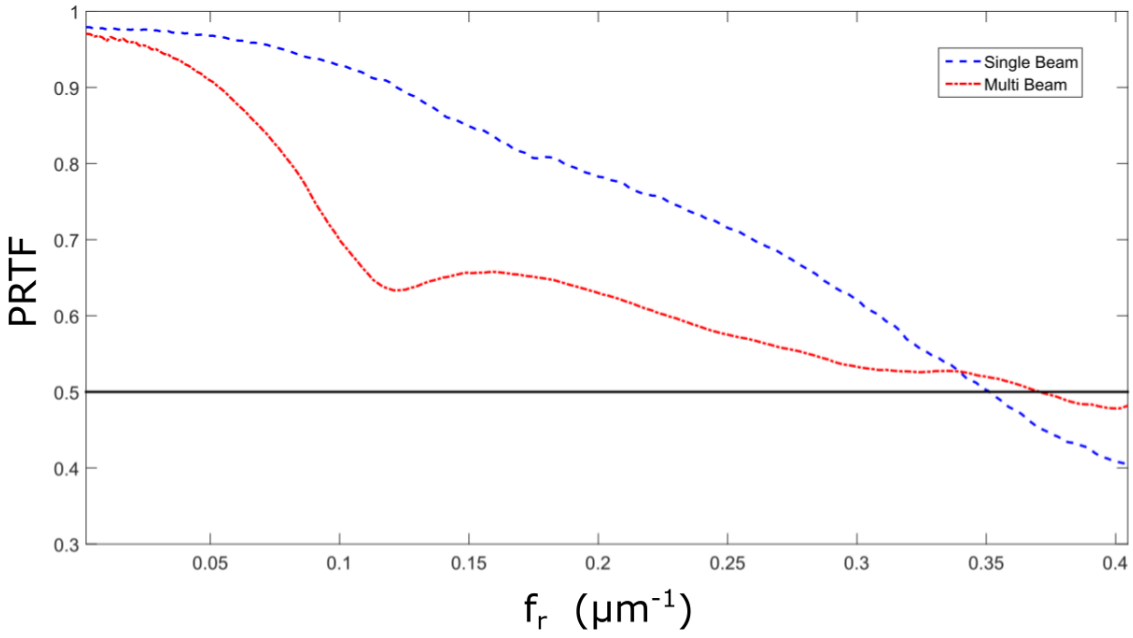

Figure 4.14: Comparison of Resolution in Multiple Beam Ptychography. The phase retrieval transfer function is plotted as a function of spatial frequency. A value of 0.5 is typically used as the cutoff for the resolution. For multiple beam ptychography, this threshold is met at a slightly higher spatial frequency than for single beam ptychography indicating a roughly equivalent resolution.

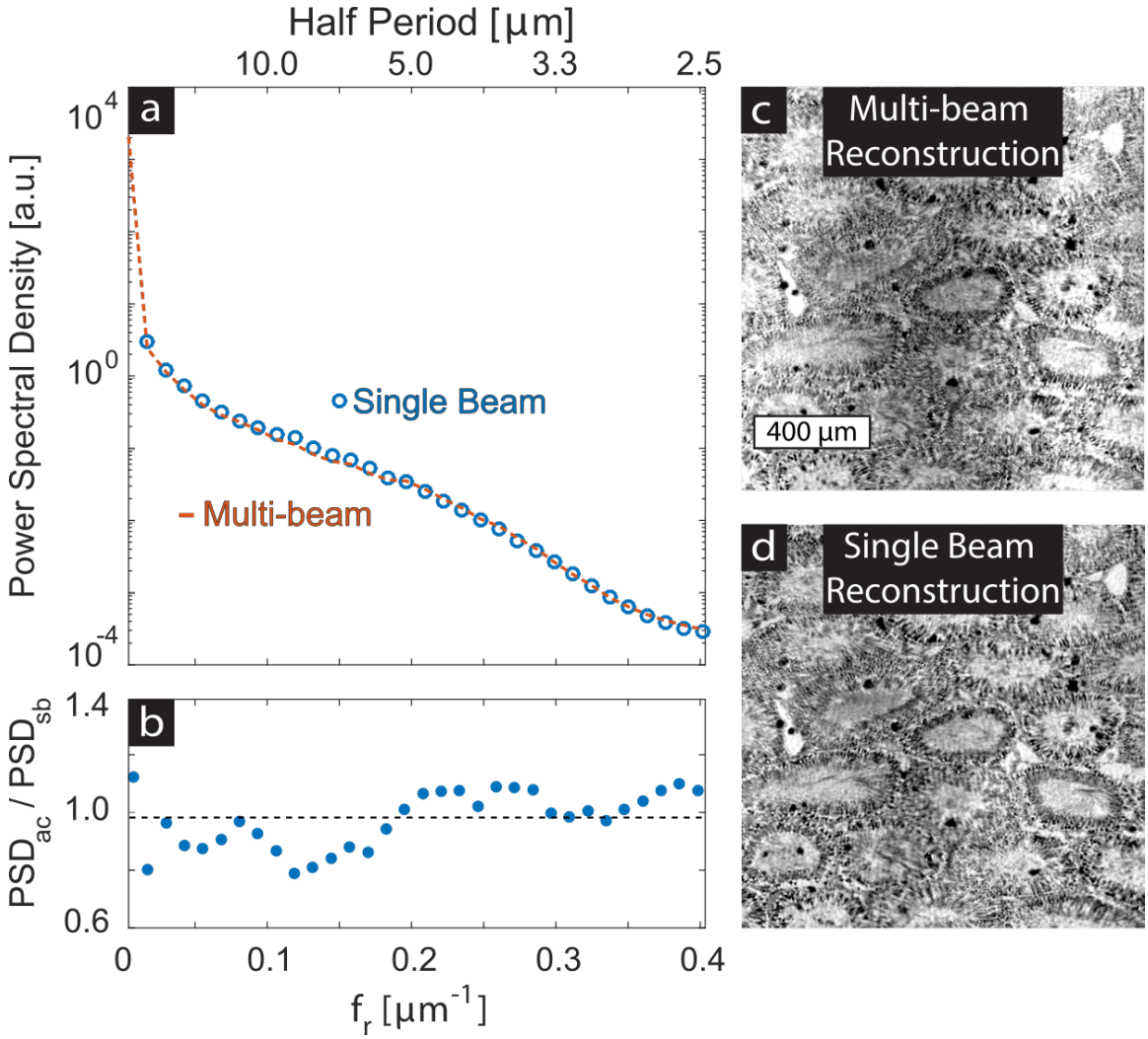

Figure 4.15: Comparison of Power Spectral Density in Multiple Beam Ptychography. (a) The power spectral density for a multiple beam reconstruction and a single beam reconstruction. (b) The ratio of the two power spectral densities. (c-d) The equivalent reconstructions used in this comparison. The similarity of the power spectral density demonstrates that the use of multiple beams does not degrade image quality.

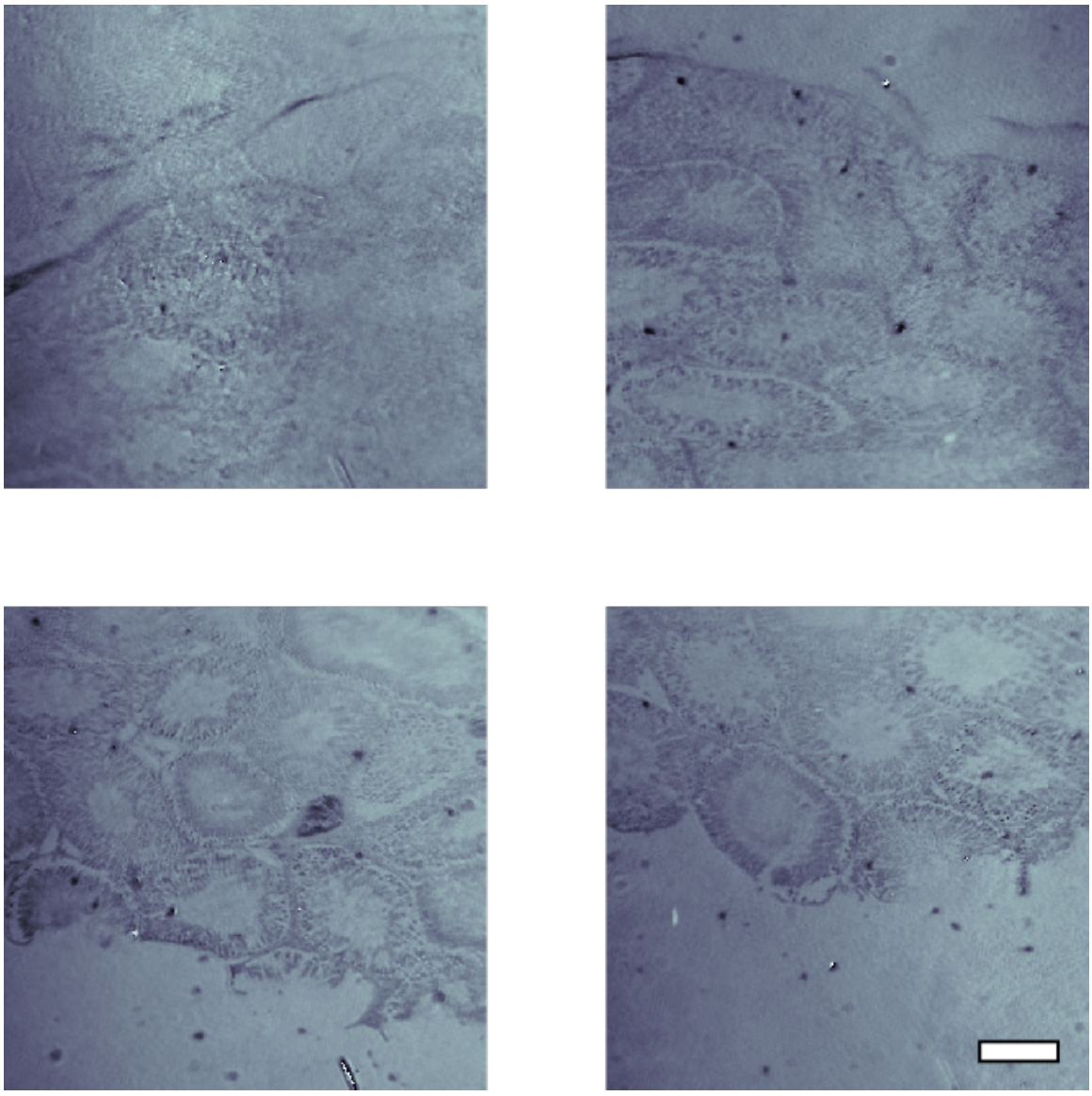

Figure 4.16: Four Beam Ptychography Reconstruction. Using a pinhole array that has four holes in a square formation, a multiple beam ptychography scan was recorded using alias cloaking. These are the four reconstructed fields of view. The sample in this experiment was the same rabbit sample as in figure 4.12. This reconstruction demonstrates that the upper limit to the number of beams permissible in multiple beam ptychography is at least 4. The scale bar is 200 μm.

Chapter 5

High Harmonic Generation

5.1 Introduction

In this chapter, we review the development of high harmonic generation (HHG) and some of the considerations for an HHG source. A more detailed can be found in [108].

The process of high harmonic generation [65, 118, 130, 138, 156] is a highly nonlinear process in which a high intensity, ultrashort laser pulse interacts with a material, usually a gas, and the emitted light has a much higher energy than the input light. The polarization and coherence of the light are preserved, and the duration of its pulses reduced [131]. In this chapter, the history of the development of high harmonic generation is discussed, along with a more detailed examination of one model for the high harmonic process, the three step model [44], then the concept of phase matching in a hollow-core fiber [198] is discussed.

5.2 Development of High Harmonic Generation

High harmonic generation was first experimentally demonstrated using early picosecond and femtosecond lasers [65, 156]. The field of high harmonic generation was greatly impacted by developments in the driving laser technology. One such development is the Ti:Sapphire laser system originally developed by Moulton [167]. Due to the broad bandwidth of the Ti:Sapphire crystal, extremely short pulses of duration well below 30 fs can be generated from these oscillators [221, 261]. Pulses of such short duration are one ingredient to creating extremely bright, broadband, infrared sources. Another ingredient is the development of

chirped pulse amplification [145, 178, 225], wherein the pulse is stretched in time, amplified through stimulated emission, and then recompressed. These high power, broad-bandwidth infrared sources are important for developing bright high harmonic sources. One example of such a bright source is a multi-pass Ti:Sapphire ring amplifier [10, 11].

High harmonic generation has been achieved in many modalities other than the gas jet modality used in early works. Harmonics can now be generated from solids [79, 170], plasmas [231] and gas filled waveguides [52, 198]. Further development of high harmonic generation has allowed for the creation of light in the water window [29, 36, 222], for the generation of hard x-ray (>1 keV) light [181, 209], for the creation of isolated attosecond bursts [37, 38, 180, 202], for circular and elliptically polarized harmonic light [56, 59, 63, 66, 112], and for harmonic light with orbital angular momentum [70, 187].

5.3 Three Step Model

The three step model [44] is a simplified description of the high harmonic process that ignores many of the quantum mechanical considerations involved in a more detailed explanation [129]. However, this understanding is intuitive and the phenomenology derived from it is sufficiently accurate for many applications.

The three step model looks at the interaction of the ultrashort light pulse with a single atom. The three steps in question are: partial ionization of the atom, the acceleration of the electron in the electromagnetic field, and the recombination of the electron and ion, resulting in the emission of a high energy photon.

The energy of this emitted photon is determined by the ionization energy of the atom involved in the process and the amount of kinetic energy the electron absorbs when in the electric field. The equation of motion for the electron in the electric field is given by

$$m_e \ddot{x} + eE_0 \cos(\omega t) = 0 \tag{5.1}$$

where m_e is the electron mass, x is the electron position, e is the electron charge, E_0 is

the magnitude of the electric field, ω is the frequency of the electric field, and t is the time coordinate. Integrating this equation yields the electron trajectory

$$x = \frac{eE_o}{m_e\omega^2}\left[(\cos(\omega t) - \cos(\omega t_i)) + (\omega t - \omega t_i)\sin(\omega t_i)\right] \tag{5.2}$$

where t_i is the initial time: the time of ionization. One can define a new time coordinate $\tau = t - t_i$, the time since ionization, thus the equation of motion becomes

$$x = \frac{eE_o}{m_e\omega^2}\left[(\cos(\omega\tau + \omega t_i) - \cos(\omega t_i)) + (\omega\tau)\sin(\omega t_i)\right] \tag{5.3}$$

Depending on the specific position in the electric field where the atom is ionized, the initial velocity of the electron will be different. Some example trajectories are shown in figure 5.1. When the electron recombines with the ion, the excess energy is released as a photon. The energy of that photon will be the ionization energy plus the kinetic energy of the electron.

The highest possible energy light that can be generated in this process can be computed by calculating the highest kinetic energy that a recombining electron may have. This is equivalent to maximizing the velocity of the electron under the condition that the electron position is zero, i.e. the position of the parent ion.

$$\dot{x} = \frac{-eE_o}{m_e\omega}\left[\sin(\omega\tau + \omega t_i) - \sin(\omega t_i)\right] \tag{5.4}$$

$$x = \frac{eE_o}{m_e\omega^2}\left[(\cos(\omega\tau + \omega t_i) - \cos(\omega t_i)) + (\omega\tau)\sin(\omega t_i)\right] = 0 \tag{5.5}$$

Many solutions to these equations are shown in figure 5.2, which shows the maximum kinetic energy as a function of the initial phase of the electron. The peak value of this distribution is 3.17 times the ponderomotive energy, given by

$$U_p = \frac{2e^2}{c\epsilon_0 m_e}\frac{I}{4}\frac{\lambda^2}{4\pi^2c^2} \tag{5.6}$$

where I is the peak intensity of the driving field.

The physical system used in this thesis consisted of a $2\ \mathrm{W}/m^2$ peak intensity Ti:Sapphire laser with a central wavelength of roughly 800 nm. From this, the ponderomotive energy is

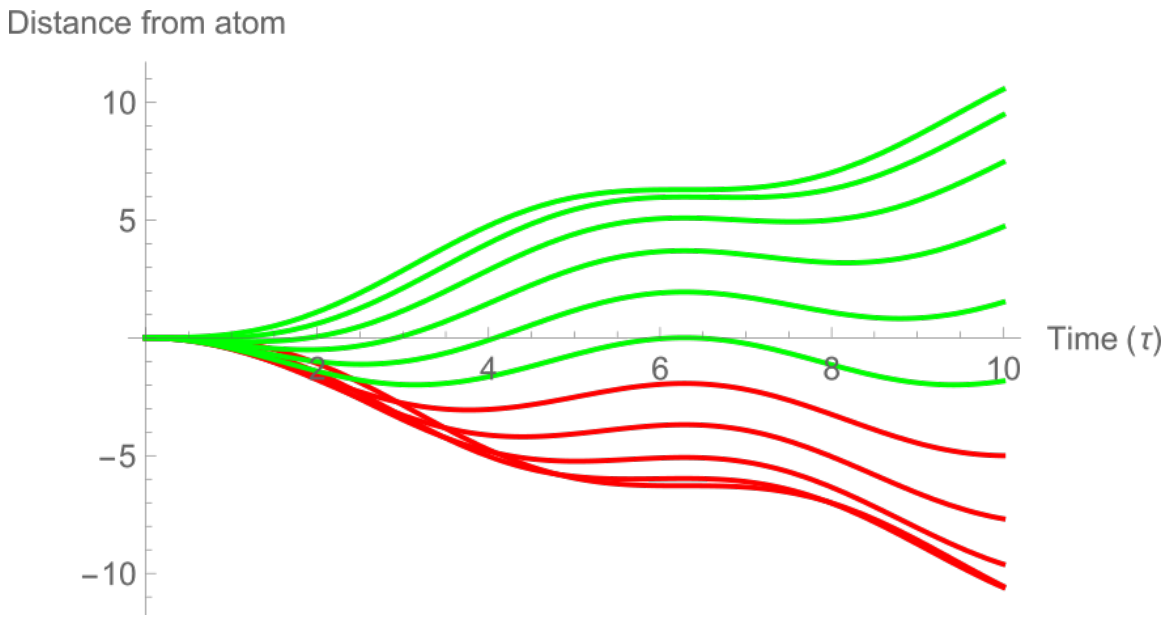

Figure 5.1: Electron Trajectories During High Harmonic Generation. The green trajectories lead the electron to recombine with the parent ion, the red do not. The energy of the emitted photon is based on the kinetic energy of the recombining electron, and thus the slope of the trajectory at its zero. By examining all of the possible trajectories, the maximum kinetic energy at recombination can be elucidated.

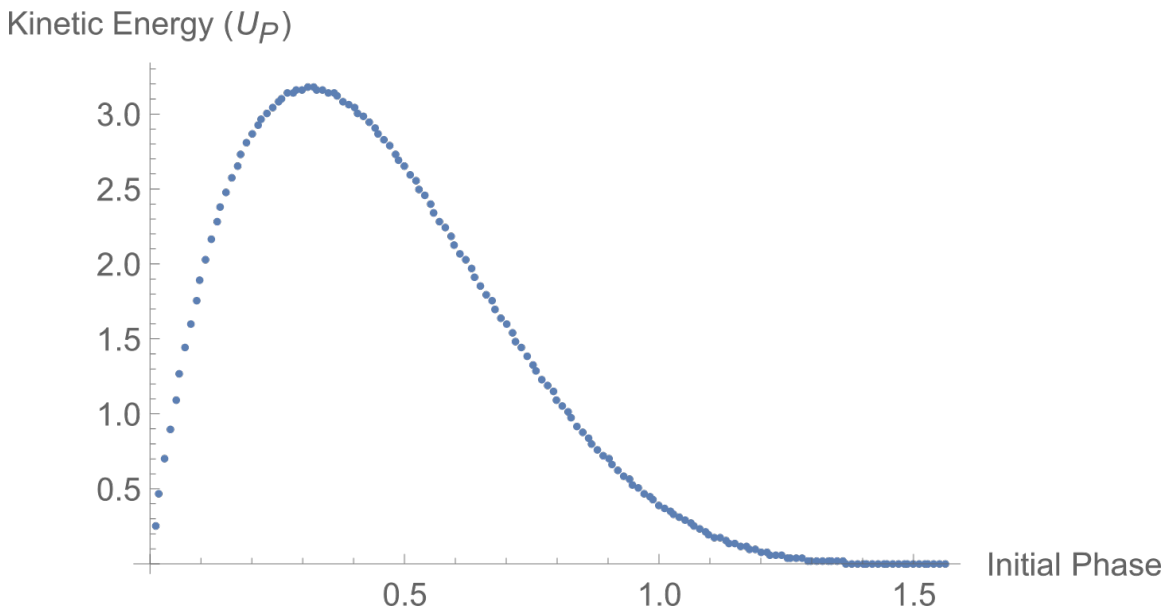

Figure 5.2: Spectrum of HHG Cutoff Energies. These are the kinetic energies that the electron will have during recombination should the electron leave the parent atom with the given phase. The peak of this spectrum has a kinetic energy of 3.17 times the ponderomotive energy, giving an upper limit on the energy of the high harmonic photon.

calculated to be 11.8 eV. Thus, for harmonics generated in argon, which has an ionization potential of 15.76 eV, the cutoff energy is 53 eV. The work done with argon harmonics in this thesis was done at approximately 43 eV.

5.4 Phase Matching

The section above details a single atom description of the HHG process. In order to generate a usable extreme ultraviolet (EUV) beam, it is helpful for the light emitted from multiple atoms to be in phase [16, 57, 175, 198]. If the light is out of phase between atoms, then there will be destructive interference, greatly reducing the overall intensity of the EUV beam.

In order to guarantee that the phases are matched, it is useful to look at the k vectors for the driving infrared light and for the generated EUV light. If the two k vectors are equal in the direction of propagation, then all of the generated EUV light will be in phase.

The expression for the k vector of the infrared light contains five terms. These terms are for the effects of the vacuum, the neutral gas, the nonlinear index of refraction of the neutral gas, the plasma, and the waveguide. With all of these terms, the k vector can be written

$$k = \frac{2\pi}{\lambda} + \frac{2\pi P(1-\eta)\delta(\lambda)}{\lambda} + (1-\eta)n_2 I - P\eta N_{atm} r_e \lambda - \frac{u_{11}^2 \lambda}{4\pi a^2} \tag{5.7}$$

where P is the pressure of the gas in the capillary, η is the ionization fraction, δ is the difference from unity of the index of refraction per unit pressure, n_2 is the nonlinear index of refraction, N_{atm} is the number density of electrons at a pressure of 1 atm, r_e is the classical electron radius, u_{11} is a geometric constant from the waveguide coupling [149], and a is the radius of the waveguide [198]. This expression is valid for both the driving light and the resulting EUV light, with the caveat that some terms are negligible for the EUV light.

In order to have phase matching throughout the entire waveguide, the k vector of the infrared light and the extreme ultraviolet light must be equal. Further, the nonlinear term is

taken to be sufficiently small as to be neglected. The phase matching condition thus becomes

$$\Delta k \approx q\left(\frac{u_{11}^2\lambda}{4\pi a^2}+\frac{2\pi P(1-\eta)}{\lambda}\left[\delta\left(\frac{\lambda}{q}\right)-\delta(\lambda)\right]+P\eta N_{atm}r_e\lambda\right) \tag{5.8}$$

where q is the harmonic order in question (Due to the symmetries in the system, only odd values of q are allowed [5]). In order for the phase matching condition to be met (i.e. $\Delta k = 0$), the pressure may be adjusted. This phase matching pressure is calculated by solving equation 5.8 at the phase matching condition, yielding

$$P=\frac{u_{11}^2\lambda^2}{4\pi a^2\left(2\pi(1-\eta)\left[\delta(\lambda)-\delta\left(\frac{\lambda}{q}\right)\right]-\eta N_{atm}r_e\lambda^2\right)} \tag{5.9}$$

The nature of this fraction allows for values of the ionization for which the denominator goes to or below zero. In these situations, the pressure required for phase matching diverges, and thus phase matching cannot occur. The ionization at which phase matching first becomes impossible is the critical ionization. This can be calculated by setting the denominator of equation 5.9 to zero. Thus, the critical ionization is

$$\eta_c=\frac{2\pi\left[\delta(\lambda)-\delta\left(\frac{\lambda}{q}\right)\right]}{N_{atm}r_e\lambda^2} \tag{5.10}$$

where η_c is the critical ionization fraction.

Chapter 6

Scatterometry and Imaging of Colloidal Crystals

6.1 Introduction

A colloidal crystal is an arrangement of nano-scale particles that self-assembled into a structure with long range order [54, 76]. An example of this is naturally occurring opals, which are composed of a periodic arrangement of silica spheres [106, 201]. It is possible to use a colloidal crystal as a template for a porous material by infiltrating the gaps in the crystal structure with a different material, then removing the colloidal crystal [223, 240].

Three-dimensional colloidal crystals and materials that use them as templates have diverse thermal, electronic, and magnetic properties [199], and thus show promise for applications in thermoelectronics, nano-electronics, photovoltaics, and nano-enhanced therapies [15, 22, 85, 86, 117, 134]. The materials engineered using colloidal crystals have the promise to go beyond the material properties of natural materials by changing the alloy or multi-layer composition. The design of these materials relies heavily on the ability to characterize these emergent properties. One important tool for studying the local structure of colloidal crystals is coherent x-ray scattering and imaging [162].

The angular cross-correlation function [6, 122] has been used at synchrotron facilities to retrieve structural information from coherent x-ray scattering patterns of glassy polymethylmethacrylate spheres, revealing information on local symmetries [127, 250, 251]. The combination of this angular cross-correlation function with small angle scattering was used to investigate orientation heterogeneities in films of silica spheres of various sizes [206]. On

the other hand, these techniques have been applied to electron diffraction [124] to probe the order of ligands in a two-dimensional supracrystal of dodecanethiol-capped gold nanoparticles [147]. This analysis was also used with transmission electron microscope diffraction to study the helical-to-skyrmion magnetic phase transition in Cu_2OSeO_3 [184].

Previous work with extreme ultraviolet (EUV) light has imaged sparse 2 μm silica spheres [53] and achieved a spatial resolution between 250 nm and 440 nm. In this chapter, experiments using a high harmonic source to study the structure of colloidal crystals at sub-100 nm length scales are presented. First the tabletop apparatus to create and measure diffraction with 13 nm light is described, followed by a description of the angular cross-correlation function and the diffraction analysis using it. Finally, full-field quantitative coherent diffractive imaging is presented with better than 20 nm resolution. We have published these results in [146].

6.2 Experimental Setup

The experimental apparatus is shown in figure 6.1. The harmonic source is driven by a 20 fs, 2 mJ, 3 kHz Ti:Sapphire laser centered at 785 nm [KMLabs Dragon]. This light was focused into a 150 μm diameter, hollow waveguide filled with 575 torr of helium, generating extreme ultraviolet light at 13.5 nm [KMLabs XUUS4]. The residual driving infrared light was separated from the 13 nm light using a pair of ZrO_2 coated Si mirrors near Brewster's angle, and a 400 nm Zr foil filter. Multiple harmonics are generated in the high harmonic generation process; a single harmonic was selected by a pair of Si/Mo multi-layer mirrors. The first mirror is flat and the second has a 100 mm radius-of curvature to focus the 13.5 nm harmonic onto the sample. There is slight astigmatism on the beam due to the non-zero angle of incidence. To account for this, the sample was placed between the horizontal and vertical foci, yielding a beam of approximately 5 μm in diameter.

The sample for this experiment is a colloidal crystal made by dropcasting monodispersed silica nano-spheres onto a 30 nm thick silicon nitride membrane. A scanning electron

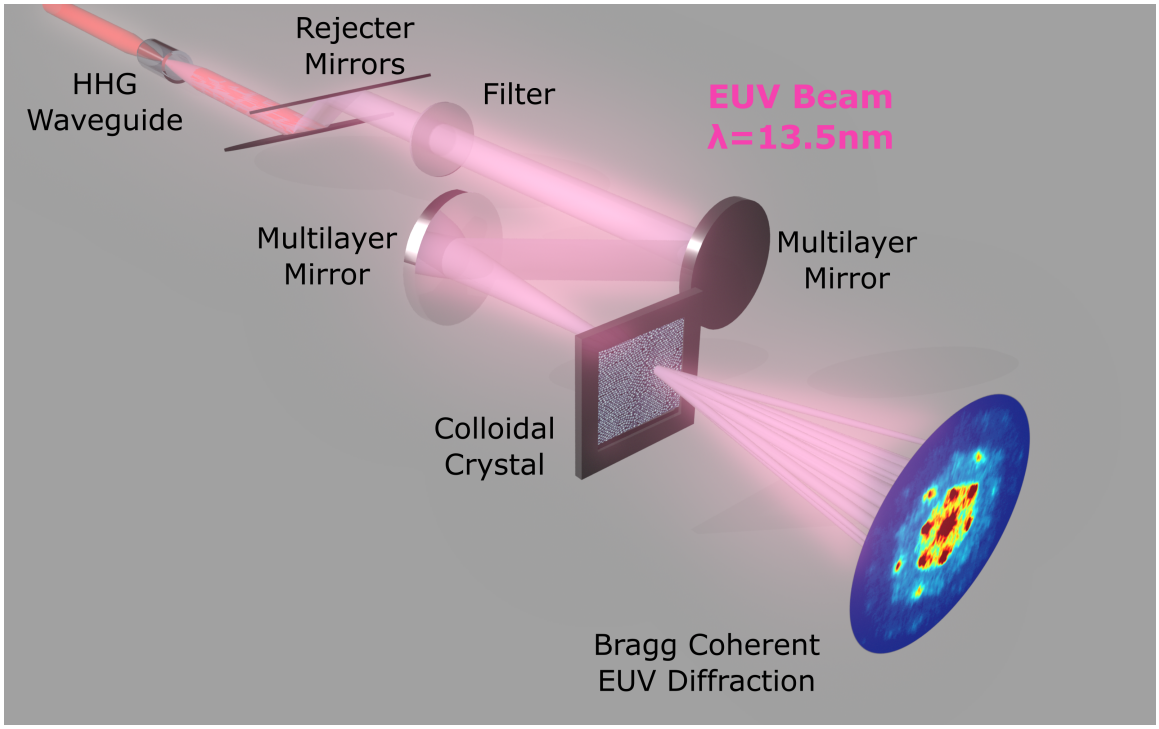

Figure 6.1: Schematic for Colloidal Crystal Characterization. Coherent extreme ultraviolet light is created through high harmonic generation in a waveguide. The driving infrared light is filtered using a pair of ZrO_2 coated Si mirrors and a thin Zr filter. The beam is focused onto the colloidal crystal using a pair of multi-layer mirrors and the scattered light is recorded on a CCD camera.

microscope (SEM) image of these spheres is shown in figure 6.2. In this image, the diameter of the spheres can be seen to be 123±3 nm. Further, the dispersion of the spheres can be seen. The left section of the sample has very dispersed spheres, the center has a densely packed monolayer of spheres, and the right side has a tightly packed three-dimensional multi-layer of spheres.

The 13.5 nm light interacts with the colloidal crystal sample and diffracts. This diffracted light propagates 18.3 mm and is incident on a charge-coupled device (CCD) camera [Andor iKon] with 2048x2048 pixels that are 13.5 μm × 13.5 μm in size. As the colloidal crystal sample is moved relative to the beam, different diffraction patterns are measured depending on the local structure of the sample. This is shown schematically in figure 6.3.

Diffraction patterns were collected from the left and right regions in figure 6.2. The patterns were collected in a series of twenty frames with no binning on the camera at a readout rate of 1 MHz. The exposure times were 12 sec for the right region, and 3.5 sec for the left region. The total fluence of extreme ultraviolet light incident on the sample is less than 4 μJ/cm^2, and is thus classified as a non-destructive measurement of the colloidal crystal. The diffraction patterns measured in this way are shown in figure 6.4.

By casual observation of the diffraction patterns in figure 6.4, one can see that the diffraction from the ordered region has a strong six-fold symmetry, while that from the sparse region does not.

The diffraction pattern of the multi-layer region contains multiple Bragg peaks due to the long-range order in the colloidal crystal. These colloidal self-assemblies typically organize into hexagonal close-packed or face-centered cubic structures [217]. Larger systems containing more than two layers tend to form a combination of these two types, forming a random close-packed structure due to the low difference in free energy between the two configurations [157]. In order to verify that the diffraction is from the trilayered region of the sample, a comparison was made between the diffraction and the SEM image. A sub-region of the SEM image (shown in figure 6.4) was selected to have the characteristic multi-layer

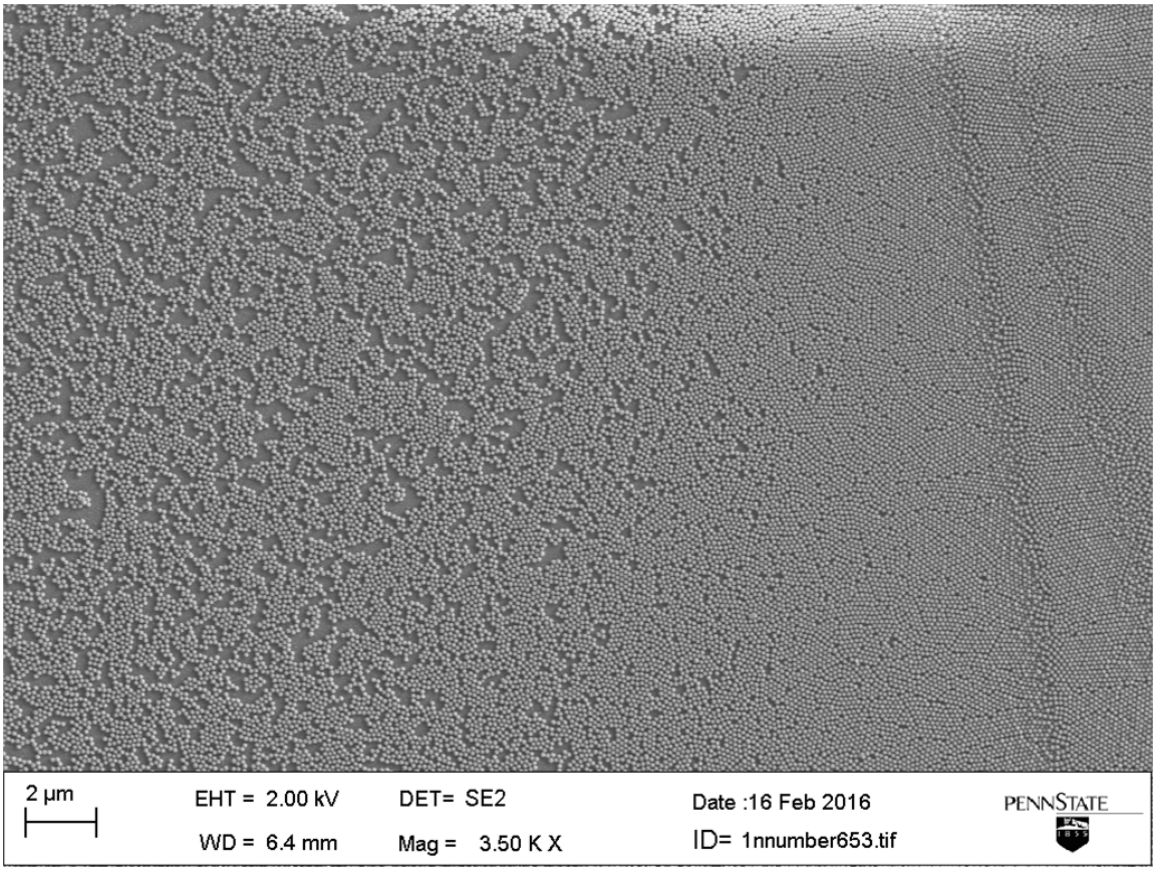

Figure 6.2: Scanning Electron Microscope Image of Colloidal Crystal. The image shows three distinct regions: left: sparsely packed monolayer of silica spheres; center: tightly packed monolayer of spheres; right: dense, three-dimensional stacking of spheres.

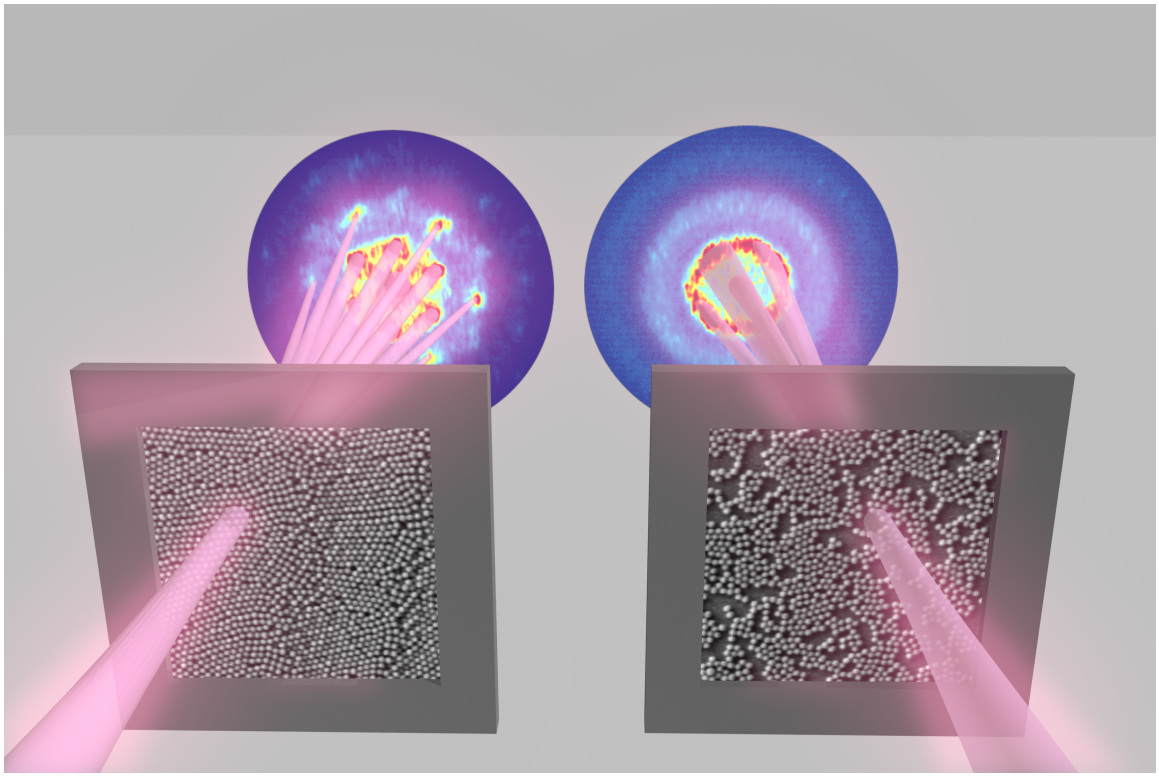

Figure 6.3: Schematic of Small Angle EUV Scattering Experiment. As the extreme ultraviolet light is incident on different parts of the sample, the local structure of the colloidal crystal will cause the diffraction pattern to form differently. A well ordered structure (left) will cause distinct Bragg peaks to form, while a less orderly structure (right) will form a Debye-Scherrer ring instead.

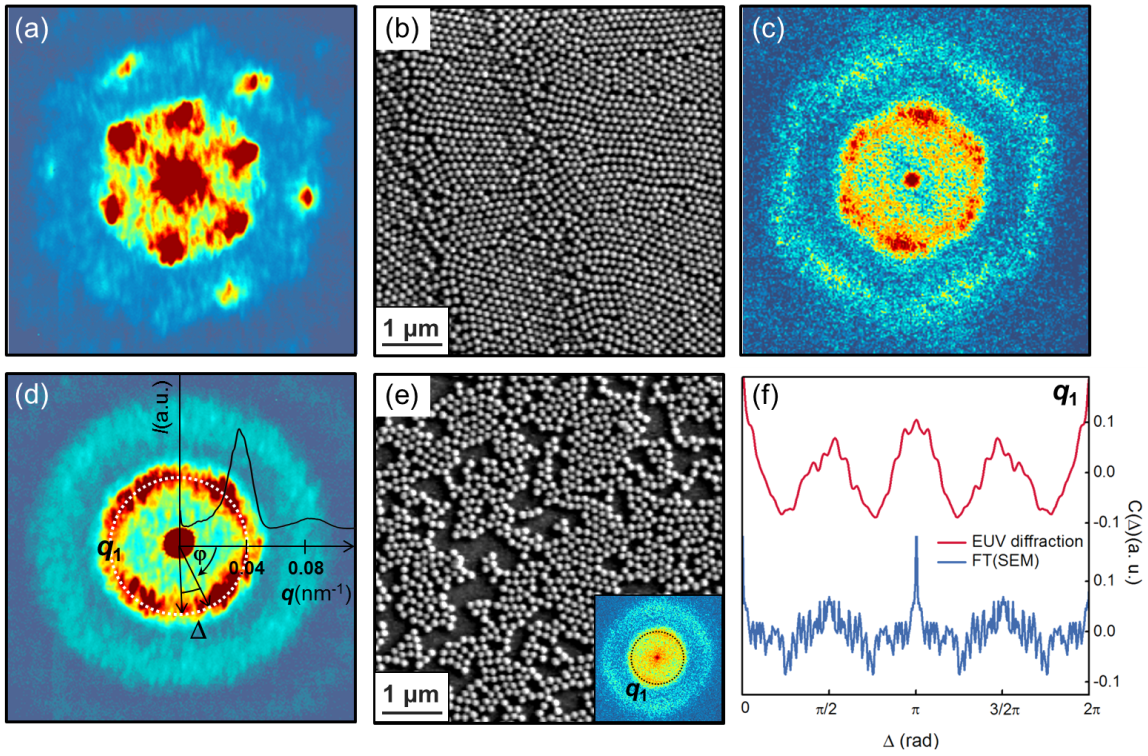

Figure 6.4: Diffraction Pattern Analysis of Colloidal Crystals. (a) Diffraction pattern from multi-layer region of colloidal crystal. (b) SEM image of this multi-layer region. (c) Fourier transform of (b). The six-fold symmetry present in the diffraction pattern is likewise present in this image. (d) Diffraction pattern measured from sparse region of colloidal crystal. (e) SEM image of this sparse region. Subset: Fourier transform of the SEM image of the sparse region. (f) Comparison of the angular cross-correlation of the EUV diffraction and the Fourier transform of the SEM image for the sparse region. Both of these measurements show the same four-fold symmetry, indicating order in the structure of the silica spheres.

stacking and to have an area equal to that of the EUV beam (5 μm diameter). A Fourier transform was performed on this sub-region, yielding the simulated diffraction pattern shown in figure 6.4 [125]. In this simulated diffraction pattern, the same six-fold symmetry in the Bragg peaks is easily observed.

The diffraction from the sparse region shows instead a Debye-Scherrer ring, which is typical of a more disordered crystal. The radial intensity distribution is

$$I(q) = \frac{1}{2\pi} \int I(q, \varphi) d\varphi \tag{6.1}$$

where I is the intensity, q is the radial coordinate of the detector, and φ is the angular coordinate of the detector (as shown in figure 6.4). The resulting distribution is shown as the overlay in figure 6.4. By locating the peak of this distribution, the inter-sphere spacing is measured to be $d_1 = 149 \pm 2$ nm. This value is larger than that measured from the SEM image (123±3 nm), indicating that the spheres are not as tightly packed as possible, instead there is space between the spheres.

This diffraction pattern was compared to the SEM image in the same fashion as the other diffraction pattern. A sparse region of the SEM image was selected and the Fourier transform of that region was calculated (Figure 6.4). This simulated diffraction pattern also shows Debye-Scherrer rings of the same radii. Thus the diffraction pattern is indeed from a sparse region characterized by disorder.

6.3 Angular Cross-Correlation

The diffraction pattern contains information that is associated with the local arrangement and symmetry of the assembly's structure. Thus, we can use the diffraction pattern to characterize the order of the sample, even in this predominantly disordered region. In order to quantify the order in this diffraction pattern, the angular cross-correlation function [6, 122, 123] is used. A schematic defining the coordinates used for the angular cross-correlation is shown in figure 6.4. At a given scattering radius q_1, the intensity at one angle

φ is compared to the intensity at a different angle $\varphi + \Delta$. This is done for every angle φ and for every angular separation Δ. Taking an average over the initial angle φ yields an expression that is a function of the angular separation Δ. This is the angular cross-correlation and it can be expressed in a normalized form as

$$C_{\text{norm}}(\Delta) = \frac{\langle I(q_1, \varphi) I(q_1, \varphi + \Delta) \rangle_\varphi - \langle I(q_1, \varphi) \rangle_\varphi^2}{\langle I(q_1, \varphi) \rangle_\varphi^2} \tag{6.2}$$

where $\langle \cdot \rangle_\varphi$ denotes an average over φ. This function can more readily be computed using Fourier transforms over the angular dimension [124, 147] so that the non-normalized form is

$$C(\Delta) = \langle I(q_1, \varphi) I(q_1, \varphi + \Delta) \rangle_\varphi = \mathcal{R} \left(\mathcal{F}_\varphi^{-1} \left(\left| \mathcal{F}_\varphi \left(I(q_1, \varphi) \right) \right|^2 \right) \right) \tag{6.3}$$

The angular cross-correlation is calculated for the EUV diffraction from the sparse region of the sample. This is shown in figure 6.4 along with the angular cross-correlation of the Fourier transform of the SEM image of a similar sparse region. Both of these cross-correlation functions show a four fold symmetry. This reveals that while the colloidal crystal is disordered, there is still some intrinsic ordering to the structure, in this case, a four-fold symmetry instead of a six-fold symmetry.

The order of the colloidal crystal is further studied by computing the angular cross-correlation at different length scales. This gives insight into the change in the structure from its local packing to its long range order. Figure 6.5 shows a diffraction pattern from the center monolayer region of the sample. This region is characterized by close-packed spheres in various different grains on the order of 1 μm. In order to measure structure at these length scales, the extreme ultraviolet beam size was increased to 15 μm and the sample was placed 15.1 mm from the detector. The diffraction pattern was acquired from 30 frames with a 9 sec exposure time with no binning and a 1 MHz readout rate.

The diffraction pattern is compared to the SEM image of the sample in this region using the same procedure as above. In this case, the Debye-Scherrer ring is observed at the same scattering angle.

The angular cross-correlation function is computed at two different scattering angles. The first is at the Debye-Scherrer ring, where the four fold symmetry was observed. The second is at very small scattering angle, close to the undiffracted light. These two scattering angles correspond to the inter-sphere spacing of 125±2 nm and a spacing of approximately 1 μm, which corresponds to the grain size in this region. The angular cross-correlation function for the Debye-Scherrer ring (scattering angle q_1) is shown in red in figure 6.5. There is a clear six-fold symmetry which corresponds to the close packing of the silica spheres. This is the same symmetry observed in the dense, multi-layer region of the colloidal crystal. Furthermore, the Fourier transform of the SEM image shows this same six-fold symmetry at this scattering angle. At the second scattering angle, q_2, which corresponds to 1 μm length scales, a four-fold symmetry is observed in the angular cross-correlation function. This means that the grains are rectangularly arranged while the spheres within them are hexagonally arranged. This four-fold symmetry is tested against a diffraction pattern of the direct beam without sample interaction (Figure 6.6). The angular cross-correlation of the direct beam does not show this four-fold symmetry, confirming that the symmetry arises from the sample and not from the extreme ultraviolet beam.

6.4 Coherent Diffractive Imaging

In order to directly probe the structure of the colloidal crystal, coherent diffractive imaging is employed. A ptychography dataset is recorded in a rectilinear pattern with 30% random offsets to prevent periodic artifacts [208, 233]. 81 scan positions were collected with 1.2 μm spacing between them. At each position, two frames were averaged with a 4 sec exposure time for each with no binning on the camera and a 1 MHz readout rate. The EUV beam was measured with a knife-edge test to be 5 μm in diameter. The sample was placed 18.3 mm from the sensor.

The sample is reconstructed using the ePIE algorithm [143] with modulus enforced probe [74] for a total of 3350 iterations with 750 iterations of a position correction algorithm

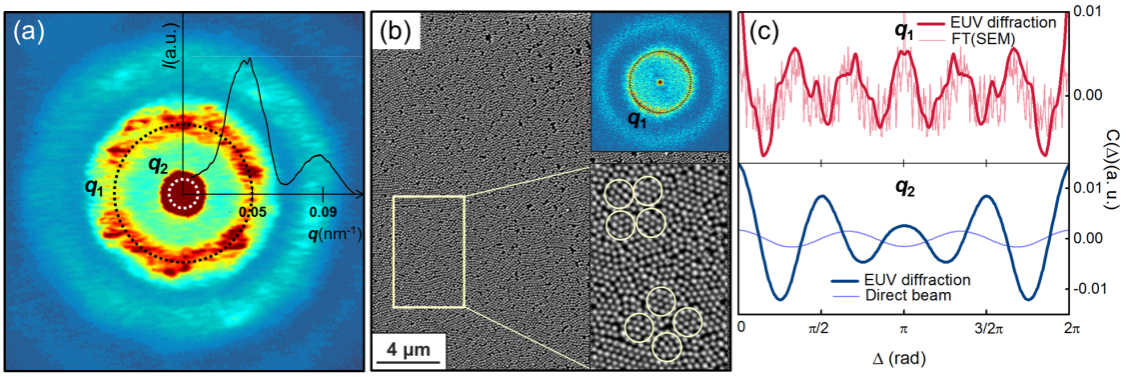

Figure 6.5: Angular Cross-Correlation at Multiple Length Scales. (a) Extreme ultraviolet diffraction pattern from the monolayer region of the colloidal crystal. This region is characterized by close-packed silica spheres in micron scale grains. (b) SEM image of corresponding region of the colloidal crystal. Top insert: Fourier transform of this image showing similarity to the diffraction pattern. Bottom insert: zoomed in region of the SEM image highlighting the crystal grains and the four fold symmetry between the grains. (c) Angular cross-correlation for the inter-sphere spacing (top) and for the inter-grain spacing (bottom). The six fold symmetry present in both the diffraction pattern's cross-correlation and the SEM image's cross-correlation indicate that the spheres are densely packed in a hexagonal geometry. The four-fold symmetry in the inter-grain angular cross-correlation indicates that the grains have a rectangular packing.

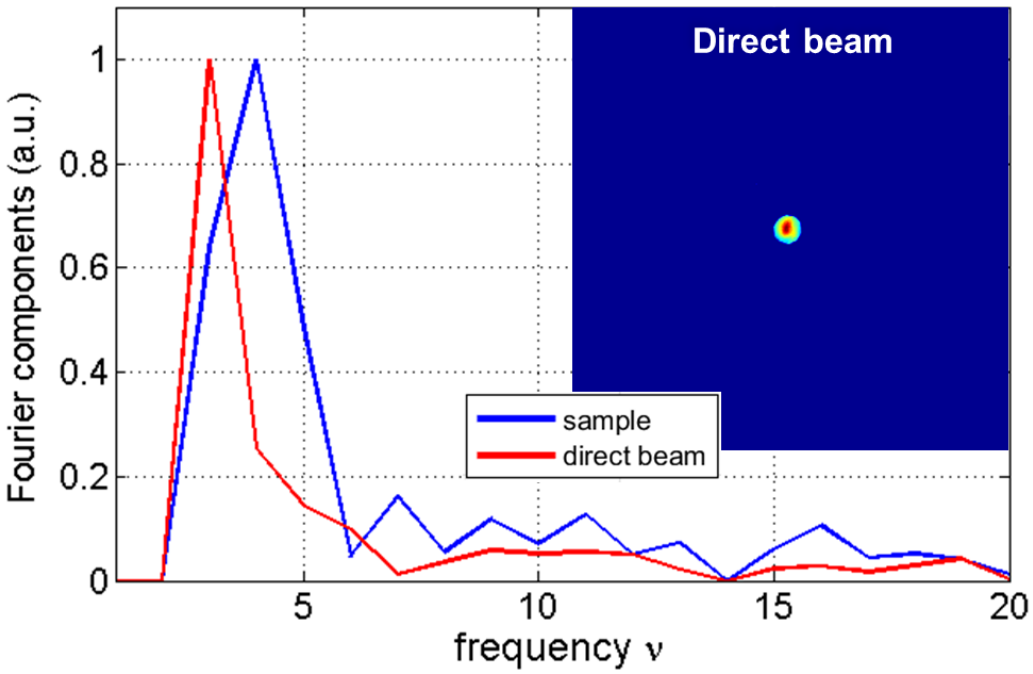

Figure 6.6: Diffraction from Direct Extreme Ultraviolet Beam. The insert shows the diffraction resulting from the EUV beam impinging directly onto the sensor without interacting with the sample. The main plot shows the radial intensity of the diffraction pattern compared to a diffraction pattern with sample interaction. From this, it can be seen that there are small angle features resulting from the interaction with the sample.

[259]. The probe relaxation factor was set to 3; the object relaxation factor to 1. The object was re-initialized thrice: on the 50th, 350th, and 1350th iteration.

The ptychographic reconstructions are shown in figure 6.7. There are horizontal striations across the image, this is due to insufficient overlap in the vertical direction due to the oblong nature of the probe (shown in figure 6.8). In the regions with sufficient overlap, the images are in agreement with the SEM images (Figure 6.9). The sphere separation measured in the reconstructions is 125 nm, in agreement with the SEM image and the cross-correlation analysis. The numerical aperture of the diffraction patterns is 0.37, corresponding to an Abbe limited resolution of 18.2 nm.

Comparing the center of one of the silica spheres and a region between spheres, a phase difference of 0.16 rad is measured. This phase difference corresponds to propagation of 124 nm through silica. This further indicates that the sphere diameter is in agreement with the other measurements. In order to properly consider only the phase accumulated through propagation through the sphere, the effects of the silica to silicon nitride interface needed to be accounted for. The Fresnel phase from each of these interfaces was calculated to be 5.6 μrad, which is negligible compared to the phase from propagation through the sphere [93].

The amplitude reconstruction in figure 6.7 is a quantitative measure of the spatially varying transmissivity of the colloidal crystal. The measured ratio between a high and low transmission region of the sample is 0.54, which is in agreement with the transmission through 124 nm of silica [93]. The entire range of transmission values is from 0.2 to 0.6. This range corresponds to transmission through 30 nm of silicon nitride followed by transmission through 248 nm and 124 nm of silica, respectively. From this, it is concluded that in every part of the image, the light has propagated through at least part of a silica sphere. This demonstrates that this region is indeed a multi-layer.

In principle, it is possible to look at an image of the transmissivity of a close packed colloidal crystal to extract three-dimensional structure. The transmission for three layers of hexagonal close-packed and face-centered cubic packing are shown in figure 6.10. The

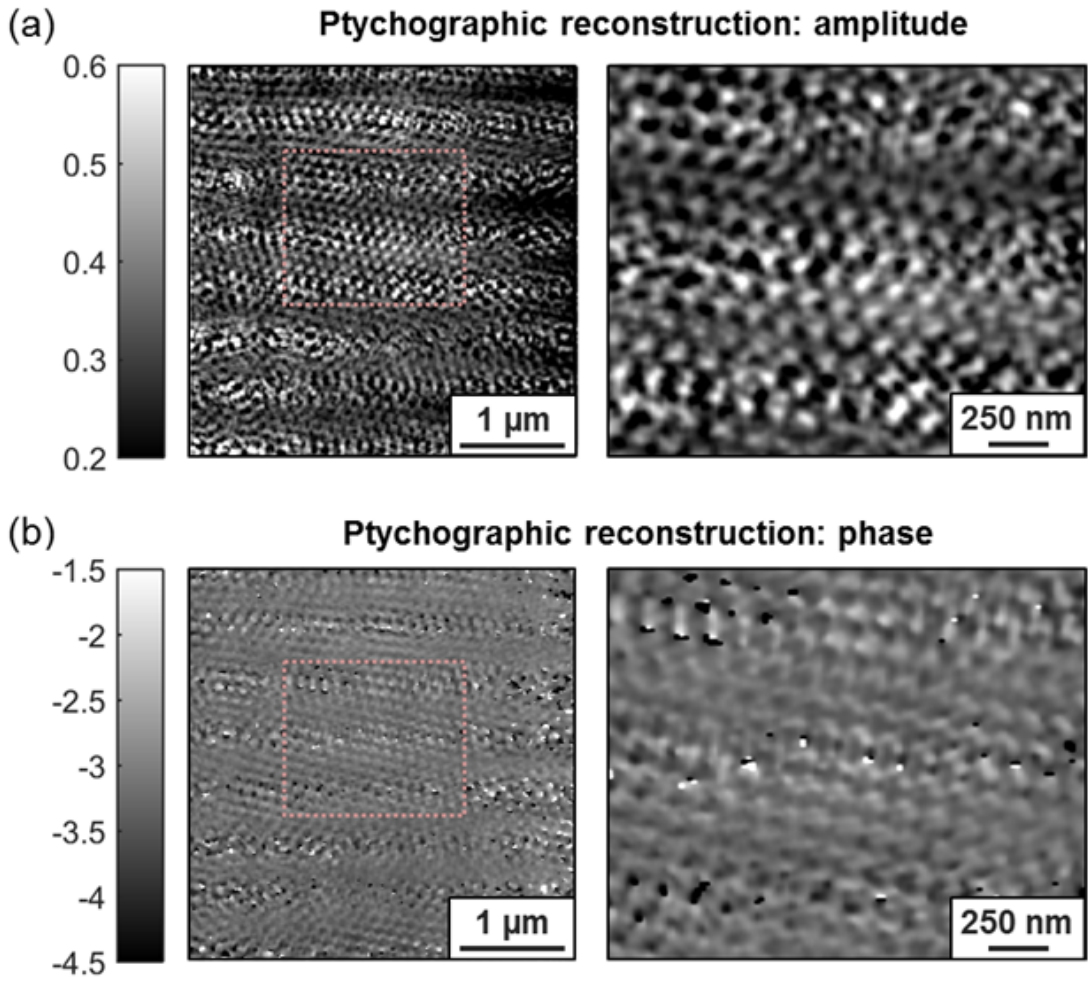

Figure 6.7: Extreme Ultraviolet Images of Colloidal Crystal. (a) Amplitude reconstruction of the colloidal crystal. (b) Phase reconstruction from the ptychographic imaging. The right panels show zoomed in regions of the left panels. The six-fold symmetry of the close packed silica spheres is readily apparent in the images. There are horizontal artifacts that are the result of insufficient overlap in the vertical direction.

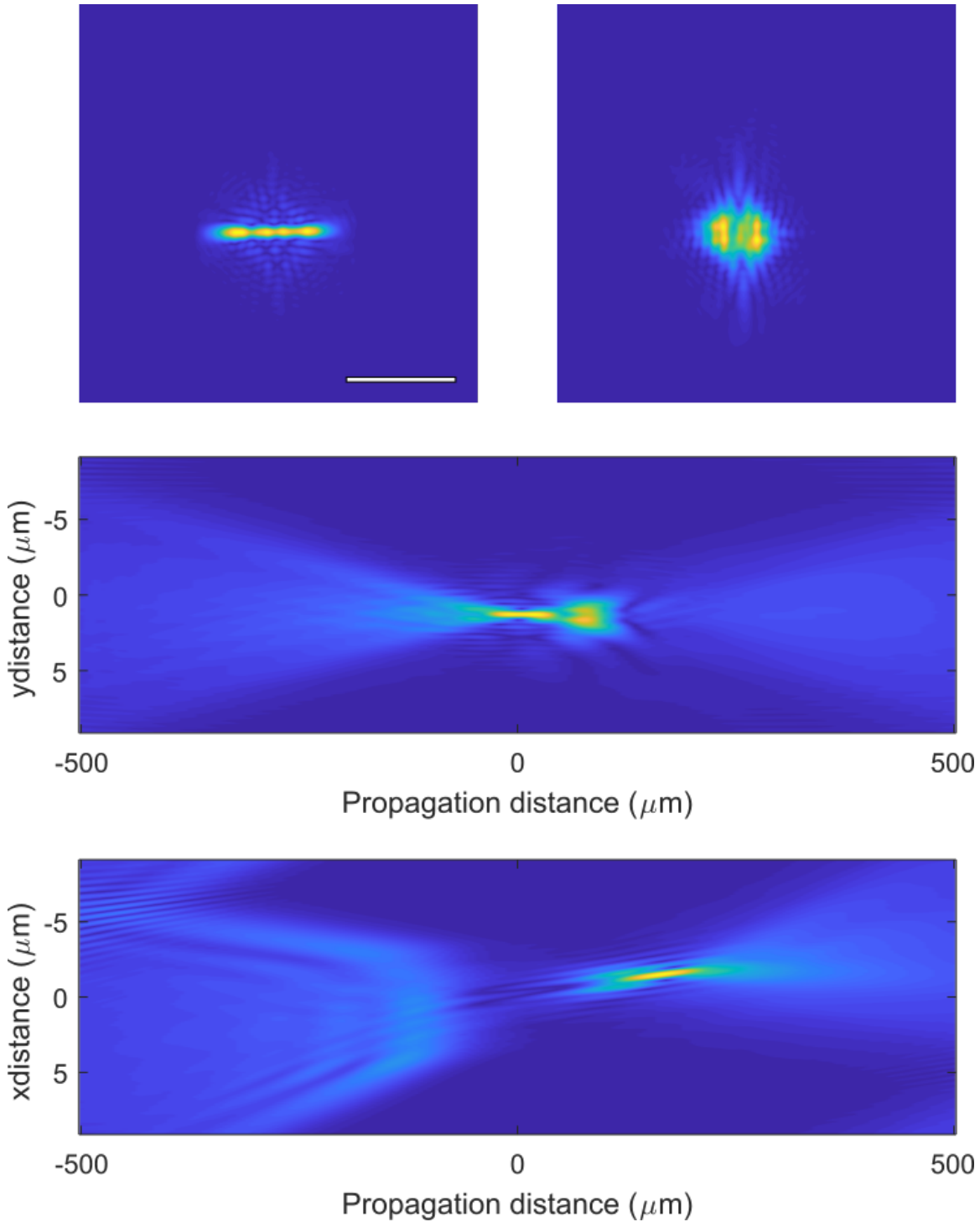

Figure 6.8: Extreme Ultraviolet Probe Reconstruction. Top left: reconstructed probe at the plane of the sample. Scale bar is 5 μm. Top right: reconstructed beam propagated to center of horizontal and vertical foci. Center and bottom: transverse slices through propagated beam showing the location and behavior of the beam near the focus. There is astigmatism present in the beam due to the non-zero incident angle on the curved focusing mirror.

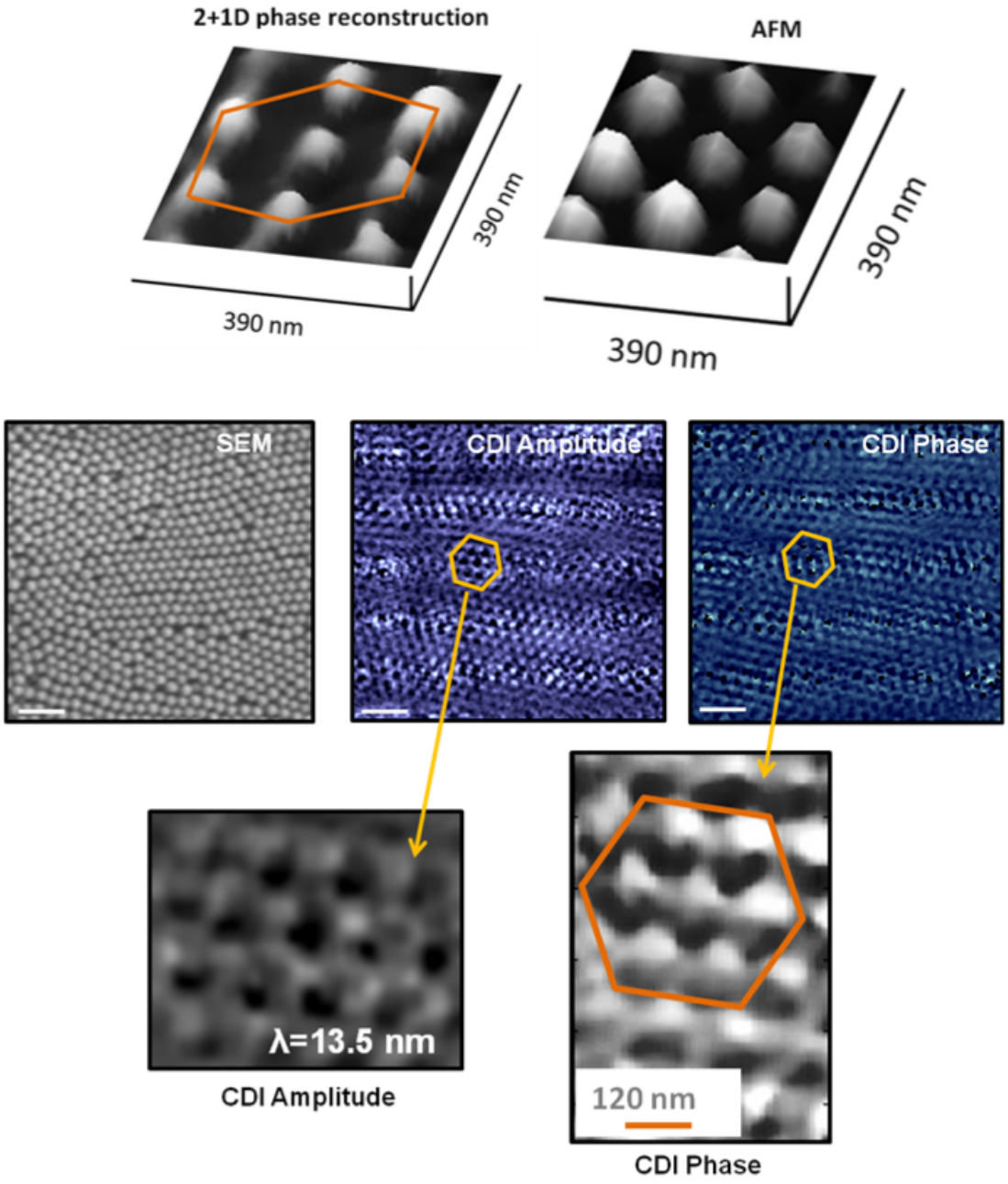

Figure 6.9: Comparison of AFM, SEM and EUV Ptychography Images. The sphere size and separation in the SEM and coherent diffractive imaging images are consistent. The bottom row compares the phase reconstruction of the colloidal crystals with an atomic force microscopy (AFM) image of the sample. The thickness of the spheres is in agreement as is the separation and overall structure.

two are immediately distinguishable in theory. In the case of the colloidal crystal sample, a definitive packing cannot be assigned, likely due to the random assortment of hexagonal close-packed and face-centered cubic packings across the sample.

This combination of small angle Bragg scattering and angular cross-correlation analysis with tabletop extreme ultraviolet ptychography imaging enables new avenues for studying materials on the nano-scale and at larger scales simultaneously.

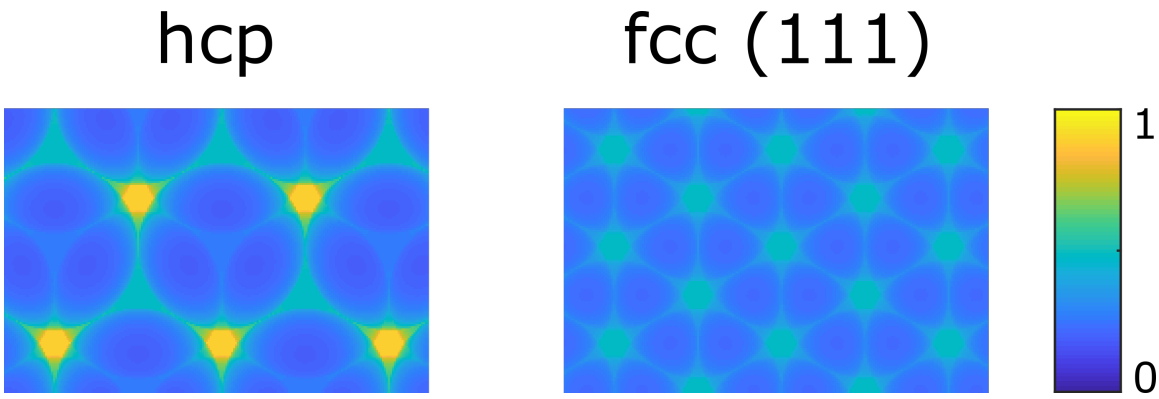

Figure 6.10: Comparison of HCP and FCC Lattice Projections. Projections for a hexagonal close-packed (hcp) and face-centered cubic (fcc) stacking of spheres are displayed. Due to the different alignments of the third layer, some regions of the sample will be highly transmissive in the hcp arrangement, while every location in the fcc projection passes through some part of the spheres. The reconstructed images of the colloidal crystal can be compared to these projections to understand how the sample is ordered in its axial dimension.

Chapter 7

Time-Resolved Microscopy of Acoustic Dynamics

7.1 Introduction

As new innovation and discovery leads to the design of more exotic materials, the need for techniques to investigate their properties increases. Specifically in the nano-scale regime (<100 nm), the physical models that describe material properties such as heat, charge, and spin transport break down [7, 97, 216, 243]. The lack of a fundamental understanding of the underlying physics at this scale creates difficulties in the design of functional nano-systems. To address this challenge, new techniques that can access high spatial and temporal resolution are critically needed. This will enable a stronger understanding of fundamental nano-scale behavior [113, 166, 260].

Time-resolved imaging on the ultrafast scale has been advancing dramatically. Ultrafast electron imaging now enables direct visualization of out-of-equilibrium intermediate states in systems undergoing phase transitions and deformation on the femtosecond timescale [17, 26]. Facility scale ultrafast x-ray free electron laser sources now employ coherent diffractive imaging techniques [162], which has enabled visualization of acoustic phonons in a single nano-crystal [39, 40] and of dislocation dynamics in battery nano-particles [239].

High harmonic generation (HHG) sources provide ultrafast, extreme ultraviolet beams that do not experience timing jitter between their driving light source to sub-femtosecond precision. The exquisite temporal properties of HHG light has been used to study a myriad of physical systems, shedding light on previously unknown dynamics [35, 97, 228, 230]. Most of

the methods that have employed HHG sources have done so in a spatially averaged manner, probing either periodic nano-structures or uniform materials. This necessarily blinds the technique to any spatially varying dynamics and prevents measurements on materials that have spatially varying structure. This is especially important in materials where the structure impacts the overall material properties, such as the case of metamaterials [260].

In this chapter, the development of a spatially and temporally resolved microscope is presented. This microscope uses extreme ultraviolet light from an HHG source to stroboscopically image dynamics with sub-100 nm transverse resolution, sub-nanometer axial precision, and ≈10 fs temporal resolution. This system is used to measure the dispersion relation of surface acoustic waves in silicon and to directly image the propagation of acoustic waves in an isolated nano-antenna. We reported on these experiments in [111].

7.2 Experimental Design

The microscope uses ptychography coherent diffractive imaging [141, 143, 233, 234] in which the sample is scanned with a diffraction pattern collected at each scan position and an image is reconstructed from this dataset. The extreme ultraviolet beam used for this is generated from an infrared 23 fs, 1.5 mJ, 5 kHz Ti:Sapphire laser [KMLabs Griffin and KMLabs Dragon] as shown in figure 7.1. The infrared light is focused into a glass waveguide that is filled with 44.5 torr of argon. Most of the driving infrared light is then separated from the extreme ultraviolet light through a pair of super-polished silicon mirrors set near Brewster's angle for infrared. The residual infrared light is blocked by a 100 nm aluminum filter [NTT]. From there, the microscope itself is constructed (Figure 7.2). A single wavelength (28.9 nm) of the extreme ultraviolet beam is selected using a pair of narrow-bandwidth multi-layer mirrors at 45 degrees. This beam is focused onto the sample using a 5 degree angle of incidence, off-axis ellipsoidal mirror, yielding a spot size of 7 μm full width at half maximum. This beam is incident at 60 degrees from the normal of the sample plane. The diffraction from the sample is collected on an in-vacuum charge-coupled

device (CCD) sensor [PI-MTE] which is placed 36.5 mm from the sample plane. In this configuration, the Abbe limited resolution is 38.1 nm.

In order to induce dynamics that are synchronized with the extreme ultraviolet light source, the same infrared source that drives the HHG process is used to excite dynamics in the sample. A beamsplitter is placed in the beam path prior to the HHG setup. The additional beam, the pump beam, is routed through a delay stage [Aerotech] to control the timing between the two arms. This infrared pump beam is focused onto the sample at near-normal incidence, with a beam size of 650 μm full width at half maximum. The intensity of the pump beam is 100 mW, yielding a total fluence of 8.4 mJ/cm^2.

The stability of the extreme ultraviolet source was tested by reflecting the beam off of a gold mirror and measuring the beam on the detector every 1.5 sec for one hour (see figure 7.3). Over this time, the standard deviation of the beam's centroid was 1.9% and 0.11% of the beam diameter in the vertical and horizontal directions, respectively. Since each ptychography scan takes twenty minutes to acquire, this level of stability is deemed sufficient.

The pump arm of the time resolved microscope was tested to ensure that the shape and location of the pump beam did not appreciably change over the length of the delay stage. The beam was recorded on a pixelated detector for a delay value at each end of the stage's range. Over this range, the beam size ranged from 449 by 316 μm to 451 by 310 μm, which is a change by less than 2%. Over this range, the beam changed location by 27 μm in the horizontal and 61 μm in the vertical. This drift is small enough that the probed region of the sample is pumped regardless of where the delay stage is set.

The pump and probe beams were roughly aligned by spatially overlapping the two infrared beams on a nonlinear beta barium borate (BBO) crystal. The two beams were incident at different angles so that, when the two are overlapped temporally, a mixing second harmonic signal can be observed spatially separated from the two beams. The delay stage in the pump arm of the setup is translated until this mixing signal is maximized. This is the

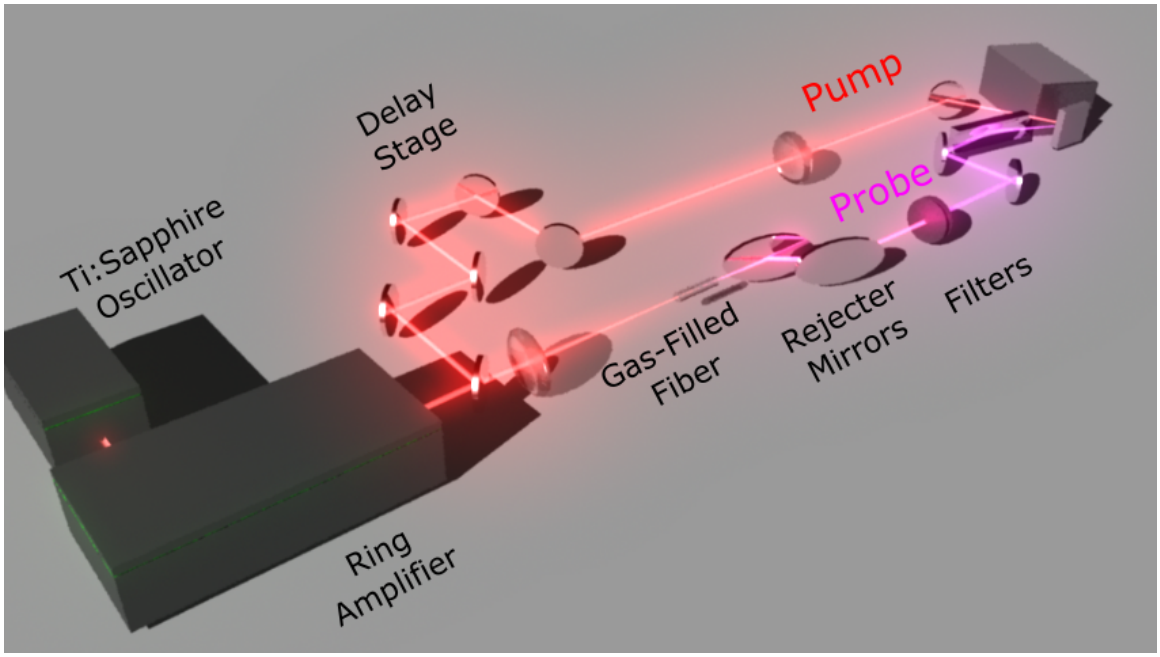

Figure 7.1: Pump-Probe Microscope Design. An ultrafast Ti:Sapphire laser is focused into an argon-filled hollow capillary to generate extreme ultraviolet light. The driving infrared is removed from this beam using a pair of silicon mirrors near Brewster's angle and a pair of thin Al filters. This light then enters the ptychography microscope. Meanwhile, some of the driving infrared light is split from the initial beam, passes through a variable delay stage, and is then focused onto the sample. Varying the delay in this line changes the pump-probe timing, thus allowing time-resolved measurements.

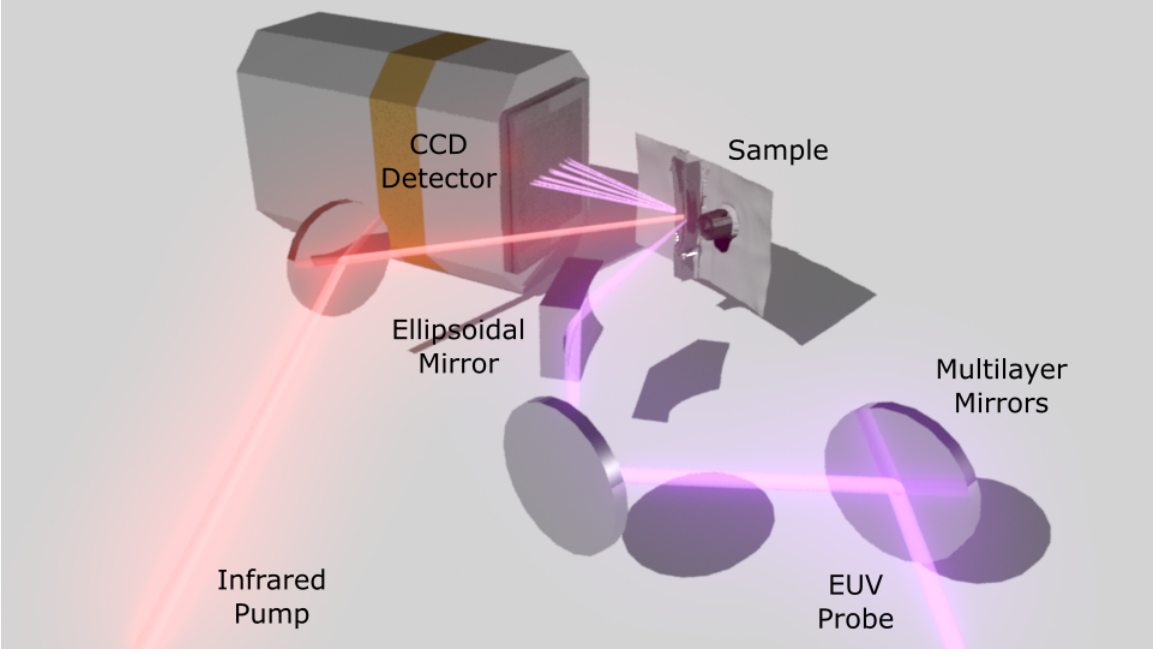

Figure 7.2: Schematic for Ultrafast Microscope. Dynamics are induced in the sample with an ultrafast infrared pump beam. The dynamics are then probed with the extreme ultraviolet beam. This beam is incident on two multi-layer mirrors and then focused onto the sample via an off-axis ellipsoidal mirror. The diffraction is measured on a CCD detector. The timing between the infrared and extreme ultraviolet beams is changed for the next measurement, allowing for time resolved imaging.

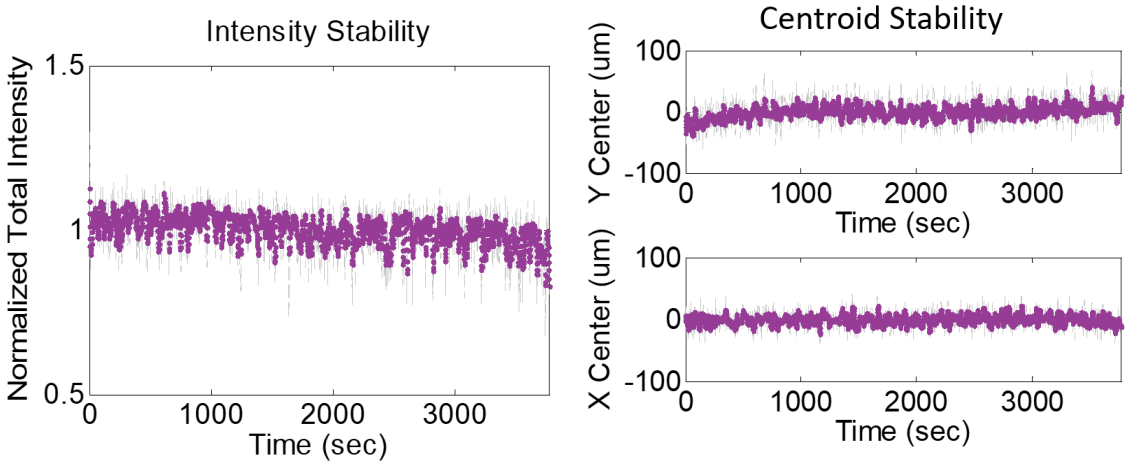

Figure 7.3: Stability of EUV Source. Left: stability of the EUV intensity plotted over the course of an hour. Over this time there is a 5% drift in the average value, with a standard deviation of 6.5% of the mean intensity. Right: centroid of the beam in the vertical (top) and horizontal (bottom) direction. Over the course of the hour, the vertical centroid drifted by 13 μm and the horizontal by 1.1 μm, both corresponding to less than 2% of the beam diameter. This level of stability is deemed sufficient for a ptychography data set to be recorded without concern for drift in the illumination.

delay that causes the two beams to be incident at the same time. This time is referred to as 'time zero'. Less delay in the pump arm and the pump will arrive before the probe, allowing ultrafast dynamics to be measured. More delay in the pump arm and the pump will arrive after the probe, so no ultrafast dynamics are observed, as they have not yet occurred.

In order to prevent the infrared pump light from being measured by the detector, a 195 nm thick aluminum filter [Luxel] is placed directly in front of the camera sensor. The efficacy of this filter in obscuring the pump light from the detector is measured as a function of pump intensity. The results of this measurement are available in figure 7.4. The total light on the detector is measured in the case of no pump light entering the experimental chamber. The total intensity on the camera is calculated and used as the normalization factor for the subsequent measurements. These subsequent measurements are taken at various pump intensities up to 500 mW. Over this range, the increase in signal on the detector is less than 1% of the natural background of the detector. In the actual experiments, the pump intensity is strictly less than 200 mW, where the infrared leak-through is negligible.

7.3 Time-Resolved Measurements of Periodic Gratings

Previous work has measured the acoustic dynamics of surface acoustic waves launched in silicon [215]. In order to validate the time-resolved measurements made by this microscope, a similar measurement is made. A 10 nm tall nickel grating with 500 nm thick lines with a 2 μm period are patterned onto a silicon substrate. This grating is presented in figure 7.5.

This diffraction grating, through its initial thermal expansion, launches longitudinal and surface acoustic waves into the substrate. As these waves propagate, they distort the surface under the grating, altering the diffraction pattern. Diffraction from this grating is measured on the detector as the pump-probe delay is scanned from slightly before time zero to 650 ps after in 5 ps steps. For each time delay, one diffraction pattern is recorded with the pump light incident on the sample, and one is recorded without the pump light. For each diffraction order, the diffraction efficiency at each time delay is calculated and compared to

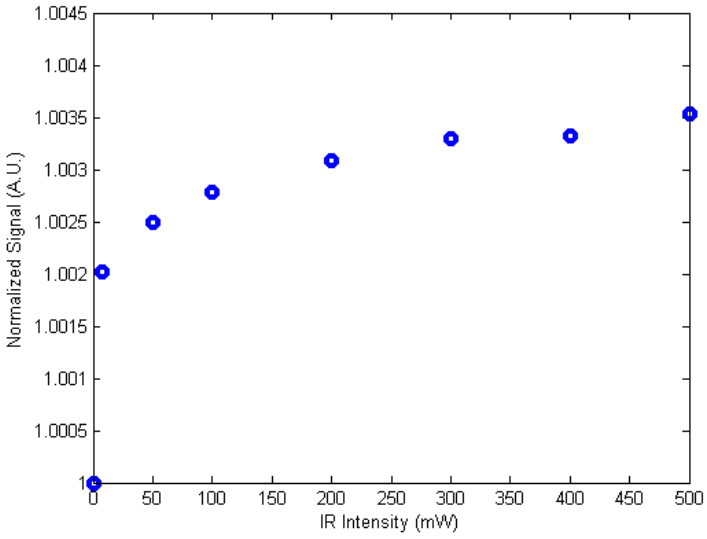

Figure 7.4: Effectiveness of Aluminum Filter on Stray Pump Light. The background signal on the detector is measured as a function of pump intensity. All of the measurements are normalized to the total intensity when the pump is set to 0 mW. The effect from the pump light, even at 500 mW power, represents less than 1% of the background noise, and thus can be safely ignored.

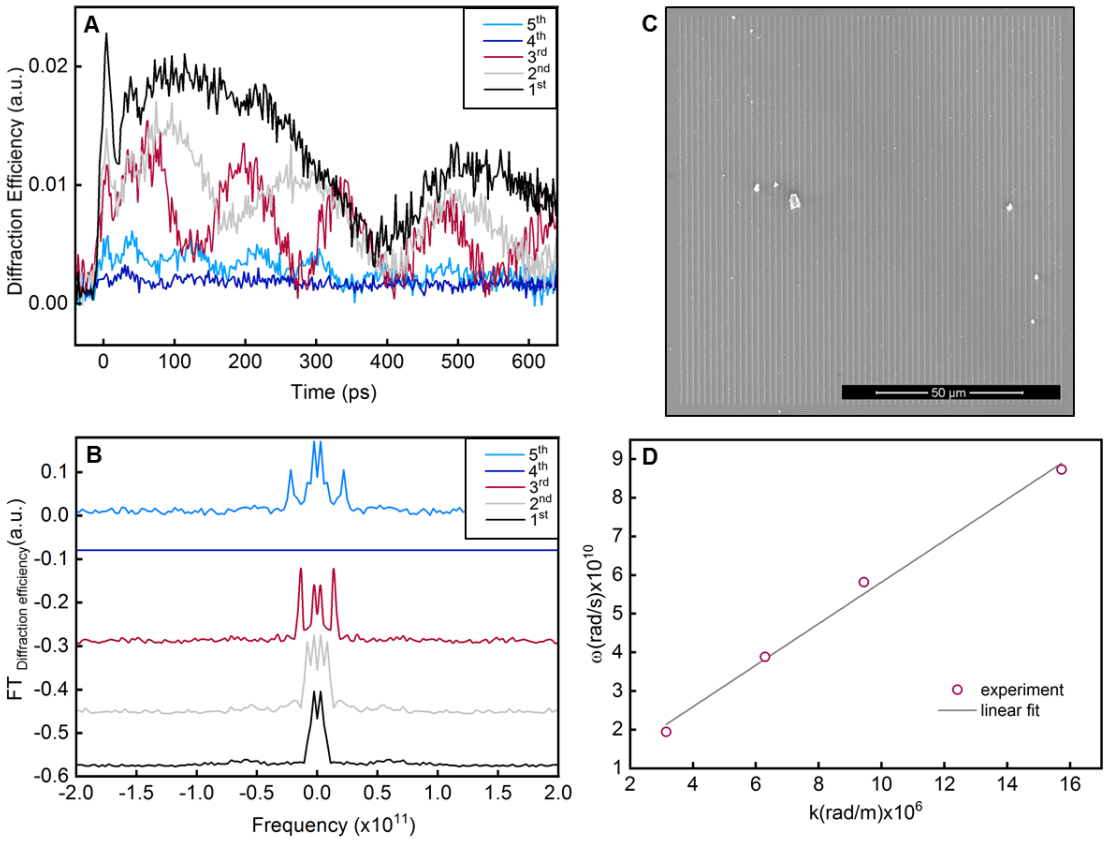

Figure 7.5: Dispersion Relation of Silicon Surface Acoustic Waves. A) Transient diffraction efficiency measured as a function of pump-probe delay for the first five diffracted orders. B) Fourier transform of the traces in A. C) Scanning electron microscope image of the nickel grating used for these measurements. D) Dispersion relation for the measured acoustic waves from the diffraction patterns. The transient signal measured in each diffraction order is at a higher frequency than the previous. This can be seen immediately in the Fourier transforms in B. These increasing frequencies as a function of spatial frequency are shown in D, and adhere to a linear dispersion relation. The velocity associated with this linear relation is 5230 ± 650 m/s, which agrees with the acoustic wave velocity in silicon.

the corresponding pump-off value. The diffraction efficiency is given by

$$\mathcal{E} = \frac{AC - DC}{AC + DC} \tag{7.1}$$

where AC is the total intensity in the diffracted order, and DC is the total intensity in the undiffracted order. This normalized diffraction efficiency is plotted as a function of delay time in figure 7.5. The first diffracted order shows an initial increase in diffraction efficiency followed by a high frequency oscillation that gives way to a lower frequency (with a period of ≈400 ps). The higher diffracted orders show a similar functional form, but with a higher frequency in that final oscillation. This frequency is apparent when a Fourier transform is performed on the transient signal. From this Fourier transform, the temporal frequency of the oscillation is calculated as a function of spatial frequency, which is shown as a dispersion relation in figure 7.5. Over the range measured in this experiment, the dispersion relation is linear, yielding a velocity of 5230 ± 650 m/s. This velocity is in agreement with the velocity of a pseudo-surface acoustic wave [168] in silicon.

The dynamics present in the time-resolved measurements are verified to be ultrafast dynamics instead of noise or irreversible dynamics. One transient measurement was recorded by scanning the delay stage from negative time delays to positive time delays. A second measurement was recorded scanning the delay stage in the opposite direction, positive to negative. These traces are in figure 7.6, and they show the same dynamics as a function of pump-probe delay. This indicates that the dynamics are indeed caused by the pump light.

The same grating is imaged using a ptychographic scan with 197 scan positions in a Fermat spiral pattern [104] with 2 μm spacing between adjacent positions. Each of these scans is reconstructed using 1000 iterations of the ePIE [143] algorithm with modulus enforced probe [74]. Following this, the representative probe from the ten reconstructions was selected and 100 iterations of ePIE without any update to the probe or the positions were run. This ensures that all of the images are naturally registered as the probe position is the same for all of the scans. The reconstructions of the nickel grating for each of these time

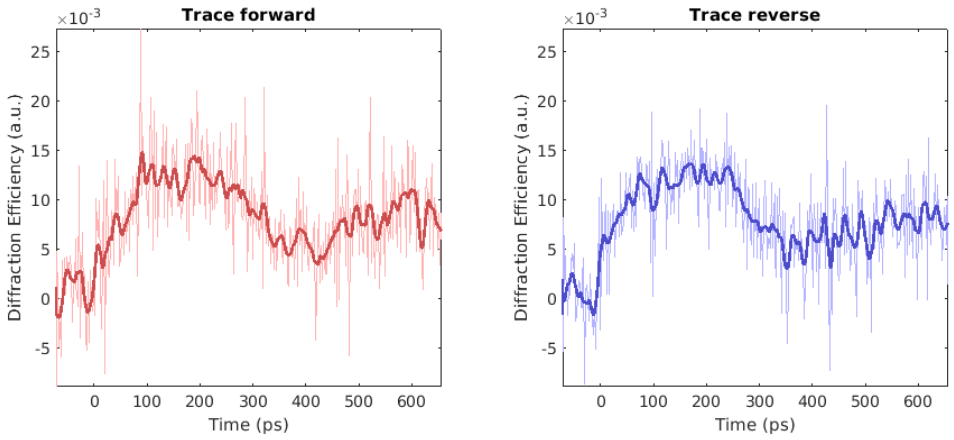

Figure 7.6: Verification of Ultrafast Dynamics. The left figure shows the dynamics measured when scanning delays from negative to positive delays. The right trace shows the same measurement made in the reverse order. Both of these measurements show the same dynamics as a function of pump-probe delay, but not as a function of acquisition time. This indicates that the dynamics are induced by the pump.

delays are the subject of figure 7.7. The images displayed in figure 7.7 are phase images of the nickel grating at various pump-probe time delays, indicated in the figure in units of picoseconds. The images themselves look mostly identical by eye, thus more detailed analysis is used to probe the differences between them.

In order to analyze the dynamics present in the reconstructions, the images were summed in the horizontal direction, giving a one-dimensional average of the grating. A Fourier transform was performed on this one-dimensional grating. The diffraction efficiency of this Fourier transform was measured by calculating equation 7.1. The diffraction efficiency for each image is plotted as a function of pump-probe delay in figure 7.8. Also plotted is the diffraction efficiency calculated from the average experimental diffraction pattern from the ptychographic data set. Comparing the two plots, it can be readily observed that the two show the same functional form, indicating that the dynamics captured in the diffraction pattern are accurately represented in the phase reconstructions.

7.4 Time-Resolved Measurements of Isolated Structures

In this section, the acoustic dynamics of isolated nano-structures are measured using the same time-resolved, extreme ultraviolet (EUV) microscope. Unlike the previous case of the periodic structures, the acoustic waves launched in these isolated structures are not launched as a single, well defined frequency, but are instead characterized by shorter wavelength waves propagating inside of the structure itself. Despite the differences in the samples, the same techniques can be employed to study them.

7.4.1 Dispersion in a Uniform Nano-Antenna

The first isolated sample investigated is a uniform nano-antenna made of nickel deposited on a silicon substrate. This antenna is displayed, multiplied by the extreme ultraviolet probe, in figure 7.9. The diffraction from this antenna shows multiple, separated diffraction peaks, allowing for the calculation of the dispersion relation.

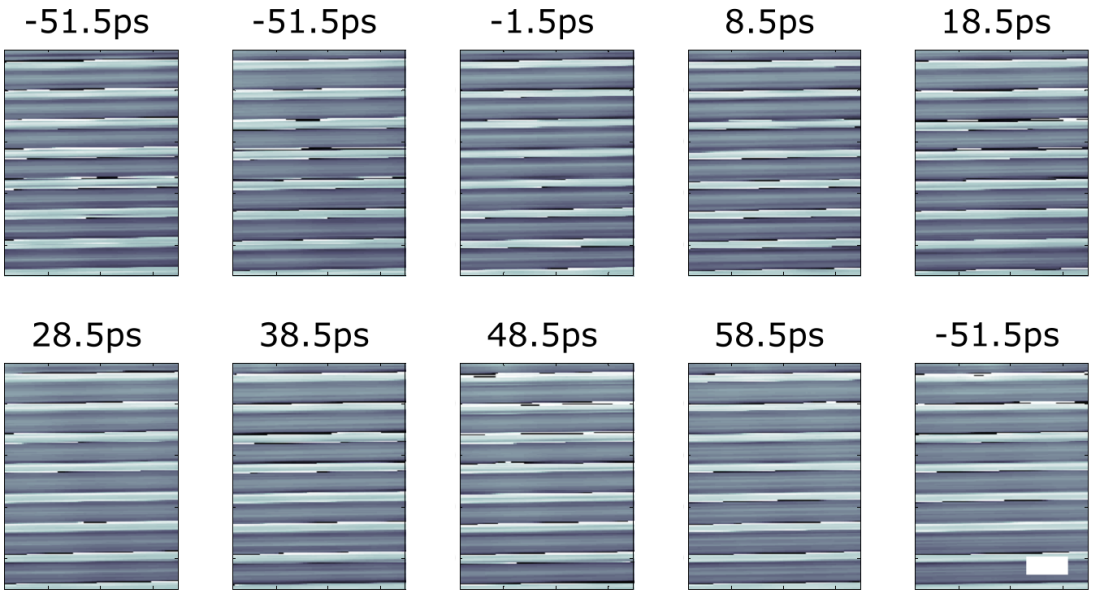

Figure 7.7: Time-Resolved Images of a Periodic Grating. Ten phase images from various pump-probe delay times are presented. The title of each image represents the delay time relative to time zero in picoseconds. The scale bar is common to all of the images and is 2 μm in both dimensions. To the eye, the reconstructed images look mostly identical, however, subtle differences can be observed through further analysis.

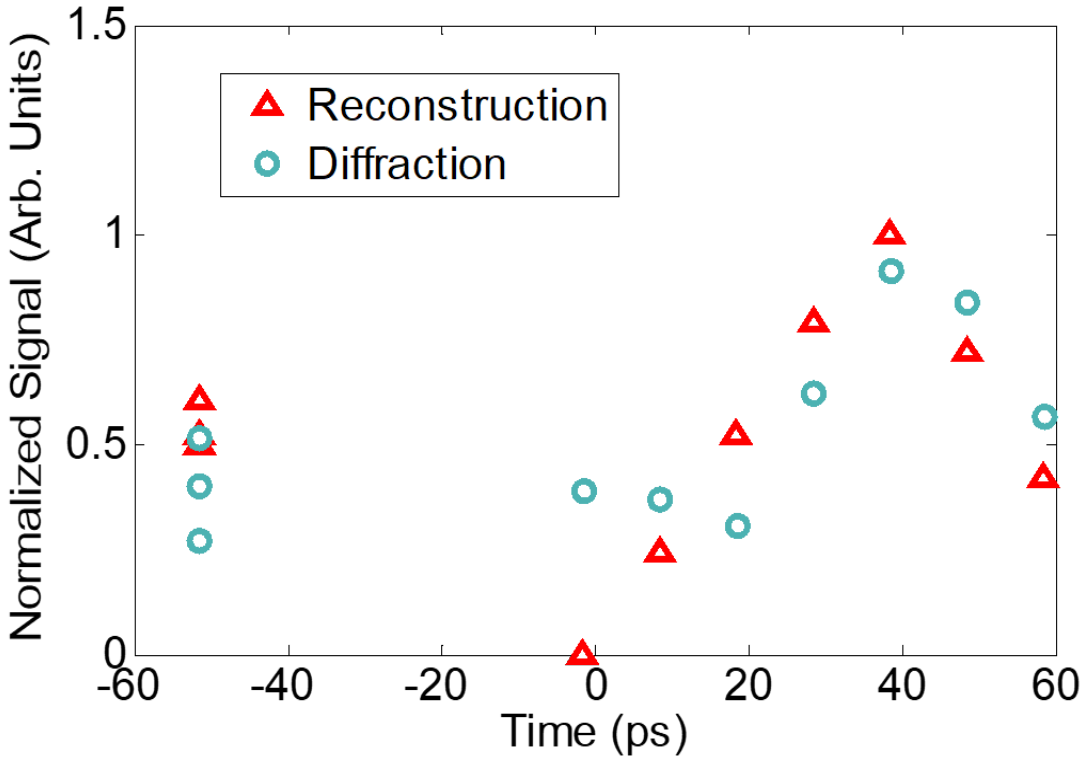

Figure 7.8: Transient Dynamics from Ptychographic Reconstruction. The cyan circles are the diffraction efficiency into the first diffracted order from the average diffraction pattern recorded in the ptychographic scan. The red triangles are the diffraction efficiency of the Fourier transform of the reconstructed phase of the grating. The two datasets show the same dynamics that are representative of acoustic wave excitation in the underlying silicon substrate.

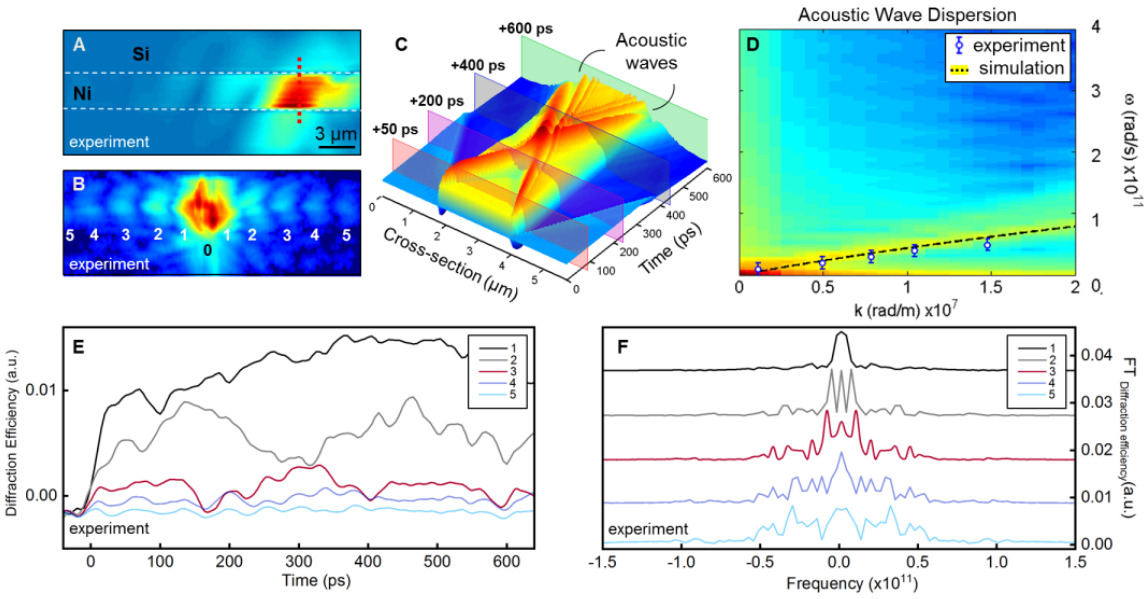

Figure 7.9: Acoustic Dynamics in Uniform Nano-Antenna. A) Reconstructed amplitude image of the uniform nano-antenna, multiplied by the reconstructed probe. The red line indicates the cross-section used for the simulation. B) Experimental diffraction pattern from this antenna. C) Simulated dynamics in the antenna's cross-section. The acoustic waves can be observed propagating through the antenna. D) Simulated and measured dispersion relation of the acoustic waves. The simulation is the background image and the dashed black line. The experimental data points are the blue circles. E) Experimental diffraction efficiency as a function of pump-probe delay for the first five diffraction orders. F) Fourier transform of the diffraction efficiency for each of the traces in E. The temporal frequency of the diffraction efficiency oscillations increases as a function of spatial frequency, permitting the dispersion relation to be measured.

The diffraction from the uniform antenna is measured as a function of pump-probe delay in 5 ps increments. For each diffracted order, the total intensity into that order was calculated and compared to the intensity in the undiffracted order according to equation 7.1. This quantity experiences an explosive increase just after time zero followed by oscillatory behavior. The temporal frequencies of the oscillations are calculated by extracting the most prominent peak from the Fourier transform of the diffraction efficiency after time zero. The spatial frequency of each peak is determined by calculating the centroid of each diffraction peak. The frequency of the temporal oscillation increases with increasing spatial frequency.

From the dispersion relation measured on the uniform nano-antenna, the velocity of the underlying acoustic wave is calculated to be 2790 ± 240 m/s, a velocity in between the Rayleigh velocity of nickel and that of silicon.

In order to verify this dispersion relation, numerical simulations of the acoustic dynamics of a cross-section of the nickel antenna are performed [42, 95, 169]. A 2.2 μm wide cross-section of the antenna is simulated in two dimensions, ignoring any dynamics along the long axis of the antenna. The results of this simulation are shown in figure 7.9. The edges of the antenna expand in such a way as to launch acoustic waves that travel both away from the antenna through the substrate and into the antenna through the nickel. Taking a Fourier transform of the vertical surface deformation in both space and time yields a simulated dispersion relation [183]. The dispersion relation is also simulated using a finite-element modal analysis on the antenna's cross-section. From this modal analysis, it can be seen that the surface acoustic waves propagating across the nano-antenna are coupled into generalized Lamb waves, a dispersive waveguide mode wherein the antenna acts as an acoustic waveguide [9]. Since these modes are partially confined in the nickel and otherwise propagating in the silicon, the theoretical velocity is between the Rayleigh velocities of nickel and silicon. Both this dispersion relation and that from analyzing the simulated dynamics are the same, and they are in agreement with the experimentally measured relation.

7.4.2 Imaging of Dynamics in a Tapered Nano-Antenna

Acoustic dynamics in a sample that thwarts direct simulation are now considered. A tapered nano-antenna is fabricated by depositing nickel on silicon. This antenna is triangular in shape with a 5 μm wide base and a length of 53 μm. The entire volume of the antenna is 1000 μm^3 with a large aspect ratio (1:2500). Because of this, direct finite element simulations of the structure's dynamics are unfeasible. Instead, direct measurements of the nano-antenna are taken, and then used to benchmark an approximate simulation.

The experimental measurements of the tapered nano-antenna are taken in a pump-probe ptychographic imaging modality. The sample is perturbed with the driving infrared beam, and probed with the extreme ultraviolet beam, with the resulting diffraction recorded (Figure 7.10). Diffraction patterns are measured in a redundant spatial scan to form the ptychographic dataset [141, 143, 233, 234]. The sample is scanned along a Fermat spiral pattern, as shown in figure 7.11. However, at each scan position, two diffraction patterns are recorded: one with the pump present, and one without. This is repeated for 14 different pump-probe delays. The ptychography scan was composed of 82 scan positions in a Fermat spiral pattern [104] with scan position separation of 2 μm. The diffraction patterns were recorded with 2×2 on-chip binning, averaged over 3 accumulations, with a 200 kHz readout rate and a 0.15 sec exposure time. Each ptychographic image is thus formed with 49.2 sec of exposure with $\approx 6\times10^9$ photons/sec incident on the sample. For each scan, 10 images of the direct beam reflected off of silicon were recorded to use the modulus enforced probe technique [74]. The final images were renormalized based on the reflectivity of silicon [93]. The result of this dataset is 28 images of the nano-antenna: 14 with the pump present that show ultrafast dynamics, and 14 without the pump to serve as reference images.

The diffraction patterns were centered relative to the peak of the average diffraction pattern. This has the effect of removing the non-physical linear phase that originates from a shift in the detector relative to the diffraction patterns. A constant background was re-

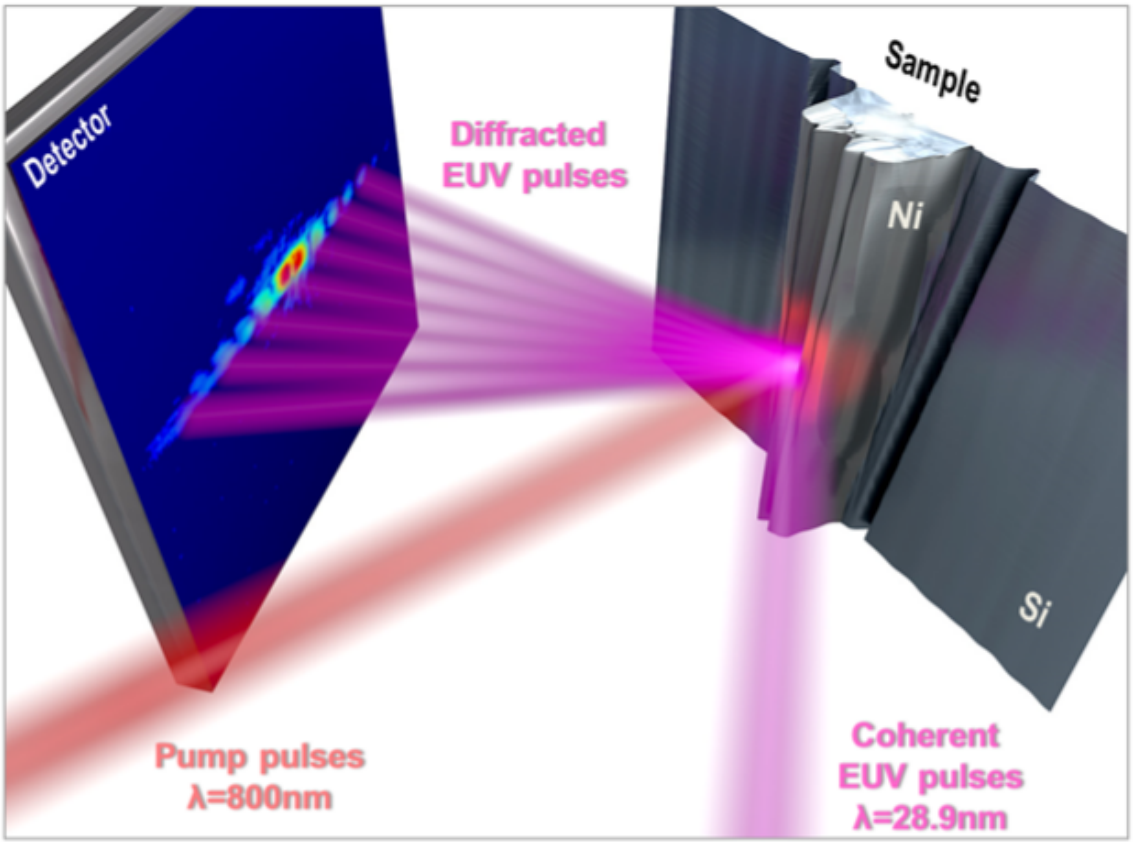

Figure 7.10: Experimental Design for Ultrafast Imaging of Tapered Nano-Antenna. Dynamics in the nickel nano-antenna are induced through heating from an ultrafast infrared pump beam. This results in deformations of the structure, which are measured using coherent, extreme ultraviolet light. The diffraction from the sample is recorded on a CCD detector and then used to form an image of the structure as a function of delay between the infrared and the extreme ultraviolet light.

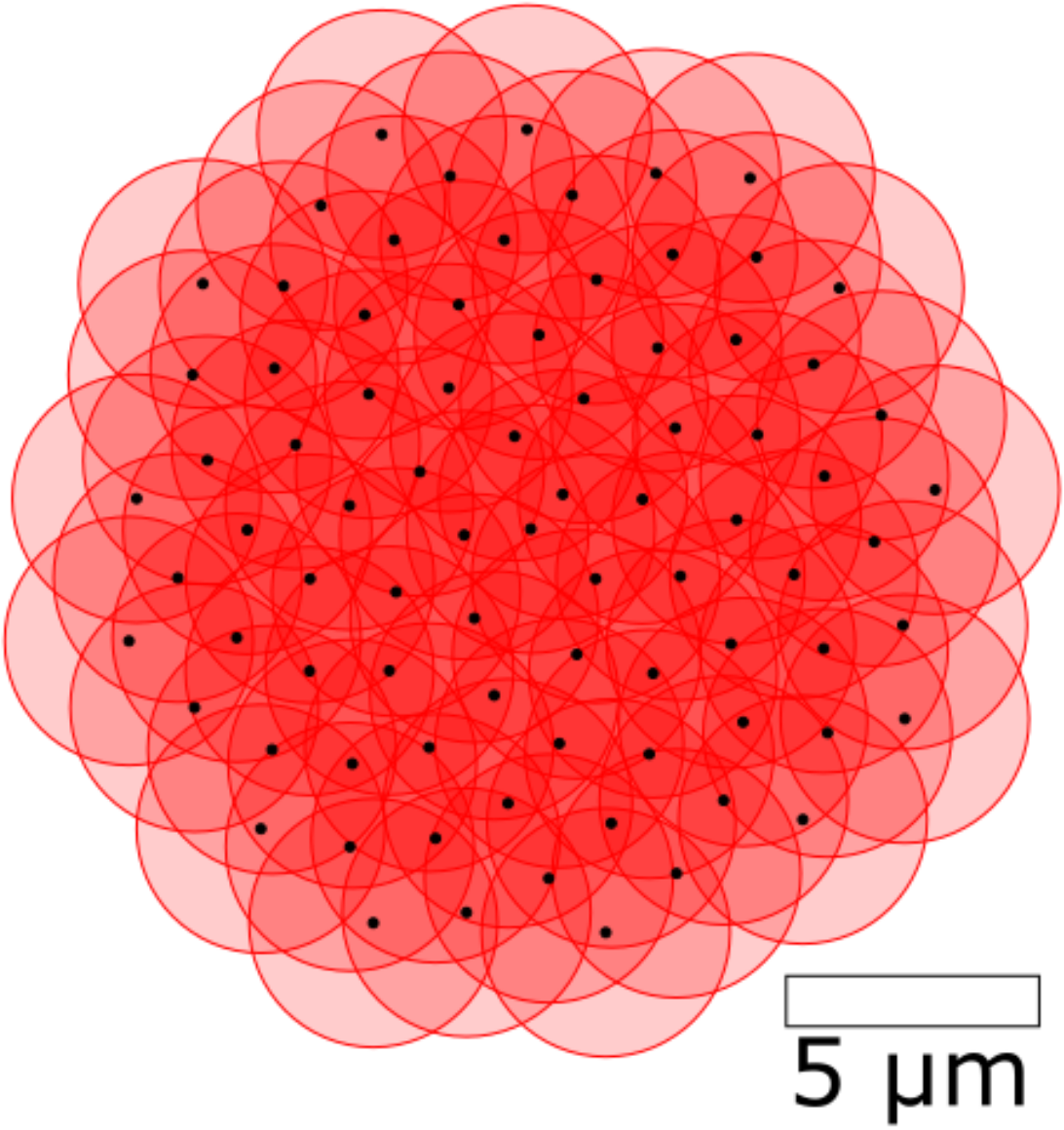

Figure 7.11: Fermat Spiral Ptychography Scan. The scan positions used in the ptychography scan of the tapered nano-antenna are displayed as black dots. The red circles show the idealized extent of the probe at each scan position. Because the scan grid is not periodic, no gridding artifacts arise, removing the need for random offsets to the scan positions.

moved from the diffraction patterns. The curvature of the diffraction that results from conical diffraction effect was computationally reversed using tilted plane correction techniques [75]. The diffraction patterns were cropped to be 512x512 pixels in size, corresponding to a theoretical Abbe resolution of 76 nm in both transverse dimensions [242].

The ptychographic reconstructions were run using 10550 iterations of the ePIE algorithm [143] with modulus enforced probe [74]. The object relaxation parameter was set to 1 and the probe relaxation factor was set to 5. 400 iterations of a position correction algorithm [259] were used to refine the scan positions.

The reconstructed probe is displayed in figure 7.12, and the reconstructed sample is shown in figure 7.13 along with correlated images from a scanning electron microscope and an atomic force microscope. These images show the fidelity of the extreme ultraviolet microscope to be quite robust. Furthermore, in these images, not only is the tapered nano-antenna depicted, but additionally a small circular object is present to the right of the antenna.

7.4.2.1 Image Segmentation Using Complex Histograms

In order to address the different elements of the images individually, the images need to be segmented into their various components. The technique developed to perform this segmentation, analysis by complex histograms, is herein described [111].

Each pixel in the reconstructed images contains a complex value for the reflectivity of the sample. Considering these values as a single list of values, a histogram can be created that tallies the frequency of each complex value's occurrence. In one dimension, a histogram of the amplitudes or the phases of all of the pixels could be crafted. In two dimensions, the full, complex value can be considered. In this mode, any pixels that have complex values within a small range in the Argand plane will be lumped together and tallied. The result of these tallies will be a two-dimensional histogram in which the locations are complex values and the intensity is the number of pixels in the image with a complex value in this range.

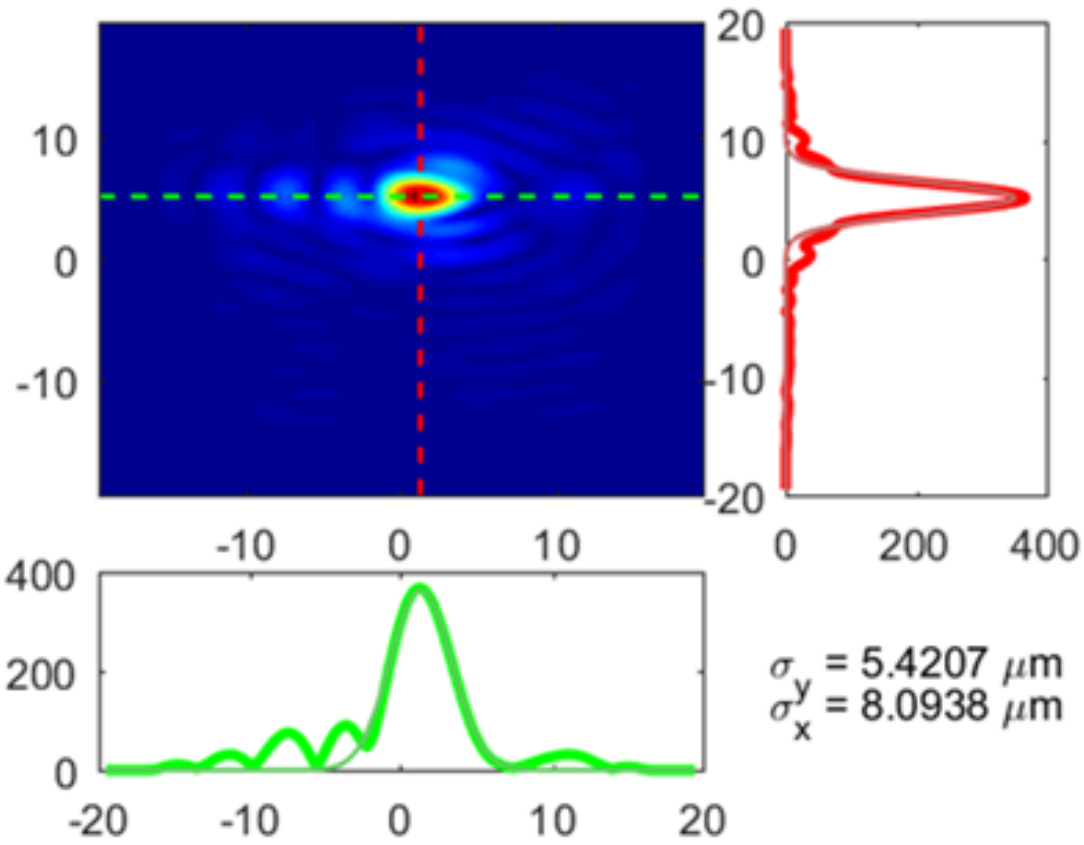

Figure 7.12: Reconstructed Extreme Ultraviolet Beam. This is the intensity of the probe reconstructed from the time-resolved ptychography datasets. The spatial units are in μm, the units of the lineouts are arbitrary units of intensity. The beam diameters are reported as full-width at half-maximum values.

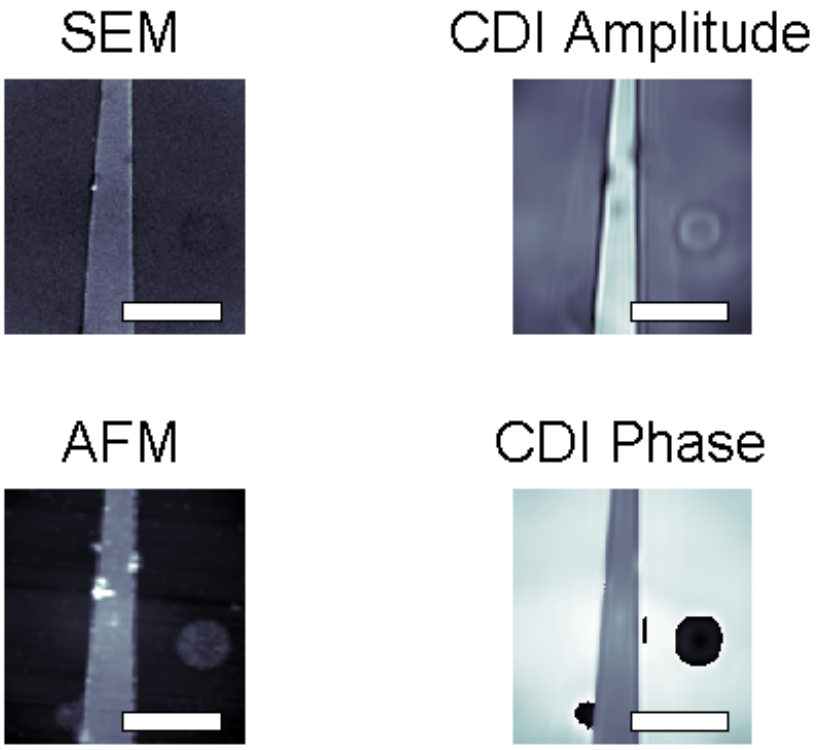

Figure 7.13: Comparison of Imaging Modalities for Tapered Nano-Antenna. Top left: scanning electron microscope image. Top right: amplitude of the coherent diffractive imaging reconstruction. Bottom left: atomic force microscope image. Bottom right: phase of the coherent diffractive imaging reconstruction. The scale bar in all images is 5 μm. In every image, the tapered nano-antenna can be observed. Furthermore, a small circular feature is present to the right of the nano-antenna. The contrast of this feature is different in each image.

One such histogram is shown in figure 7.14.

In this histogram, distance from the center is the amplitude of the complex value, and rotations correspond to phase differences. Horizontal and vertical shifts correspond to differences in the real and imaginary components of the complex value, respectively.

For the images of the nano-antenna, two distinct peaks can be seen. The largest peak is closer to the center. This corresponds to pixels that have the reflectivity of silicon (i.e. the substrate). The other peak corresponds to the reflectivity of nickel (i.e. the nano-antenna). Relative shifts in the locations of these peaks are a direct indication of the ultrafast dynamics being studied. In order to better address those dynamics, the histograms are used to determine which pixels in the image are of the nano-antenna, which are of the substrate, and which are of neither.

The different peaks of the histogram are determined by iteratively selecting the largest value in the histogram and all adjacent, non-zero values. This masks out the region corresponding to the substrate as shown in figure 7.15. On the second iteration of this, the pixels within this first mask are ignored, so that the new largest value is that of the nano-antenna peak. Thus a second mask is formed containing only those reflectivity values that belong to the nano-antenna.

Upon creating the two masks for the substrate and nano-antenna, there are regions of the histogram that remained unassigned. This region is primarily the circular feature to the side of the nano-antenna, which correctly is neither substrate nor nano-antenna. This region also contains the area between the nano-antenna and the substrate, where due to the finite resolution of the imaging system, the values are likely a blend between the two. All of the pixels in this third histogram mask are excluded from subsequent dynamics analysis so that only the effects of the nano-antenna and the substrate may be considered.

Since the different regions have been identified, the effect of the different materials on the complex reflectivity can be accounted for separately. This Fresnel reflectivity contains a phase that is distinct from the phase induced by the topography of the sample. By removing

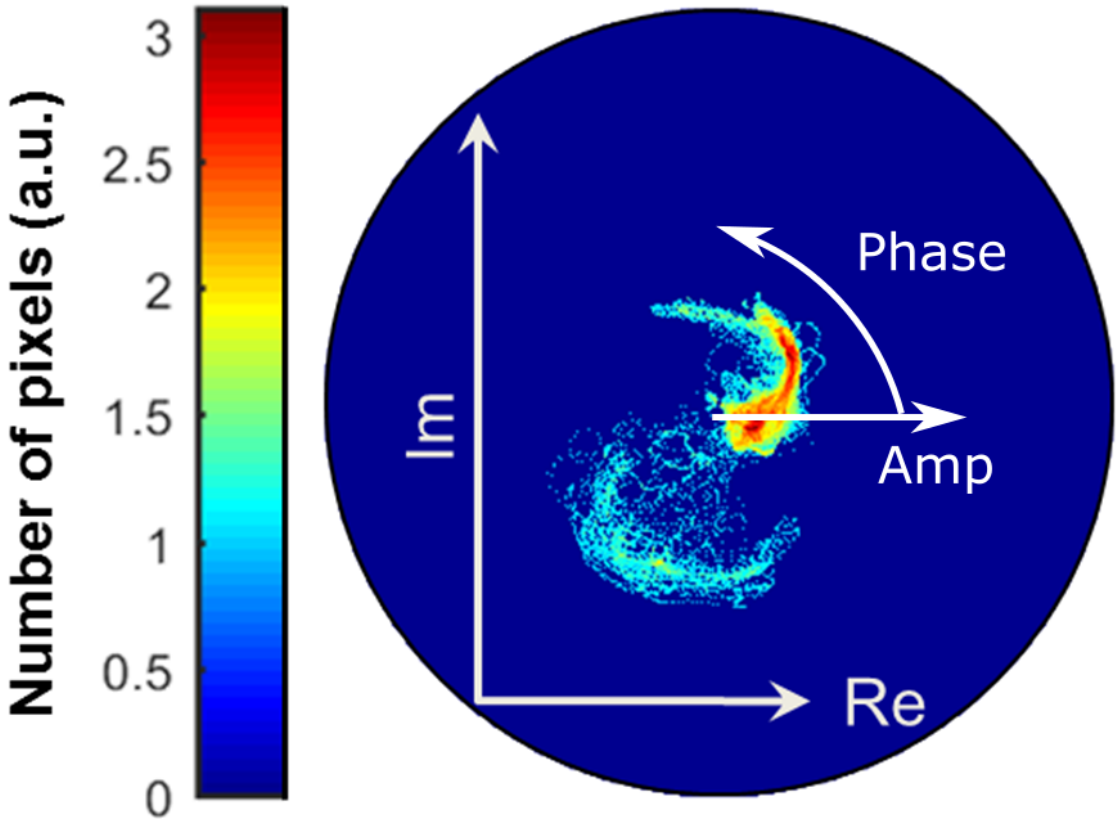

Figure 7.14: Two-Dimensional Histogram of Complex Image. The color of the plot corresponds to the number of pixels in the image that have a given complex value. The entirety of the plot is the region of complex space bounded by the unit circle. Distance from the center is the amplitude of the complex reflectivity, rotations about the center are differences in the phase. The horizontal dimension and vertical dimension are the real and imaginary axes, respectively.

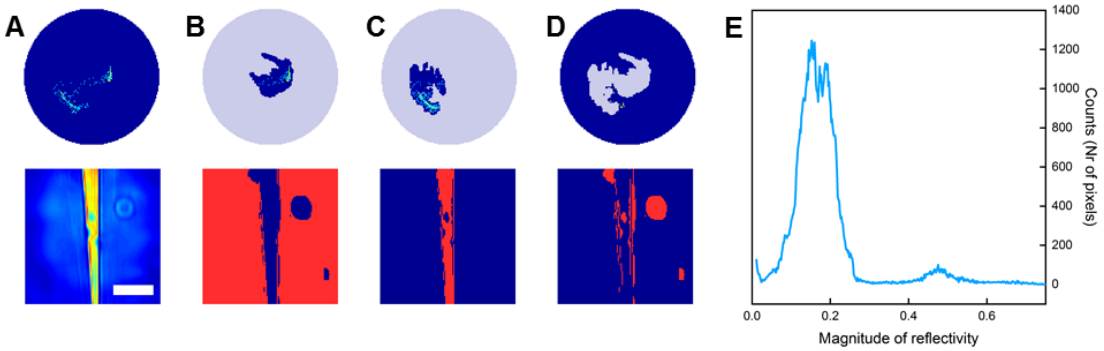

Figure 7.15: Image Segmentation with Complex Histograms. (A-D) Top: two-dimensional histograms with the different peak highlighted. These peaks correspond to the regions shown in the bottom row. The scale bar is 5 μm. E) One-dimensional histogram as a function of amplitude only. In this histogram the peaks are less well separated, and the assignment of the mask constructed in D is not possible.

the Fresnel phase, the only remaining phase is that from the height of the nano-antenna. The Fresnel phases are removed in the nano-antenna region and the substrate region according to the reflectivities of nickel and silicon, respectively [93].

Once the Fresnel phase is removed, the full phase image is unwrapped using a 2D Goldstein branch cut phase unwrapping algorithm [78, 81]. This final phase is converted into height, yielding height images of the nano-antenna.

7.4.2.2 Finite Element Simulation of Nano-Antenna Dynamics

In order to understand the thermal transport and acoustic wave dynamics that are induced by the pump light, a numerical simulation of the heat-driven displacement is performed and propagated through time [42]. This simulation is performed on a two-dimensional cross-section of the tapered nano-antenna at two different thicknesses (1.5 μm and 2.2 μm). In both simulations a height of 20.5 nm was used for the nano-antenna.

The substrate was chosen to be sufficiently deep so that acoustic waves reflected from the bottom of the numerical window would not be able to propagate back to the nano-structure during the course of the simulation. Even so, non-reflecting boundaries were used at the bottom, and at the left and right of the numerical window to suppress any possible reflection. The side and bottom of the substrate were made to be thermally insulating, while the top of the substrate and nano-antenna were free and insulating. The boundary between the nano-structure and the substrate has a thermal boundary resistivity of 5 mK*m/W to account for possible native oxides, interface roughness, or quasi-ballistic effects [97, 216]. The material properties for this simulation are tabulated in table 7.1

A similar model to [169] is used, under the approximation that the phonon temperature starts high (600 K for the 1.5 μm simulation, 450 K for the 2.2 μm simulation). This instantaneous temperature rise leads to thermal expansion that is observed experimentally. Additional simulations were performed to ascertain that the different initial temperatures correspond to a re-scaling of the extent of the surface deformation, but do not substantially

Materials	Nickel (Ni)	Silicon (Si)
k (W/(m K))	90.9 [45]	149 [45]
ρ (kg/m^3)	8900 [45]	2330 [45]
α (10^{-6} K^{-1})	12.77 [116]	3 [173]
C_p (J/(kg K))	456 [45]	710 [48]
E (GPa)	219 [169]	-
ν	0.31 [169]	-
C_{11} (GPa)	-	166 [98]
C_{12} (GPa)	-	64 [98]
C_{44} (GPa)	-	80 [98]

Table 7.1: Material Properties for Finite Element Analysis Simulation. The bracketed numbers correspond to references to literature. The material properties are as follows: k is the thermal conductivity, ρ is the density, α is the coefficient of thermal expansion, C_p is the heat capacity at constant pressure, E is the Young's modulus, ν is the Poisson's ratio, and C_{ij} is the i,jth component of the elastic tensor.

alter the functional form or the time scale of these dynamics. Thus, despite the two simulations occurring at different fluences, they can be used to study the same dynamics at different spatial locations in the nano-antenna.

These simulations are compared to the diffraction patterns in the ptychography datasets in figure 7.16. Frames from the simulation are shown in the bottom half of the figure, highlighting the acoustic waves that travel through the nickel. In the top right of the figure, the diffraction efficiency is calculated (Equation 7.1) for both the simulated nano-antenna dynamics and for the experimental diffraction patterns. The two show agreement, which lends credence to the applicability of the two-dimensional approximation used in the simulation.

7.4.2.3 Discussion

The reconstructions, having been segmented and converted into pure height maps, are displayed in figure 7.17 for selected time delays. The entire 14 frame movie can be seen in figure 7.18. The thermal expansion of the nano-antenna can be immediately observed in these height maps. Furthermore, the relative rotation of the peaks in the histograms show this average expansion more clearly. This can be seen in the subsets of figure 7.17. In these reconstructed height maps, the wave traveling across the nano-antenna can be observed. This is the generalized Lamb wave that is seen in the simulations (Figure 7.16). Furthermore, the expansion in the nano-antenna is different at different locations along the nano-antenna, corresponding with different cross-sectional widths.

These acoustic dynamics can be seen most clearly in the early times, where impulsive excitation at the edges of the structure are present, accompanied by a depression in the substrate adjacent to the nano-antenna. The expansion reached a maximum at $\approx$45 ps. After this, the distortion from the edges propagates to the center. The inhomogeneous changes through the length of the nano-antenna can be seen at 405 ps as the narrower end decreases in height while the thicker end increases.

In order to better examine these spatially varying dynamics, two different cross sections

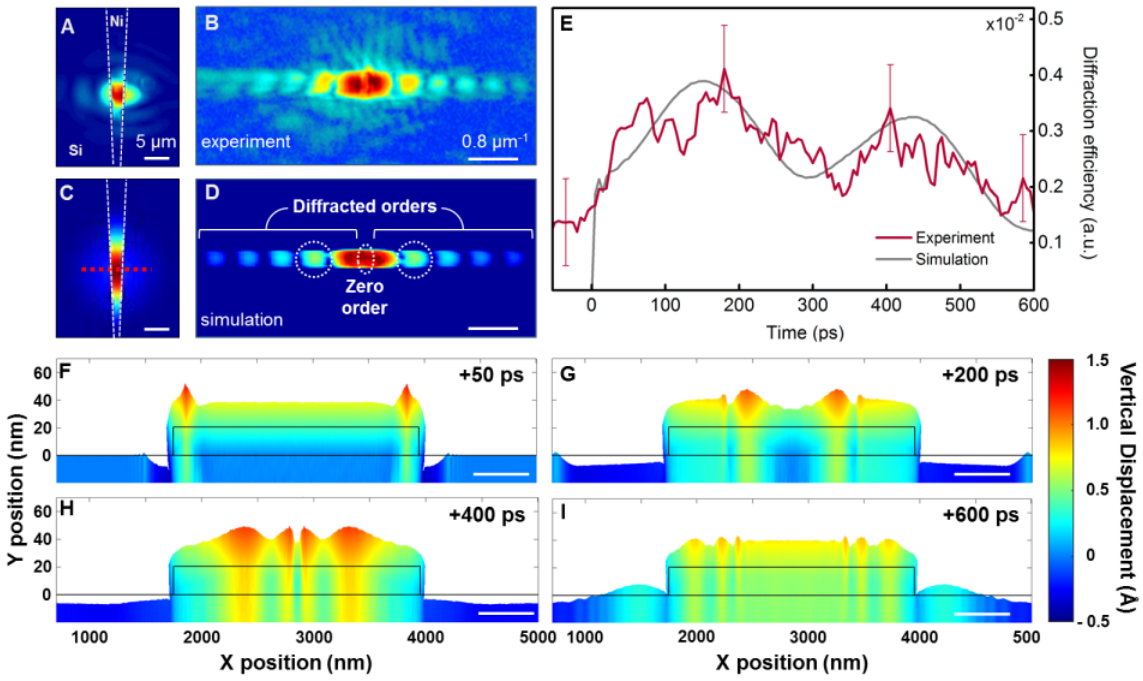

Figure 7.16: Dynamics in Tapered Nano-Antenna Compared to Simulation. A) Reconstructed image of the nickel nano-antenna, multiplied by the reconstructed probe. B) Example diffraction pattern from the experimental measurements. C) Simulation of the nickel nano-antenna with the red dashed line showing which cross section was simulated. D) Simulated diffraction pattern from the finite element analysis simulation. E) Comparison of the diffraction efficiency in the experiment and simulation as a function of time. Both show a two-lobed functional form after time zero, corresponding to the same acoustic dynamics. F-I) Frames from the finite element analysis simulation showing the surface deformation of the nano-antenna and showing the acoustic wave propagating through the structure. These surface deformations have been exaggerated by a factor of 250 to aid in visual clarity.

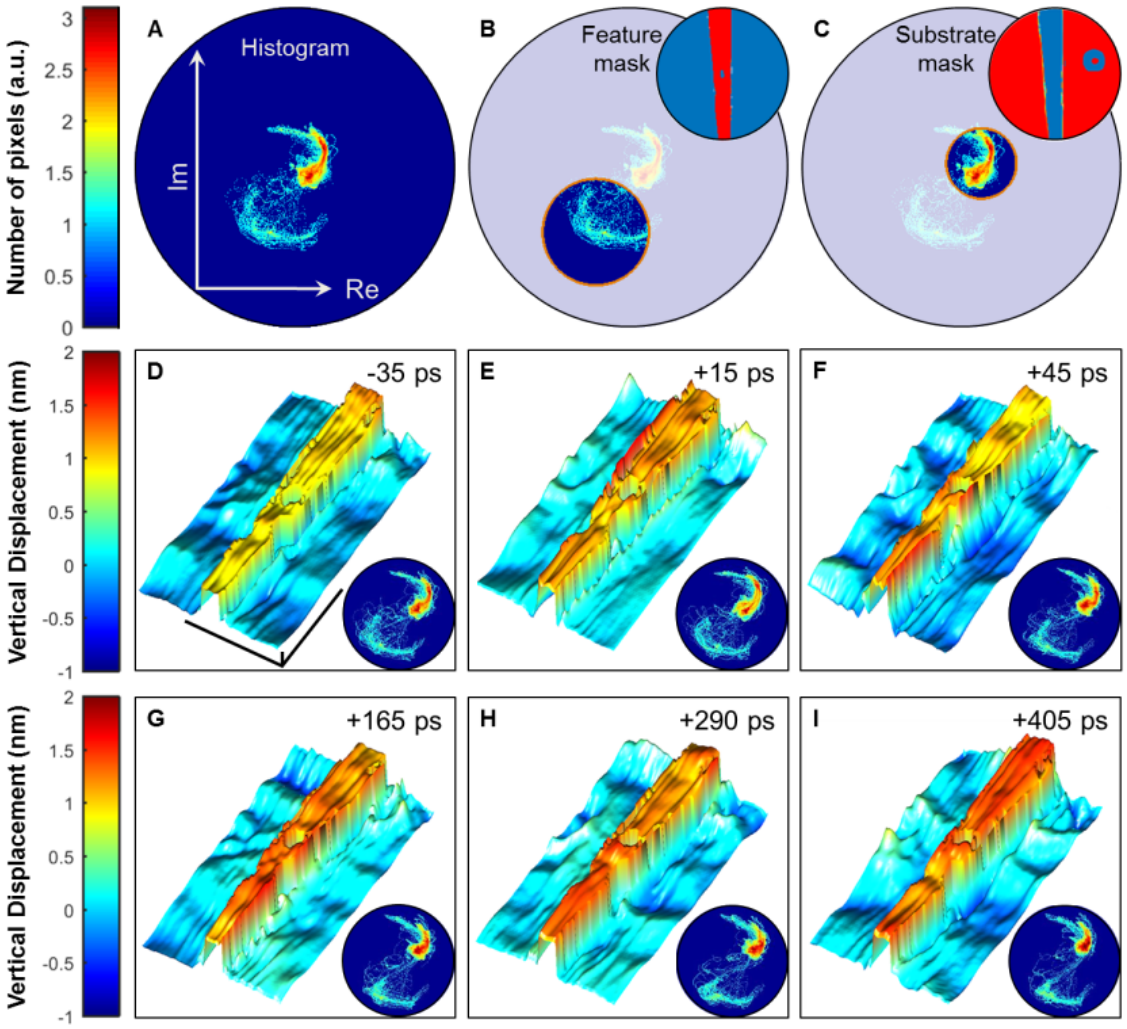

Figure 7.17: Ptychographic Reconstructions of Tapered Nano-Antenna. A) A representative complex histogram showing the distribution of different complex reflectivities in the reconstructed image. B-C) Different peaks in the histogram are selected in order to isolate the different regions of the image. Using these masks, the Fresnel reflectivity can be removed from each, leaving only the geometric phase from the different topography. D-I) Height maps from the phase of the reconstruction with the Fresnel phase removed. The subsets show the corresponding histograms for each of these time delays. The thermal expansion of the nano-antenna can be observed in the changing of the height between frames. Furthermore, evidence of the acoustic wave traveling across the nano-antenna is present. The different dynamics at different thicknesses of the nano-antenna can be seen here. The scale bar in D applies to all images, and is 5 μm laterally and 0.5 Åvertically.

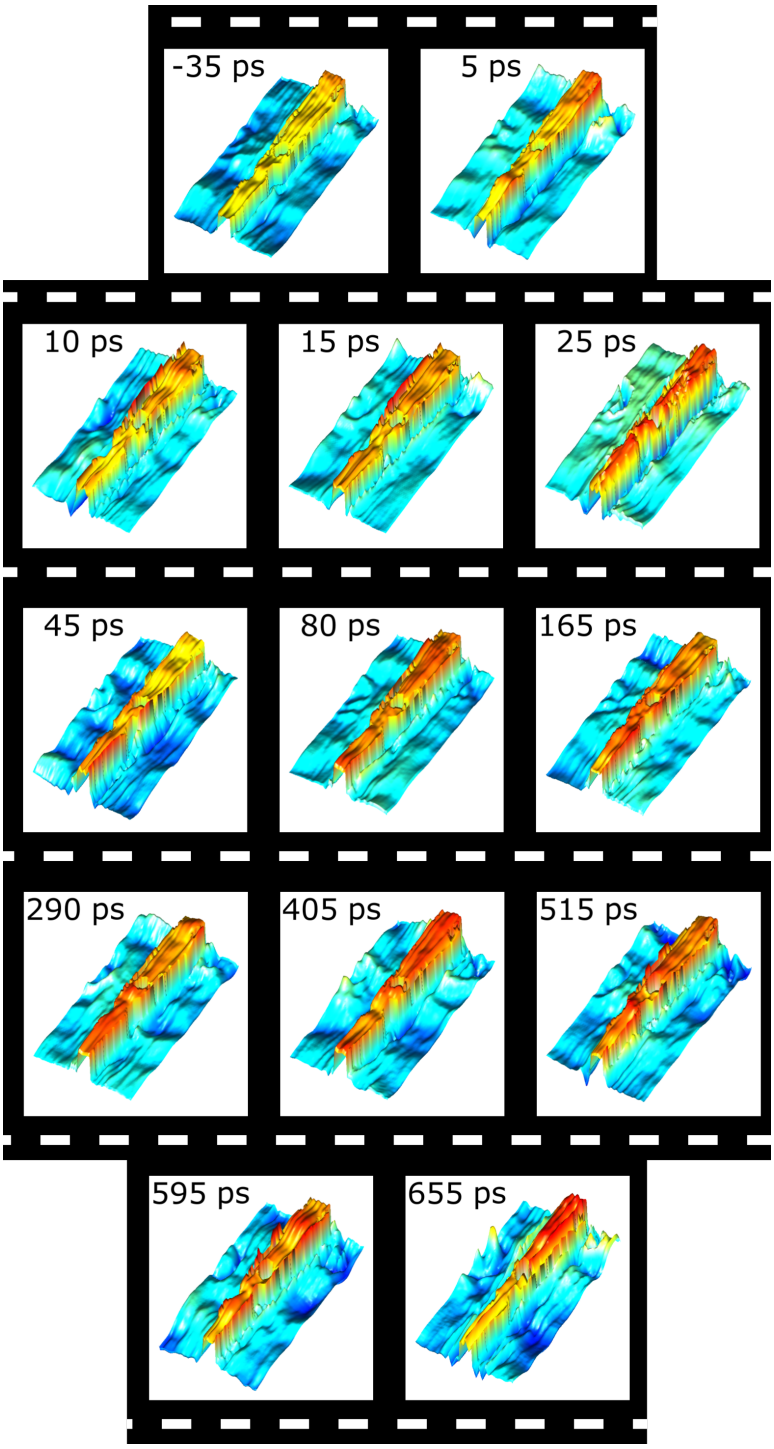

Figure 7.18: Movie of Acoustic Dynamics in Tapered Nano-Antenna. Thirteen height maps from the reconstructed complex images of the tapered nano-antenna. Each frame is from a different pump-probe delay. Putting them all together yields a nano-scale movie of the acoustic wave propagation.

of the nano-antenna are analyzed. These two cross-sections have widths of 1.5 μm and 2.2 μm, corresponding to the two widths that were simulated. A 0.5 μm by 0.5 μm area on the nano-antenna was averaged and compared to the average a 0.5 μm by 1.1 μm area of the substrate that was located 2.6 μm from the nano-antenna. The ratio of these average reflectivities was calculated, and from that the average phase difference, and thus height, was determined. This was calculated for each time delay at both of the cross-sections. The result of this analysis is in figure 7.19 along with the same quantities calculated from the finite element analysis simulation. The errorbars in the experimental measurement are derived from the standard deviation of the height different among the before time zero frames, in which no dynamics are occurring and thus all fluctuations are due to noise in the system.

The overall scaling of the transient heights in figure 7.19 do not agree. This is likely due to a scaling of the simulation resulting from a different pump fluence being used in the simulation as compared to the experiment. Importantly, the dynamics observed in the different cross sections of the nano-antenna are similar in overall shape to those seen in the simulation. They are not expected to fully agree, as the simulations are two-dimensional, and thus do not capture dynamics along the long dimension of the nano-antenna. Furthermore, the dynamics in these cross-sections are distinct from each other, displaying that there are spatially varying dynamics along the nano-antenna.

In order to quantify the axial precision, the height difference between the pump on and pump off reconstructed images was calculated for all times before the infrared pulse. The standard deviation of this differential value was calculated for various regions throughout the image. The largest variance observed was 0.009 radians, corresponding to 0.04 nm, thus a conservative estimate of the precision of this measurement is 0.5 Å. This quantity differs from the precision of the phase in a single pixel. That value was calculated by measuring the standard deviation in the phase value of each pixel in the 14 pump off images. The distribution of this variance was fit to a Gaussian profile to extract a mean value of 0.167 rad, corresponding to 0.77 nm. The histogram of this distribution of pixel by pixel standard

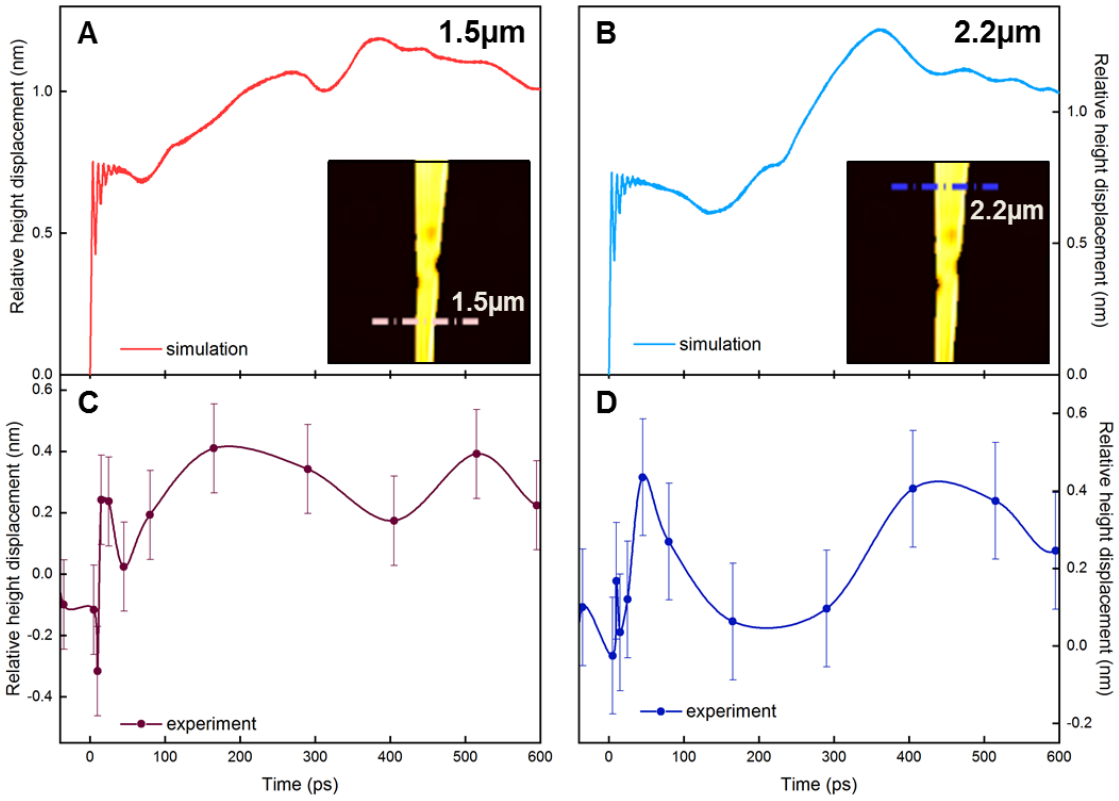

Figure 7.19: Demonstration of Spatially Varying Dynamics. A-B) Simulated change in height of the nano-antenna as a function of time along the 1.5 μm and 2.2 μm lineouts, respectively. The location of these lineouts are shown in the subsets. C-D) Experimental change in height of the nano-antenna as a function of time for these same lineouts. The simulated and experimental transient height changes have similar form, indicating some level of agreement. Full agreement should not be expected due to the assumptions made in the simulation. The experimental traces show that the dynamics in the nano-antenna are spatially varying.

deviations is in figure 7.20 along with the Gaussian fit to the distribution.

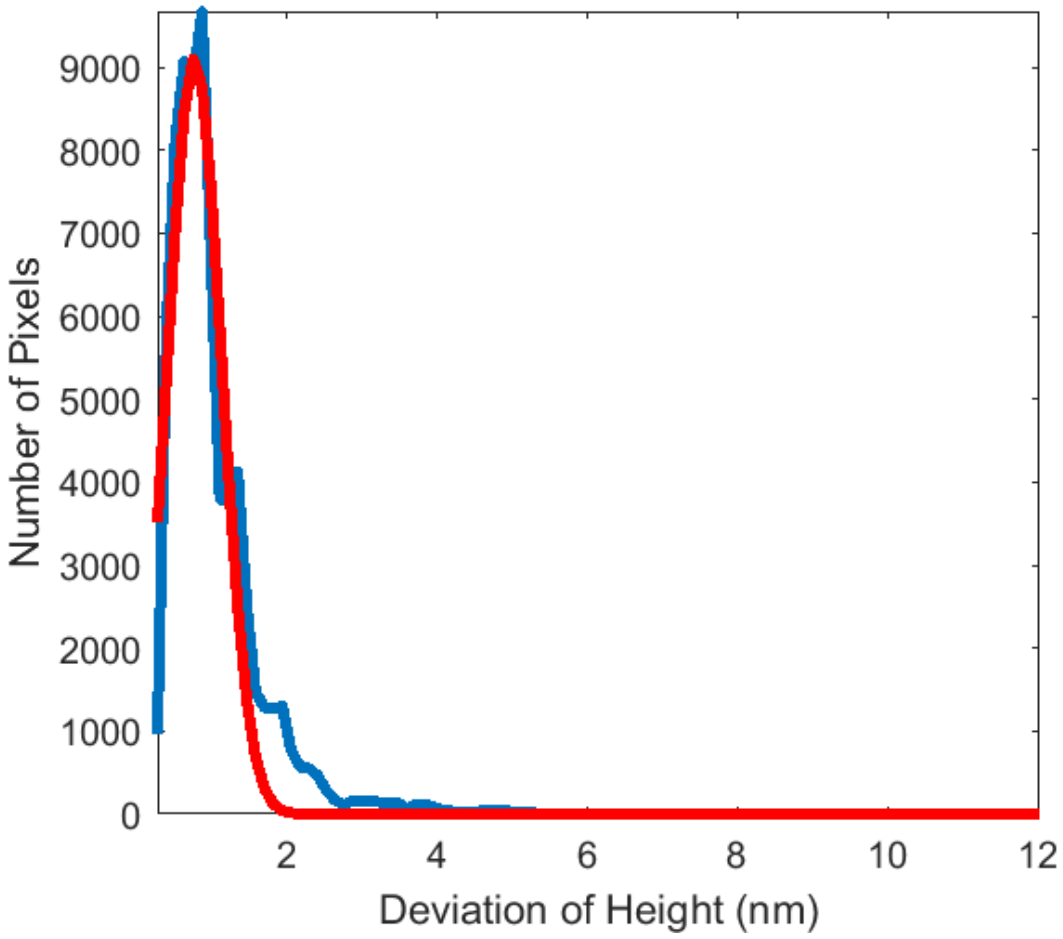

Figure 7.20: Quantification of Axial Precision. The standard deviation in each pixel across the reference images (those without the pump light present) are shown here in a histogram (blue line). This distribution is fit to a Gaussian in order to extract the position of the peak. This peak is located at 0.77 nm. This indicates that the mean standard deviation of the height measurement, on a per pixel basis, is 0.77 nm. This is used as the axial precision of a single pixel in the reconstructed images.

Chapter 8

Conclusion and Future Work

8.1 Summary

Coherent diffractive imaging (chapter 2) has proven to be a powerful tool in x-ray and extreme ultraviolet imaging. Specifically, the redundant information that is present in ptychography coherent diffractive imaging has made this technique extremely robust. By making use of multiple illumination beams (chapter 4), the field of view that can be imaged in a scan is greatly improved. Furthermore, the technique of spatially separated beams of orthogonal modes (chapter 3) has allowed for polarization resolved imaging, with both polarizations being resolved in a single scan.

The application of ptychographic imaging to the study of practical samples is the ultimate goal of technique development. In chapter 6, colloidal crystals were studied and various scattering analyses were applied to the extreme ultraviolet regime. Not only does this elucidate properties of the colloidal crystal in question, but it paves the way for future studies on inverse lattices patterned with these colloidal crystal as templates.

The most influential property of light created through high harmonic generation (chapter 5) is the ultrafast nature. By implementing pump-probe spectroscopy techniques with ptychography coherent diffractive imaging, a new microscope was developed that retains the high temporal and spatial resolutions that these techniques offer independently (chapter 7). Using this new microscope, the acoustic dynamics in nickel gratings were imaged as validation, and the dynamics in isolated nano-structures were imaged and used to benchmark

simulations.

8.2 Future Possibilities

All of the work in this thesis has horizons before it, wherein new developments can be made.

The multiple beam ptychography techniques can be applied to different microscopes beyond the optical microscopes used in the initial studies. Modern development of high harmonic sources that use more than one beam is ongoing [59]. With these systems combined with multiple beam ptychography, the advantages of extreme ultraviolet light imaging can be deployed with higher throughput. Furthermore, the development of ptychography algorithms is ever ongoing. Recently, the possibility for attosecond coherent diffractive imaging has been developed [185]. This is done by improving upon the multiple mode ptychography algorithms. This improvement to the multiple mode algorithm is also an improvement to the multiple beam ptychography technique, and should allow for more beams to be used.

The studies of colloidal crystals can be viewed as a starting point for understanding the properties of novel materials. Using the colloidal crystals as templates, inverse lattices can be fabricated that have new physical properties that are as of yet unknown. By harnessing the capabilities presented here, these inverse lattices can also be probed to garner understanding of these new electronic and magnetic properties.

The time resolved microscope as presented here, is capable of measuring dynamics on much shorter time scales that these acoustic dynamics. This leaves open the doorway to measuring femtosecond scale dynamics, such as spin transfer [34, 238].

The time resolved imaging presented here is limited in temporal resolution by the duration of the pump and probe pulses. These pulses are not, however, the shortest achievable. Using high harmonic generation, attosecond pulses have been generated [94, 119, 176]. Using these pulses as both the pump and the probe will allow for the interrogation of matter at even shorter time scales. Furthermore, by using higher energy harmonics [36, 181], these

dynamics can be measured with yet higher spatial resolution.

The techniques used in this microscope can also be developed further. The use of ptychography at each pump-probe delay is inefficient when compared to techniques that use a single diffraction pattern. Combining in-situ coherent diffractive imaging [136] with pump-probe measurements will achieve the same spatial and temporal resolutions with only a fraction of the data collection.

Bibliography

[1] Brian Abbey, Keith A. Nugent, Garth J. Williams, Jesse N. Clark, Andrew G. Peele, Mark A. Pfeifer, Martin de Jonge, and Ian McNulty. Keyhole coherent diffractive imaging. Nature Physics, 4:394–398, 2008.

[2] Brian Abbey, Garth J. Williams, Mark A. Pfeifer, Jesse N. Clark, Corey T. Putkunz, Angela Torrance, Ian McNulty, T. M. Levin, Andrew G. Peele, and Keith A. Nugent. Quantitative coherent diffractive imaging of an integrated circuit at a spatial resolution of 20 nm. Applied Physics Letters, 93:214101, 2008.

[3] H. Abraham and J. Lemoine. Disparition instantée du phénoméne de Kerr. Comptes Rendus Hebdomadaires des Séances de L'Académie des Sciences, 129:206–208, 1899.

[4] Daniel E. Adams, Leigh S. Martin, Matthew D. Seaberg, Dennis F. Gardner, Henry C. Kapteyn, and Margaret M. Murnane. A generalization for optimized phase retrieval algorithms. Optics Express, 20(22):24778–24790, 2012.

[5] Ofir E. Alon, Vitali Averbukh, and Nimrod Moiseyev. Selection Rules for the High Harmonic Generation Spectra. Physical Review Letters, 80(17):3743–3746, 1998.

[6] M. Altarelli, R. P. Kurta, and I. A. Vartanyants. X-ray cross-correlation analysis and local symmetries of disordered systems: General theory. Physical Review B, 82:104207, 2010.

[7] Priscilla D. Antunez, Douglas M. Bishop, Yu Luo, and Richard Haight. Efficient kesterite solar cells with high open-circuit voltage for applications in powering distributed devices. Nature Energy, 2:884–890, 2017.

[8] David Attwood. Soft X-Rays and Extreme Ultraviolet Radiation: Principles and Applications. Cambridge University Press, 1999.

[9] B. A. Auld. Acoustic fields and waves in solids. Wiley, New York, 1973.

[10] Sterling Backus, Randy Bartels, Sarah Thompson, Robert Dollinger, Henry C. Kapteyn, and Margaret M. Murnane. High-efficiency, single-stage 7-kHz high-average-power ultrafast laser system. Optics Letters, 26(7):465–467, 2001.

[11] Sterling Backus, Charles G. Durfee III, Margaret M. Murnane, and Henry C. Kapteyn. High power ultrafast lasers. Review of Scientific Instruments, 69(3):1207–1223, 1998.

[12] Albert V. Baez. Fresnel Zone Plate for Optical Image Formation Using Extreme Ultraviolet and Soft X Radiation. Journal of the Optical Society of America, 51(4):405–412, 1961.

[13] Peter D. Baksh, Michal Odstrčil, Hyun-Su Kim, Stuart A. Boden, Jeremy G. Frey, and William S. Brocklesby. Wide-field broadband extreme ultraviolet transmission ptychography using a high-harmonic source. Optics Letters, 41(7):1317–1320, 2016.

[14] Andrius Baltuška, Zhiyi Wei, Maxim S. Pshenichnikov, and Douwe A. Wiersma. Optical pulse compression to 5 fs at a 1-MHz repetition rate. Optics Letters, 22(2):102–104, 1997.

[15] Michael T. Barako, Aditya Sood, Chi Zhang, Junjie Wang, Takashi Kodama, Mehdi Asheghi, Xiaolin Zheng, Paul V. Braun, and Kenneth E. Goodson. Quasi-ballistic Electronic Thermal Conduction in Metal Inverse Opals. Nano Letters, 16:2754–2761, 2016.

[16] Randy A. Bartels, Ariel Paul, Hans Green, Henry C. Kapteyn, Margaret M. Murnane, Sterling Backus, Ivan P. Christov, Yanwei Liu, David Attwood, and Chris Jacobsen. Generation of Spatially Coherent Light at Extreme Ultraviolet Wavelengths. Science, 297:376–378, 2002.

[17] Brett Barwick, Hyun Soon Park, Oh-Hoon Kwon, J. Spencer Baskin, and Ahmed H. Zewail. 4D Imaging of Transient Structures and Morphologies in Ultrafast Electron Microscopy. Science, 322:1227–1231, 2008.

[18] R. H. T. Bates. Fourier phase problems are uniquely solvable in more than one dimension I: Underlying theory. Optik, 61(3):247–262, 1981.

[19] R. H. T. Bates and J. M. Rodenburg. Sub-ångström transmission microscopy: A Fourier transform algorithm for microdiffraction plane intensity information. Ultramicroscopy, 31:303–307, 1989.

[20] Darren J. Batey, Daniel Claus, and John M. Rodenburg. Information multiplexing in ptychography. Ultramicroscopy, 138:13–21, 2014.

[21] Charles Bevis, Robert Karl Jr., Jonathan Reichanadter, Dennis F. Gardner, Christina Porter, Elisabeth Shanblatt, Michael Tanksalvala, Giulia F. Mancini, Henry Kapteyn, Margaret Murnane, and Daniel Adams. Multiple beam ptychography for large field-of-view, high throughput, quantitative phase contrast imaging. Ultramicroscopy, 184:164–171, 2018.

[22] Michael A. Boles, Michael Engel, and Dmitri V. Talapin. Self-Assembly of Colloidal Nanocrystals: From Intricate Structures to Functional Materials. Chemical Reviews, 116:11220–11289, 2016.

[23] Alexey Bosak, Irina Snigireva, Kirill S. Napolskii, and Anatoly Snigirev. High-Resolution Transmission X-ray Microscopy: A New Tool for Mesoscopic Materials. Advanced Materials, 22:3256–3259, 2010.

[24] D. J. Bradley, B. Liddy, and W. E. Sleat. Direct linear measurement of ultrashort light pulses with a picosecond streak camera. Optics Communications, 2(8):391–395, 1971.

[25] Yu. M. Bruck and L. G. Sodin. On the ambiguity of the image reconstruction problem. Optics Communications, 30(3):304–308, 1979.

[26] Fabrizio Carbone, Oh-Hoon Kwon, and Ahmed H. Zewail. Dynamics of Chemical Bonding Mapped by Energy-Resolved 4D Electron Microscopy. Science, 325:181–184, 2009.

[27] J. N. Cederquist, J. R. Fienup, J. C. Marron, and R. G. Paxman. Phase retrieval from experimental far-field speckle data. Optics Letters, 13(8):619–621, 1988.

[28] F. Cerrina, G. Margaritondo, J. H. Underwood, M. Hettrick, M. A. Green, L. J. Brillson, A. Franciosi, H. Höchst, P. M. Deluca Jr., and M. N. Gould. Maximum: A Scanning Photoelectron Microscope at Aladdin. Nuclear Instruments and Methods in Physics Research, 266:303–307, 1988.

[29] Zenghu Chang, Andy Rundquist, Haiwen Wang, Margaret M. Murnane, and Henry C. Kapteyn. Generation of Coherent Soft X Rays at 2.7 nm Using High Harmonics. Physical Review Letters, 79(16):2967–2970, 1997.

[30] Weilun Chao, Bruce D. Harteneck, J. Alexander Liddle, Erik H. Anderson, and David T. Attwood. Soft X-ray microscopy at a spatial resolution better than 15 nm. Nature, 435:1210–1213, 2005.

[31] Henry N. Chapman. Phase-retrieval X-ray microscopy by Wigner-distribution deconvolution. Ultramicroscopy, 66:153–172, 1996.

[32] Henry N. Chapman, Anton Barty, Stefano Marchesini, Aleksandr Noy, Stefan P. Hau-Riege, Congwu Cui, Malcolm R. Howells, Rachel Rosen, Haifeng He, John C. H. Spence, Uwe Weierstall, Tobias Beetz, Chris Jacobsen, and David Shapiro. High-resolution ab initio three-dimensional x-ray diffraction microscopy. Journal of the Optical Society of America A, 23(5):1179–1199, 2006.

[33] Henry N. Chapman and Keith A. Nugent. Coherent lensless X-ray imaging. Nature Photonics, 4:833–839, 2010.

[34] Claude Chappert, Albert Fert, and Frédéric Nguyen Van Dau. The emergence of spin electronics in data storage. Nature Materials, 6:813–823, 2007.

[35] Cong Chen, Zhensheng Tao, Adra Carr, Piotr Matyba, Tibor Szilvási, Sebastian Emmerich, Martin Piecuch, Mark Keller, Dmitriy Zusin, Steffen Eich, Markus Rollinger, Wenjing You, Stefan Mathias, Uwe Thumm, Manos Mavrikakis, Martin Aeschlimann,

Peter M. Oppeneer, Henry Kapteyn, and Margaret Murnane. Distinguishing attosecond electron – electron scattering and screening in transition metals. Proceedings of the National Academy of Sciences, 114(27):E5300–E5307, 2017.

[36] M.-C. Chen, P. Arpin, T. Popmintchev, M. Gerrity, B. Zhang, M. Seaberg, D. Popmintchev, M. M. Murnane, and H. C. Kapteyn. Bright, Coherent, Ultrafast Soft X-Ray Harmonics Spanning the Water Window from a Tabletop Light Source. Physical Review Letters, 105:173901, 2010.

[37] Ming-Chang Chen, Christopher Mancuso, Carlos Hernández-García, Franklin Dollar, Ben Galloway, Dimitar Popmintchev, Pei-Chi Huang, Barry Walker, Luis Plaja, Agnieszka A. Jarón-Becker, Andreas Becker, Margaret M. Murnane, Henry C. Kapteyn, and Tenio Popmintchev. Generation of bright isolated attosecond soft X-ray pulses driven by multicycle midinfrared lasers. Proceedings of the National Academy of Sciences, 111(23):E2361–E2367, 2014.

[38] Ivan P. Christov, Margaret M. Murnane, and Henry C. Kapteyn. High-Harmonic Generation of Attosecond Pulses in the "Single-Cycle" Regime. Physical Review Letters, 78(7):1251–1254, 1997.

[39] J. N. Clark, L. Beitra, G. Xiong, A. Higginbotham, D. M. Fritz, H. T. Lemke, D. Zhu, M. Chollet, G. J. Williams, M. Messerschmidt, B. Abbey, R. J. Harder, A. M. Korsunsky, J. S. Wark, and I. K. Robinson. Ultrafast three-dimensional imaging of lattice dynamics in individual gold nanocrystals. Science, 341:56–59, 2013.

[40] Jesse N. Clark, Loren Beitra, Gang Xiong, David M. Fritz, Henrik T. Lemke, Diling Zhu, Matthieu Chollet, Garth J. Williams, Marc M. Messerschmidt, Brian Abbey, Ross J. Harder, Alexander M. Korsunsky, Justin S. Wark, David A. Reis, and Ian K. Robinson. Imaging transient melting of a nanocrystal using an X-ray laser. Proceedings of the National Academy of Sciences, 112(24):7444–7448, 2015.

[41] Jesse N. Clark, Xiaojing Huang, Ross J. Harder, and Ian K. Robinson. Continuous scanning mode for ptychography. Optics Letters, 39(20):6066–6069, oct 2014.

[42] COMSOL. COMSOL Multiphysics Version 4.3b. COMSOL, Inc., Burlington, MA, 2013.

[43] Ray Conley, Chian Liu, Jun Qian, Cameron M. Kewish, Albert T. Macrander, Hanfei Yan, Hyon Chol Kang, Jörg Maser, and G. Brian Stephenson. Wedged multilayer Laue lens. Review of Scientific Instruments, 79:053104, 2008.

[44] P. B. Corkum. Plasma Perspective on Strong-Field Multiphoton Ionization. Physical Review Letters, 71(13):1994–1997, 1993.

[45] John A. Dean. Lange's Handbook of Chemistry. McGraw-Hill, Inc., 2005.

[46] A. J. DeMaria, D. A. Stetser, and H. Heynau. Self mode-locking of lasers with saturable absorbers. Applied Physics Letters, 8(7):174–176, 1966.

[47] Junjing Deng, Youssef S. G. Nashed, Si Chen, Nicholas W. Phillips, Tom Peterka, Rob Ross, Stefan Vogt, Chris Jacobsen, and David J. Vine. Continuous motion scan ptychography: characterization for increased speed in coherent x-ray imaging. Optics Express, 23(5):5438–5451, 2015.

[48] P. D. Desai. Thermodynamic Properties of Iron and Silicon. Journal of Physical and Chemical Reference Data, 15:967–983, 1986.

[49] Ana Diaz, Pavel Trtik, Manuel Guizar-Sicairos, Andreas Menzel, Pierre Thibault, and Oliver Bunk. Quantitative x-ray phase nanotomography. Physical Review B, 85:020104, 2012.

[50] M. DiDomenico, Jr. Small-Signal Analysis of Internal (Coupling-Type) Modulation of Lasers. Journal of Applied Physics, 35(10):2870–2876, 1964.

[51] Martin Dierolf, Pierre Thibault, Andreas Menzel, Cameron M. Kewish, Konstantins Jefimovs, Urne Schlichting, Konstanze Von König, Oliver Bunk, and Franz Pfeiffer. Ptychographic coherent diffractive imaging of weakly scattering specimens. New Journal of Physics, 12:1–14, 2010.

[52] Chengyuan Ding, Wei Xiong, Tingting Fan, Daniel D. Hickstein, Tenio Popmintchev, Xiaoshi Zhang, Mike Walls, Margaret M. Murnane, and Henry C. Kapteyn. High flux coherent super-continuum soft X-ray source driven by a single-stage, 10mJ, Ti:sapphire amplifier-pumped OPA. Optics Express, 22(5):6194–6202, 2014.

[53] Khuong Ba Dinh, Adabelle X. P. Ong, Hoang Vu Le, Clare A. Henderson, Cuong Van Vuong, Peter Hannaford, Trevor A. Smith, and Lap Van Dao. Coherent diffractive imaging of single layer microspheres. Journal of Applied Physics, 117:163102, 2015.

[54] Anthony D. Dinsmore, John C. Crocker, and Arjun G. Yodh. Self-assembly of colloidal crystals. Current Opinion in Colloid and Interface Science, 3:5–11, 1998.

[55] Jose A. Dominguez-Caballero, Nick Loomis, George Barbastathis, and Jerry Milgram. Techniques Based on Digital Multiplexing Holography for Three-Dimensional Object Tracking. Conference on Lasers and Electro Optics, 2007.

[56] Kevin M. Dorney, Jennifer L. Ellis, Carlos Hernández-García, Daniel D. Hickstein, Christopher A. Mancuso, Nathan Brooks, Tingting Fan, Guangyu Fan, Dmitriy Zusin, Christian Gentry, Patrik Grychtol, Henry C. Kapteyn, and Margaret M. Murnane. Helicity-Selective Enhancement and Polarization Control of Attosecond High Harmonic Waveforms Driven by Bichromatic Circularly Polarized Laser Fields. Physical Review Letters, 119:063201, 2017.

[57] Charles G. Durfee III, Andy R. Rundquist, Sterling Backus, Catherine Herne, Margaret M. Murnane, and Henry C. Kapteyn. Phase Matching of High-Order Harmonics in Hollow Waveguides. Physical Review Letters, 83(11):2187–2190, 1999.

[58] T. B. Edo, D. J. Batey, A. M. Maiden, C. Rau, U. Wagner, Z. D. Pešić, T. A. Waigh, and J. M. Rodenburg. Sampling in x-ray ptychography. Physical Review A, 87:053850, 2013.

[59] Jennifer L. Ellis, Kevin M. Dorney, Daniel D. Hickstein, Nathan J. Brooks, Christian Gentry, Carlos Hernández-García, Dmitriy Zusin, Justin M. Shaw, Quynh L. Nguyen, Christopher A. Mancuso, G. S. Matthijs Jansen, Stefan Witte, Henry C. Kapteyn, and Margaret M. Murnane. High harmonics with spatially varying ellipticity. Optica, 5(4):479–485, 2018.

[60] B. Enders, M. Dierolf, P. Cloetens, M. Stockmar, F. Pfeiffer, and P. Thibault. Ptychography with broad-bandwidth radiation. Applied Physics Letters, 104:171104, 2014.

[61] Y. Esashi, C.-T. Liao, B. Wang, N. Brooks, K. M. Dorney, H. Kapteyn, D. Adams, and M. Murnane. Ptychographic amplitude and phase reconstruction of bichromatic vortex beams. Optics Express, 26(26):34007–34015, 2018.

[62] Morteza Esmaeili, Jostein B. Fløystad, Ana Diaz, Kristin Høydalsvik, Manuel Guizar-Sicairos, Jens W. Andreasen, and Dag W. Breiby. Ptychographic X-ray Tomography of Silk Fiber Hydration. Macromolecules, 46:434–439, 2013.

[63] Tingting Fan, Patrik Gychtol, Ronny Knut, Carlos Hernández-García, Daniel Hickstein, Christian Gentry, Craig Hogle, Dmitriy Zusin, Kevin Dorney, Oleg Shpyrko, Oren Cohen, Ofer Kfir, Luis Plaja, Andreas Becker, Agnieszka Jaron-Becker, Margaret Murnane, Henry Kapteyn, and Tenio Popmintchev. Bright Circularly Polarized Soft X-Ray High Harmonics for X-Ray Magnetic Circular Dichroism. Conference on Lasers and Electro Optics, 2015.

[64] H. M. L. Faulkner and J. M. Rodenburg. Movable Aperture Lensless Transmission Microscopy: A Novel Phase Retrieval Algorithm. Physical Review Letters, 93(2):023903, 2004.

[65] M. Ferray, A. L'Huillier, X. F. Li, L. A. Lompré, G. Mainfray, and C. Manus. Multiple-harmonic conversion of 1064 nm radiation in rare gases. Journal of Physics B: Atomic, Molecular and Optical Physics, 21:L31–L35, 1988.

[66] A. Ferré, C. Handschin, M. Dumergue, F. Burgy, A. Comby, D. Descamps, B. Fabre, G. A. Garcia, R. Géneaux, L. Merceron, E. Mével, L. Nahon, S. Petit, B. Pons, D. Staedter, S. Weber, T. Ruchon, V. Blanchet, and Y. Mairesse. A table-top ultrashort light source in the extreme ultraviolet for circular dichroism experiments. Nature Photonics, 9:93–98, 2015.

[67] J. R. Fienup. Reconstruction of an object from the modulus of its Fourier transform. Optics Letters, 3(1):27–29, 1978.

[68] J. R. Fienup. Phase retrieval algorithms: a comparison. Applied Optics, 21(15):2758–2769, 1982.

[69] James R. Fienup. Phase retrieval algorithms: a personal tour [Invited]. Applied Optics, 52(1):45–56, 2013.

[70] Avner Fleischer, Ofer Kfir, Tzvi Diskin, Pavel Sidorenko, and Oren Cohen. Spin angular momentum and tunable polarization in high-harmonic generation. Nature Photonics, 8:543–549, 2014.

[71] R. L. Fork, C. H. Brito Cruz, P. C. Becker, and C. V. Shank. Compression of optical pulses to six femtoseconds by using cubic phase compensation. Optics Letters, 12(7):483–485, 1987.

[72] Stuart L. Friedman and J. M. Rodenburg. Optical demonstration of a new principle of far-field microscopy. Journal of Physics D: Applied Physics, 25:147–154, 1992.

[73] Si Gao, Peng Wang, Fucai Zhang, Gerardo T. Martinez, Peter D. Nellist, Xiaoqing Pan, and Angus I. Kirkland. Electron ptychographic microscopy for three-dimensional imaging. Nature Communications, 8:163, 2017.

[74] Dennis F. Gardner, Michael Tanksalvala, Elisabeth R. Shanblatt, Xiaoshi Zhang, Benjamin R. Galloway, Christina L. Porter, Robert Karl Jr., Charles Bevis, Daniel E. Adams, Henry C. Kapteyn, Margaret M. Murnane, and Giulia F. Mancini. Subwavelength coherent imaging of periodic samples using a 13.5 nm tabletop high-harmonic light source. Nature Photonics, 11:259–264, 2017.

[75] Dennis F. Gardner, Bosheng Zhang, Matthew D. Seaberg, Leigh S. Martin, Daniel E. Adams, Farhad Salmassi, Eric Gullikson, Henry Kapteyn, and Margaret Murnane. High numerical aperture reflection mode coherent diffraction microscopy using off-axis apertured illumination. Optics Express, 20(17):19050–19059, 2012.

[76] Alice P. Gast and William B. Russel. Simple ordering in complex fluids. Physics Today, 51(12):24–30, 1998.

[77] R. W. Gerchberg and W. O. Saxton. A Practical Algorithm for the Determination of Phase from Image and Diffraction Plane Pictures. Optik, 35(2):237–246, 1971.

[78] D. C. Ghiglia and M. D. Pritt. Two-dimensional phase unwrapping: theory, algorithms, and software. Wiley, New York, 1998.

[79] Shambhu Ghimire, Anthony D. DiChiara, Emily Sistrunk, Pierre Agostini, Louis F. DiMauro, and David A. Reis. Observation of high-order harmonic generation in a bulk crystal. Nature Physics, 7:138–141, 2011.

[80] T. M. Godden, R. Suman, M. J. Humphry, J. M. Rodenburg, and A. M. Maiden. Ptychographic microscope for three-dimensional imaging. Optics Express, 22(10):12513–12523, 2014.

[81] Richard M. Goldstein, Howard A. Zebker, and Charles L. Werner. Satellite radar interferometry: Two-dimensional phase unwrapping, 1988.

[82] Joseph W. Goodman. Introduction to Fourier Optics. Roberts & Company Publishers, Greenwood Village, 3rd edition, 2005.

[83] Manuel Guizar-Sicairos and James R. Fienup. Phase retrieval with transverse translation diversity: a nonlinear optimization approach. Optics Express, 16(10):7264–7278, 2008.

[84] T. E. Gureyev and K. A. Nugent. Rapid quantitative phase imaging using the transport of intensity equation. Optics Communications, 133:339–346, 1997.

[85] J. E. Han and Vincent H. Crespi. Tuning Fermi-Surface Properties through Quantum Confinement in Metallic Metalattices: New Metals from Old Atoms. Physical Review Letters, 86(4):696–699, 2001.

[86] J. E. Han and Vincent H. Crespi. Abrupt Topological Transitions in the Hysteresis Curves of Ferromagnetic Metalattices. Physical Review Letters, 89(19):197203, 2002.

[87] Tetsuo Harada, Junki Kishimoto, Takeo Watanabe, Hiroo Kinoshita, and Dong Gun Lee. Mask observation results using a coherent extreme ultraviolet scattering microscope at NewSUBARU. Journal of Vacuum Science & Technology B, 27:3203–3207, 2009.

[88] Tetsuo Harada, Masato Nakasuji, Yutaka Nagata, Takeo Watanabe, and Hiroo Kinoshita. Phase Imaging of Extreme-Ultraviolet Mask Using Coherent Extreme-Ultraviolet Scatterometry Microscope. Japanese Journal of Applied Physics, 52:06GB02, 2012.

[89] L. E. Hargrove, R. L. Fork, and M. A. Pollack. Locking of He-Ne laser modes induced by synchronous intracavity modulation. Applied Physics Letters, 5(1):4–5, 1964.

[90] Herman A. Haus. Mode-Locking of Lasers. IEEE Journal on Selected Topics in Quantum Electronics, 6(6):1173–1185, 2000.

[91] R. Hegerl and W. Hoppe. Dynamische Theorie der Kristallstrukturanalyse durch Elektronenbeugung im inhomogenen Primärstrahlwellenfeld. Berichte der Brunsen-Gesellschaft, 74(11):1148–1154, 1970.

[92] R. Hegerl and W. Hoppe. Phase evaluation in generalized diffraction (ptychography). Proceedings of the Fifth European Congress on Electron Microscopy, pages 628–629, 1972.

[93] B. L. Henke, E. M. Gullikson, and J. C. Davis. X-Ray Interactions: Photoabsorption, Scattering, Transmission, and Reflection at E = 50-30,000 eV, Z = 1-92. Atomic Data and Nuclear Data Tables, 54(2):181–342, 1993.

[94] M. Hentschel, R. Kienberger, Ch. Spielmann, G. A. Reider, N. Milosevic, T. Brabec, P. Corkum, U. Heinzmann, M. Drescher, and F. Krausz. Attosecond metrology. Nature, 414:509–513, 2001.

[95] Jorge N. Hernandez-Charpak, Kathleen M. Hoogeboom-Pot, Qing Li, Travis D. Frazer, Joshua L. Knobloch, Marie Tripp, Sean W. King, Erik H. Anderson, Weilun Chao, Margaret M. Murnane, Henry C. Kapteyn, and Damiano Nardi. Full Characterization of the Mechanical Properties of 11-50 nm Ultrathin Films: Influence of Network Connectivity on the Poisson's Ratio. Nano Letters, 17:2178–2183, 2017.

[96] M. Holler, A. Diaz, M. Guizar-Sicairos, P. Karvinen, Elina Färm, Emma Härkönen, Mikko Ritala, A. Menzel, J. Raabe, and O. Bunk. X-ray ptychographic computed tomography at 16 nm isotropic 3D resolution. Scientific Reports, 4:3857, 2014.

[97] Kathleen M. Hoogeboom-Pot, Jorge N. Hernandez-Charpak, Xiaokun Gu, Travis D. Frazer, Erik H. Anderson, Weilun Chao, Roger W. Falcone, Ronggui Yang, Margaret M. Murnane, Henry C. Kapteyn, and Damiano Nardi. A new regime of nanoscale thermal transport: Collective diffusion increases dissipation efficiency. Proceedings of the National Academy of Sciences, 112(16):4846–4851, 2015.

[98] Matthew A. Hopcroft, William D. Nix, and Thomas W. Kenny. What is the Young's Modulus of Silicon? Journal of Microelctromechanical Systems, 19(2):229–238, 2010.

[99] W. Hoppe. Beugung im inhomogenen Primärstrahlwellenfeld. I. Prinzip einer Phasenmessung von Elektronenbeugungsinterferenzen. Acta Crystallographica, 25:495–501, 1969.

[100] W. Hoppe. Trace structure analysis, ptychography, phase tomography. Ultramicroscopy, 10:187–198, 1982.

[101] Walter Hoppe. Beugung im inhomogenen Primärstrahlwellenfeld. III. Amplituden- und Phasenbestimmung bei unperiodischen Objekten. Acta Crystallographica, 25:508–514, 1969.

[102] Walter Hoppe and G. Strube. Beugung in inhomogenen Primärstrahlenwellenfeld. II. Lichtoptische Analogieversuche zur Phasenmessung von Gitterinterferenzen. Acta Crystallographica, 25:502–507, 1969.

[103] Xiaojing Huang, Kenneth Lauer, Jesse N. Clark, Weihe Xu, Evgeny Nazaretski, Ross Harder, Ian K. Robinson, and Yong S. Chu. Fly-scan ptychography. Scientific Reports, 5:9074, 2015.

[104] Xiaojing Huang, Hanfei Yan, Ross Harder, Yeukuang Hwu, Ian K. Robinson, and Yong S. Chu. Optimization of overlap uniformness for ptychography. Optics Express, 22(10):12634–12644, 2014.

[105] J. D. Jackson. Classical Electrodynamics. John Wiley & Sons, Hoboken, NJ, 3rd edition, 1999.

[106] J. B. Jones, J. V. Sanders, and E. R. Segnit. Structure of Opal. Nature, 204(4962):990–991, 1964.

[107] Hyon Chol Kang, Hanfei Yan, Robert P. Winarski, Martin V. Holt, Jörg Maser, Chian Liu, Ray Conley, Stefan Vogt, Albert T. Macrander, and G. Brian Stephenson. Focusing of hard x-rays to 16 nanometers with a multilayer Laue lens. Applied Physics Letters, 92:221114, 2008.

[108] Henry C. Kapteyn, Margaret M. Murnane, and Ivan P. Christov. Extreme Nonlinear Optics: Coherent X Rays from Lasers. Physics Today, pages 39–44, 2005.

[109] Robert M. Karl, Daniel E. Adams, Charles S. Bevis, Henry C. Kapteyn, and Margaret M. Murnane. Coherent Diffractive Imaging with Spaced-Apart Beams. United States Patent, 9,911,207, 2018.

[110] Robert Karl, Jr., Charles Bevis, Raymond Lopez-Rios, Jonathan Reichanadter, Dennis Gardner, Christina Porter, Elisabeth Shanblatt, Michael Tanksalvala, Giulia F. Mancini, Margaret Murnane, Henry Kapteyn, and Daniel Adams. Spatial, spectral, and polarization multiplexed ptychography. Optics Express, 23(23):30250–30258, 2015.

[111] Robert M. Karl Jr., Giulia F. Mancini, Joshua L. Knobloch, Travis D. Frazer, Jorge N. Hernandez-Charpak, Begoña Abad, Dennis F. Gardner, Elisabeth R. Shanblatt, Michael Tanksalvala, Christina L. Porter, Charles S. Bevis, Daniel E. Adams, Henry C. Kapteyn, and Margaret M. Murnane. Full-field imaging of thermal and acoustic dynamics in an individual nanostructure using tabletop high harmonic beams. Science Advances, 4:eaau4295, 2018.

[112] Ofer Kfir, Patrik Grychtol, Emrah Turgut, Ronny Knut, Dmitriy Zusin, Dimitar Popmintchev, Tenio Popmintchev, Hans Nembach, Justin M. Shaw, Avner Fleischer, Henry Kapteyn, Margaret Murnane, and Oren Cohen. Generation of bright phase-matched circularly-polarized extreme ultraviolet high harmonics. Nature Photonics, 9:99–105, 2014.

[113] Sean W. King, Harsono Simka, Dan Herr, Hiro Akinaga, and Mike Garner. Research Updates: The three M's (materials, metrology, and modeling) together pave the path to future nanoelectronic technologies. APL Materials, 1:040701, 2013.

[114] Paul Kirkpatrick and A. V. Baez. Formation of Optical Images by X-rays. Journal of the Optical Society of America, 38(9):766–774, 1948.

[115] Janos Kirz, Ade Harald, Erik Anderson, David Attwood, Chris Buckley, Sid Hellman, Malcolm Howells, Chris Jacobsen, Dieter Kern, Steve Lindaas, Ian McNulty, Menno Oversluizen, Harvey Rarback, Mark Rivers, Stephen Rothman, David Sayre, and Deming Shu. X-ray Microscopy with the NSLS Soft X-ray Undulator. Physica Scripta, 31:12–17, 1990.

[116] T. G. Kollie. Measurement of the thermal-expansion coefficient of nickel from 300 to 1000 K and determination of the power-law constants near the Curie temperature. Physical Review B, 16(11):4872–4881, 1977.

[117] J. M. Kosterlitz and D. J. Thouless. Ordering, metastability and phase transitions in two-dimensional systems. Journal of Physics C: Solid State Physics, 6:1181–1203, 1973.

[118] Jeffrey L. Krause, Kenneth J. Schafer, and Kenneth C. Kulander. High-Order Harmonic Generation from Atoms and Ions in the High Intensity Regime. Physical Review Letters, 68(24):3535–3538, 1992.

[119] Ferenc Krausz and Misha Ivanov. Attosecond physics. Reviews of Modern Physics, 81:163–234, 2009.

[120] P. Krehl and S. Engemann. August Toepler - the first who visualized shock waves. Shock Waves, 5:1–18, 1995.

[121] M. A. Kumakhov and V. A. Sharov. A neutron lens. Nature, 357:390–391, 1992.

[122] R. P. Kurta, M. Altarelli, E. Weckert, and I. A. Vartanyants. X-ray cross-correlation analysis applied to disordered two-dimensional systems. Physical Review B - Condensed Matter and Materials Physics, 85(18):1–19, 2012.

[123] Ruslan P. Kurta, Jeffrey J. Donatelli, Chun Hong Yoon, Peter Berntsen, Johan Bielecki, Benedikt J. Daurer, Hasan DeMirci, Petra Fromme, Max Felix Hantke, Filipe R. N. C. Maia, Anna Munke, Carl Nettelblad, Kanupriya Pande, Hemanth K. N. Reddy, Jonas A. Sellberg, Raymond G. Sierra, Martin Svenda, Gijs van der Schot, Ivan A. Vartanyants, Garth J. Williams, P. Lourdu Xavier, Andrew Aquila, Peter H. Zwart, and Adrian P. Mancuso. Correlations in Scattered X-Ray Laser Pulses Reveal Nanoscale Structural Features of Viruses. Physical Review Letters, 119:158102, 2017.

[124] T. Latychevskaia, G. F. Mancini, and F. Carbone. The role of the coherence in the cross-correlation analysis of diffraction patterns from two-dimensional dense monodisperse systems. Scientific Reports, 5:16573, 2015.

[125] Tatiana Latychevskaia and Hans-Werner Fink. Practical algorithms for simulation and reconstruction of digital in-line holograms. Applied Optics, 54(9):2424–2434, 2015.

[126] Sangsul Lee, Manuel Guizar-Sicairos, and Yasin Ekinci. A novel concept for actinic EUV mask review tool using a scanning lensless imaging method at the Swiss Light Source. Proceedings of SPIE, 9048:904811, 2014.

[127] Felix Lehmkühler, Birgit Fischer, Leonard Müller, Beatrice Ruta, and Gerhard Grübel. Structure beyond pair correlations: X-ray cross-correlation from colloidal crystals. Journal of Applied Crystallography, 49:2046–2052, 2016.

[128] Ben Leshem, Rui Xu, Yehonatan Dallal, Jianwei Miao, Boaz Nadler, Dan Oron, Nirit Dudovich, and Oren Raz. Direct single-shot phase retrieval from the diffraction pattern of separated objects. Nature Communications, 7:10820, 2016.

[129] M. Lewenstein, Ph. Balcou, M. Yu. Ivanov, Anne L'Huillier, and P. B. Corkum. Theory of high-harmonic generation by low-frequency laser fields. Physical Review A, 49(3):2117–2132, 1994.

[130] Anne L'Huillier and Ph. Balcou. High-Order Harmonic Generation in Rare Gases with a 1-ps 1053-nm Laser. Physical Review Letters, 70(6):774–777, 1993.

[131] Anne L'Huillier, Kenneth J. Schafer, and Kenneth C. Kulander. Theoretical aspects of intense field harmonic generation. Journal of Physics B: Atomic, Molecular and Optical Physics, 24:3315–3341, 1991.

[132] Peng Li and Andrew Maiden. Multi-slice ptychographic tomography. Scientific Reports, 8:2049, 2018.

[133] Peng Li and Andrew M. Maiden. Ten implementations of ptychography. Journal of Microscopy, 00(0):1–8, 2017.

[134] Tao Li, Andrew J. Senesi, and Byeongdu Lee. Small Angle X-ray Scattering for Nanoparticle Research. Chemical Reviews, 116:11128–11180, 2016.

[135] Haigang Liu, Zijian Xu, Xiangzhi Zhang, Yanqing Wu, Zhi Guo, and Renzhong Tai. Effects of missing low-frequency information on ptychographic and plane-wave coherent diffraction imaging. Applied Optics, 52(11):2416–2427, 2013.

[136] Yuan Hung Lo, Lingrong Zhao, Marcus Gallagher-Jones, Arjun Rana, Jared J. Lodico, Weikun Xiao, B. C. Regan, and Jianwei Miao. In situ coherent diffractive imaging. Nature Communications, (9):1826, 2018.

[137] D. Russell Luke. Relaxed averaged alternating reflections for diffraction imaging. Inverse Problems, 21:37–50, 2005.

[138] J. J. Macklin, J. D. Kmetec, and C. L. Gordon III. High-Order Harmonic Generation Using Intense Femtosecond Pulses. Physical Review Letters, 70(6):766–769, 1993.

[139] A. M. Maiden, M. J. Humphry, and J. M. Rodenburg. Ptychographic transmission microscopy in three dimensions using a multi-slice approach. Journal of the Optical Society of America A, 29(8):1606–1614, 2012.

[140] A. M. Maiden, M. J. Humphry, M. C. Sarahan, B. Kraus, and J. M. Rodenburg. An annealing algorithm to correct positioning errors in ptychography. Ultramicroscopy, 120:64–72, 2012.

[141] Andrew Maiden, Daniel Johnson, and Peng Li. Further improvements to the ptychographical iterative engine. Optica, 4(7):736–745, 2017.

[142] Andrew M. Maiden, Martin J. Humphry, Fucai Zhang, and John M. Rodenburg. Superresolution imaging via ptychography. Journal of the Optical Society of America A, 28(4):604–612, 2011.

[143] Andrew M. Maiden and John M. Rodenburg. An improved ptychographical phase retrieval algorithm for diffractive imaging. Ultramicroscopy, 109:1256–1262, 2009.

[144] T. H. Maiman. Optical and microwave-optical experiments in ruby. Physical Review Letters, 4(11):564–566, 1960.

[145] P. Maine, D. Strickland, P. Bado, M. Pessot, and G. Mourou. Generation of Ultrahigh Peak Power Pulses by Chirped Pulse Amplification. IEEE Journal of Quantum Electronics, 24(2):398–403, 1988.

[146] Giulia F. Mancini, Robert M. Karl Jr., Elisabeth R. Shanblatt, Charles S. Bevis, Dennis F. Gardner, Michael D. Tanksalvala, Jennifer L. Russell, Daniel E. Adams, Henry C. Kapteyn, John V. Badding, Thomas E. Mallouk, and Margaret M. Murnane. Colloidal crystal order and structure revealed by tabletop extreme ultraviolet scattering and coherent diffractive imaging. Optics Express, 26(9):11393–11406, 2018.

[147] Giulia Fulvia Mancini, Tatiana Latychevskaia, Francesco Pennacchio, Javier Reguera, Francesco Stellacci, and Fabrizio Carbone. Order/Disorder Dynamics in a Dodecanethiol-Capped Gold Nanoparticles Supracrystal by Small-Angle Ultrafast Electron Diffraction. Nano Letters, 16:2705–2713, 2016.

[148] Shashidhara Marathe, S. S. Kim, S. N. Kim, Chan Kim, H. C. Kang, P. V. Nickles, and D. Y. Noh. Coherent diffraction surface imaging in reflection geometry. Optics Express, 18(7):7253–7262, 2010.

[149] E. A. J. Marcatili and R. A. Schmeltzer. Hollow Metallic and Dielectric Waveguides for Long Distance Optical Transmission and Lasers. The Bell System Technical Journal, 43:1783–1809, 1964.

[150] S. Marchesini, H. He, H. N. Chapman, S. P. Hau-Riege, A. Noy, M. R. Howells, U. Weierstall, and J. C. H. Spence. X-ray image reconstruction from a diffraction pattern alone. Physical Review B, 68:140101, 2003.

[151] Stefano Marchesini. Phase retrieval and saddle-point optimization. Journal of the Optical Society of America A, 24(10):3289–3296, 2007.

[152] J. Maser, G. B. Stephenson, S. Vogt, W. Yun, A. Macrander, H. C. Kang, C. Liu, and R. Conley. Multilayer Laue lenses as high-resolution x-ray optics. Proceedings of SPIE, 5539:185–194, 2004.

[153] B. C. McCallum and J. M. Rodenburg. Two-dimensional demonstration of Wigner phase-retrieval microscopy in the STEM configuration. Ultramicroscopy, 45:371–380, 1992.

[154] F. J. McClung and R. W. Hellwarth. Giant Optical Pulsations from Ruby. Journal of Applied Physics, 33(3):828–829, 1962.

[155] Ian McNulty, Janos Kirz, Chris Jacobsen, Erik H. Anderson, Malcolm R. Howells, and Dieter P. Kern. High-Resolution Imaging by Fourier Transform X-ray Holography. Science, 256:1009–1012, 1992.

[156] A. McPherson, G. Gibson, H. Jara, U. Johann, T. S. Luk, I. A. McIntyre, K. Boyer, and C. K. Rhodes. Studies of multiphoton production of vacuum-ultraviolet radiation in the rare gases. Journal of the Optical Society of America B, 4(4):595–601, 1987.

[157] J.-M. Meijer, A. Shabalin, R. Dronyak, O. M. Yefanov, A. Singer, R. P. Kurta, U. Lorenz, O. Gorobstov, D. Dzhigaev, J. Gulden, D. V. Byelov, A. V. Zozulya, M. Sprung, I. A. Vartanyants, and A. V. Petukhov. Double hexagonal close-packed structure revealed in a single colloidal crystal grain by Bragg rod analysis. Journal of Applied Crystallography, 47:1199–1204, 2014.

[158] J. Miao and D. Sayre. On possible extensions of X-ray crystallography through diffraction-pattern oversampling. Acta Crystallographica, 56:596–605, 2000.

[159] J. Miao, D. Sayre, and H. N. Chapman. Phase retrieval from the magnitude of the Fourier transforms of nonperiodic objects. Journal of the Optical Society of America A, 15(6):1662–1669, 1998.

[160] Jianwei Miao, Pambos Charalambous, Janos Kirz, and David Sayre. Extending the methodology of X-ray crystallography to allow imaging of micrometre-sized non-crystalline specimens. Nature, 400:342–344, 1999.

[161] Jianwei Miao, Tetsuya Ishikawa, Erik H. Anderson, and Keith O. Hodgson. Phase retrieval of diffraction patterns from noncrystalline samples using the oversampling method. Physical Review B, 67:174104, 2003.

[162] Jianwei Miao, Tetsuya Ishikawa, Ian K. Robinson, and Margaret M. Murnane. Beyond crystallography: Diffractive imaging using coherent x-ray light sources. Science, 348(6234):530–535, 2015.

[163] Jianwei Miao, Tetsuya Ishikawa, Qun Shen, and Thomas Earnest. Extending X-Ray Crystallography to Allow the Imaging of Noncrystalline Materials, Cells, and Single Protein Complexes. Annual Review of Physical Chemistry, 59:387–410, 2008.

[164] Jianwei Miao, Richard L. Sandberg, and Changyong Song. Coherent X-Ray Diffraction Imaging. IEEE Journal on Selected Topics in Quantum Electronics, 18(1):399–410, 2012.

[165] R. P. Millane and W. J. Stroud. Reconstructing symmetric images from their undersampled Fourier intensities. Journal of the Optical Society of America A, 14(3):568–579, 1997.

[166] Kathryn Ann Moler. Imaging quantum materials. Nature Materials, 16:1049–1052, 2017.

[167] Peter Moulton. Ti-doped sapphire: tunable solid-state laser. Optics News, 8:9, 1982.

[168] D. Nardi, F. Banfi, C. Giannetti, B. Revaz, G. Ferrini, and F. Parmigiani. Pseudo-surface acoustic waves in hypersonic surface phononic crystals. Physical Review B, 80:104119, 2009.

[169] Damiano Nardi, Marco Travagliati, Mark E. Siemens, Qing Li, Margaret M. Murnane, Henry C. Kapteyn, Gabriele Ferrini, Fulvio Parmigiani, and Francesco Banfi. Probing Thermomechanics at the Nanoscale: Impulsively Excited Pseudosurface Acoustic Waves in Hypersonic Phononic Crystals. Nano Letters, 11:4126–4133, 2011.

[170] Georges Ndabashimiye, Shambhu Ghimire, Mengxi Wu, Dana A. Browne, Kenneth J. Schafer, Mette B. Gaarde, and David A. Reis. Solid-state harmonics beyond the atomic limit. Nature, 534:520–523, 2016.

[171] B. Niemann, D. Rudolph, and G. Schmahl. X-ray microscopy with synchrotron radiation. Applied Optics, 15(8):1883–1884, 1976.

[172] Michal Odstrčil, Mirko Holler, and Manuel Guizar-Sicairos. Arbitrary-path fly-scan ptychography. Optics Express, 26(10):12585–12593, 2018.

[173] Yasumasa Okada and Yozo Tokumaru. Precise determination of lattice parameter and thermal expansion coefficient of silicon between 300 and 1500 K. Journal of Applied Physics, 56:314–320, 1984.

[174] Xingchen Pan, Cheng Liu, and Jianqiang Zhu. Single shot ptychographical iterative engine based on multi-beam illumination. Applied Physics Letters, 103:171105, 2013.

[175] Ariel Paul, Emily A. Gibson, Xiaoshi Zhang, Amy Lytle, Tenio Popmintchev, Xibin Zhou, Margaret M. Murnane, Ivan P. Christov, and Henry C. Kapteyn. Phase-Matching Techniques for Coherent Soft X-Ray Generation. IEEE Journal of Quantum Electronics, 42(1):14–26, 2006.

[176] P. M. Paul, E. S. Toma, P. Breger, G. Mullot, F. Augé, Ph. Balcou, H. G. Muller, and P. Agostini. Observation of a Train of Attosecond Pulses from High Harmonic Generation. Science, 292:1689–1692, 2001.

[177] Philipp M. Pelz, Manuel Guizar-Sicairos, Pierre Thibault, Ian Johnson, Mirko Holler, and Andreas Menzel. On-the-fly scans for X-ray ptychography. Applied Physics Letters, 105:251101, 2014.

[178] M. Pessot, P. Maine, and G. Mourou. 1000 Times Expansion/Compression of Optical Pulses for Chirped Pulse Amplification. Optics Communications, 62(6):419–421, 1987.

[179] Mark A. Pfeifer, Garth J. Williams, Ivan A. Vartanyants, Ross Harder, and Ian K. Robinson. Three-dimensional mapping of a deformation field inside a nanocrystal. Nature, 442:63–66, 2006.

[180] Tenio Popmintchev, Ming-Chang Chen, Paul Arpin, Margaret M. Murnane, and Henry C. Kapteyn. The attosecond nonlinear optics of bright coherent X-ray generation. Nature Photonics, 4:822–832, 2010.

[181] Tenio Popmintchev, Ming-Chang Chen, Dimitar Popmintchev, Paul Arpin, Susannah Brown, Skirmantas Ališauskas, Giedrius Andriukaitis, Tadas Balčiunas, Oliver D. Mücke, Audrius Pugzyls, Andrius Baltuška, Bonggu Shim, Samuel E. Schrauth, Alexander Gaeta, Carlos Hernández-García, Luis Plaja, Andreas Becker, Agnieszka Jaron-Becker, Margaret M. Murnane, and Henry C. Kapteyn. Bright Coherent Ultrahigh Harmonics in the keV X-ray Regime from Mid-Infrared Femtosecond Lasers. Science, 336:1287–1291, 2012.

[182] Christina L. Porter, Michael Tanksalvala, Michael Gerrity, Galen Miley, Xiaoshi Zhang, Charles Bevis, Elisabeth Shanblatt, Robert Karl, Jr., Margaret M. Murnane, Daniel E. Adams, and Henry C. Kapteyn. General-purpose, wide field-of-view reflection imaging with a tabletop 13 nm light source. Optica, 4(12):1552–1557, 2017.

[183] Dieter M. Profunser, Oliver B. Wright, and Osamu Matsuda. Imaging Ripples on Phononic Crystals Reveals Acoustic Band Structure and Bloch Harmonics. Physical Review Letters, 97:055502, 2006.

[184] Jayaraman Rajeswari, Ping Huang, Giulia Fulvia Mancini, Yoshie Murooka, Tatiana Latychevskaia, Damien McGrouther, Marco Cantoni, Edoardo Baldini, Jonathan Stuart White, Arnaud Magrez, Thierry Giamarchi, Henrik Moodysson Rønnow, and Fa Carbone. Filming the formation and fluctuation of skyrmion domains by cryo-Lorentz transmission electron microscopy. Proceedings of the National Academy of Sciences, 112(46):14212–14217, 2015.

[185] Arjun Rana, Jianhua Zhang, Minh Pham, Andrew Yuan, Yuan Hung Lo, Huaidong Jiang, Stanley Osher, and Jianwei Miao. Potential of attosecond coherent diffractive imaging. arXiv preprint, arXiv:1907, 2019.

[186] H. Rarback, D. Shu, S. C. Feng, H. Ade, J. Kirz, I. McNulty, D. P. Kern, T. H. P. Chang, Y. Vladimirsky, N. Iskander, D. Attwood, K. McQuaid, and S. Rothman. Scanning x-ray microscope with 75-nm resolution. Review of Scientific Instruments, 59(1):52–59, 1988.

[187] Laura Rego, Kevin M. Dorney, Nathan J. Brooks, Quynh L. Nguyen, Chen-Ting Liao, Julio San Román, David E. Couch, Allison Liu, Emilio Pisanty, Maciej Lewenstein, Luis Plaja, Henry C. Kapteyn, Margaret M. Murnane, and Carlos Hernández-García. Generation of extreme-ultraviolet beams with time-varying orbital angular momentum. Science, 364(6447):eaaw9486, 2019.

[188] Mark A. Robertson, Sean Borman, and Robert L. Stevenson. Estimation-theoretic approach to dynamic range enhancement using multiple exposures. Journal of Electronic Imaging, 12(2):219–228, 2003.

[189] I. K. Robinson, J. L. Libbert, I. A. Vartanyants, J. A. Pitney, D. M. Smilgies, D. L. Abernathy, and G. Grübel. Coherent x-ray diffraction imaging of silicon oxide growth. Physical Review B, 60(14):9965–9972, 1999.

[190] I. K. Robinson, I. A. Vartanyants, G. J. Williams, M. A. Pfeifer, and J. A. Pitney. Reconstruction of the Shapes of Gold Nanocrystals Using Coherent X-Ray Diffraction. Physical Review Letters, 87(19):195505, 2001.

[191] J. M. Rodenburg. Ptychography and Related Diffractive Imaging Methods. Advances in Imaging and Electron Physics, 150:87–184, 2008.

[192] J. M. Rodenburg. Ptychography: early history and 3D scattering effects. Short-Wavelength Imaging and Spectroscopy Sources, 8678:867809, 2012.

[193] J. M. Rodenburg and R. H. T. Bates. The theory of super-resolution electron microscopy via Wigner-distribution deconvolution. Philosophical Transactions of the Royal Society A, 339:521–553, 1992.

[194] J. M. Rodenburg and H. M. L. Faulkner. A phase retrieval algorithm for shifting illumination. Applied Physics Letters, 85(20):4795–4797, 2004.

[195] Jose A. Rodriguez, Riu Xu, Chien-Chun Chen, Zhifeng Huang, Huaidong Jiang, Allan L. Chen, Kevin S. Raines, Alan Pryor Jr, Daewoong Nam, Lutz Wiegart, Changyong Song, Anders Madsen, Yuriy Chushkin, Federico Zontone, Peter J. Bradley, and Jianwei Miao. Three-dimensional coherent X-ray diffractive imaging of whole frozen-hydrated cells. IUCrJ, 2:575–583, 2015.

[196] W. C. Röntgen. On a new kind of rays. Nature, 53(1369):274–276, 1896.

[197] S. Roy, D. Parks, K. A. Seu, R. Su, J. J. Turner, W. Chao, E. H. Anderson, S. Cabrini, and S. D. Kevan. Lensless X-ray imaging in reflection geometry. Nature Photonics, 5:243–245, 2011.

[198] Andy Rundquist, Charles G. Durfee III, Zenghu Chang, Catherine Herne, Sterling Backus, Margaret M. Murnane, and Henry C. Kapteyn. Phase-Matched Generation of Coherent Soft X-rays. Science, 280:1412–1415, 1998.

[199] Jennifer L. Russell, Grace H. Noel, Joseph M. Warren, Ngoc-Lan L. Tran, and Thomas E. Mallouk. Binary Colloidal Crystal Films Grown by Vertical Evaporation of Silica Nanoparticle Suspensions. Langmuir, 33:10366–10373, 2017.

[200] Anne Sakdinawat and David Attwood. Nanoscale X-ray imaging. Nature Photonics, 4:840–848, 2010.

[201] J. V. Sanders. Diffraction of Light by Opals. Acta Crystallographica, 24:427–434, 1968.

[202] G. Sansone, E. Benedetti, F. Calegari, C. Vozzi, L. Avaldi, R. Flammini, L. Poletto, P. Villoresi, C. Altucci, R. Velotta, S. Stagira, S. De Silvestri, and M. Nisoli. Isolated Single-Cycle Attosecond Pulses. Science, 314:443–446, 2006.

[203] D. Sayre. Some implications of a theorem due to Shannon. Acta Crystallographica, 5:843, 1952.

[204] M. Ya. Schelev, M. C. Richardson, and A. J. Alcock. Image-converter streak camera with picosecond resolution. Applied Physics Letters, 18(8):354–357, 1971.

[205] G. Schmahl and D. Rudolph. Lichtstarke Zonenplatten als abbildende Systeme für weiche Röntgenstrahlung. Optik, 29(6):577–585, 1969.

[206] M. A. Schroer, C. Gutt, and G. Grübel. Characteristics of angular cross correlations studied by light scattering from two-dimensional microsphere films. Physical Review E, 90:012309, 2014.

[207] K. Schwarzschild. Untersuchungen zur geometrischen Optik. II. Theorie der Spiegeltelescope. Astronomische Mittheilungen der Königlichen Sternwarte zu Göttingen, 10:3–28, 1905.

[208] Matthew D. Seaberg, Bosheng Zhang, Dennis F. Gardner, Elisabeth R. Shanblatt, Margaret M. Murnane, Henry C. Kapteyn, and Daniel E. Adams. Tabletop Nanometer Extreme Ultraviolet Imaging in an Extended Reflection Mode using Coherent Fresnel Ptychography. Optica, 1(1):39–44, 2014.

[209] J. Seres, E. Seres, A. J. Verhoef, G. Tempea, C. Streli, P. Wobrauschek, V. Yakovlev, A. Scrinzi, C. Spielmann, and F. Krausz. Source of coherent kiloelectronvolt X-rays. Nature, 433:596, 2005.

[210] Claude E. Shannon. Communication in the Presence of Noise. Proceedings of the IRE, 37(1):10–21, 1949.

[211] David Shapiro, Pierre Thibault, Tobias Beetz, Veit Elser, Malcolm Howells, Chris Jacobsen, Janos Kirz, Enju Lima, Huijie Miao, Aaron M. Neiman, and David Sayre. Biological imaging by soft x-ray diffraction microscopy. Proceedings of the National Academy of Sciences, 102(43):15343–15346, 2005.

[212] Xiaowen Shi, Nicolas Burdet, Darren Batey, and Ian Robinson. Multi-Modal Ptychography : Recent Developments and Applications. Applied Sciences, 8:1054, 2018.

[213] Kei Shimomura, Makoto Hirose, and Yukio Takahashi. Multislice imaging of integrated circuits by precession X-ray ptychography. Acta Crystallographica, 74:66–70, 2018.

[214] Pavel Sidorenko and Oren Cohen. Single-shot ptychography. Optica, 3(1):9–14, 2016.

[215] Mark E. Siemens, Qing Li, Margaret M. Murnane, Henry C. Kapteyn, Ronggui Yang, Erik H. Anderson, and Keith A. Nelson. High-frequency surface acoustic wave propagation in nanostructures characterized by coherent extreme ultraviolet beams. Applied Physics Letters, 94:093103, 2009.

[216] Mark E. Siemens, Qing Li, Ronggui Yang, Keith A. Nelson, Erik H. Anderson, Margaret M. Murnane, and Henry C. Kapteyn. Quasi-ballistic thermal transport from nanoscale interfaces observed using ultrafast coherent soft X-ray beams. Nature Materials, 9:26–30, 2010.

[217] Neil J. A. Sloane. Kepler 's Conjecture Confirmed. Nature, 395:435–436, 1998.

[218] A. Snigirev, V. Kohn, I. Snigireva, and B. Lengeler. A compound refractive lens for focusing high-energy X-rays. Nature, 384:49–51, 1996.

[219] A. Snigirev, V. Kohn, I. Snigireva, A. Souvorov, and B. Lengeler. Focusing high-energy x rays by compound refractive lenses. Applied Optics, 37(4):653–662, 1998.

[220] Changyong Song, Damien Ramunno-Johnson, Yoshinori Nishino, Yoshiki Kohmura, Tetsuya Ishikawa, Chien-Chun Chen, Ting-Kuo Lee, and Jianwei Miao. Phase retrieval from exactly oversampled diffraction intensity through deconvolution. Physical Review B, 75:012102, 2007.

[221] D. E. Spence, P. N. Kean, and W. Sibbett. 60-fsec pulse generation from a self-mode-locked Ti:sapphire laser. Optics Letters, 16(1):42–44, 1991.

[222] Ch. Spielmann, N. H. Burnett, S. Sartania, R. Koppitsch, M. Schnürer, C. Kan, M. Lenzner, P. Wobrauschek, and F. Krausz. Generation of Coherent X-rays in the Water Window Using 5-Femtosecond Laser Pulses. Science, 278:661–664, 1997.

[223] Andreas Stein and Rick C. Schroden. Colloidal crystal templating of three-dimensionally ordered macroporous solids: materials for photonics and beyond. Current Opinion in Solid State and Materials Science, 5:553–564, 2001.

[224] N. Streibl. Phase imaging by the transport equation of intensity. Optics Communications, 49(1):6–10, 1984.

[225] Donna Strickland and Gerard Mourou. Compression of Amplified Chirped Optical Pulses. Optics Communications, 56(3):219–221, 1985.

[226] Tao Sun, Zhang Jiang, Joseph Strzalka, Leonidas Ocola, and Jin Wang. Three-dimensional coherent X-ray surface scattering imaging near total external reflection. Nature Photonics, 6:586–590, 2012.

[227] Akihiro Suzuki, Shin Furutaku, Kei Shimomura, Kazuto Yamauchi, Yoshiki Kohmura, Tetsuya Ishikawa, and Yukio Takahashi. High-Resolution Multislice X-Ray Ptychography of Extended Thick Objects. Physical Review Letters, 112:053903, 2014.

[228] Zhensheng Tao, Cong Chen, Tibor Szilvási, Mark Keller, Manos Mavrikakis, Henry Kapteyn, and Margaret Murnane. Direct time-domain observation of attosecond final-state lifetimes in photoemission from solids. Science, 353(6294):62–67, 2016.

[229] Michael Reed Teague. Deterministic phase retrieval: a Green's function solution. Journal of the Optical Society of America, 73(11):1434–1441, 1983.

[230] Phoebe Tengdin, Wenjing You, Cong Chen, Xun Shi, Dmitriy Zusin, Yingchao Zhang, Christian Gentry, Adam Blonsky, Mark Keller, Peter M. Oppeneer, Henry C. Kapteyn, Zhensheng Tao, and Margaret M. Murnane. Critical behavior within 20fs drives the out-of-equilibrium laser-induced magnetic phase transition in nickel. Science Advances, 4(eaap9744), 2018.

[231] U. Teubner and P. Gibbon. High-order harmonics from laser-irradiated plasma surfaces. Reviews of Modern Physics, 81:445–479, 2009.

[232] P. Thibault and M. Guizar-Sicairos. Maximum-likelihood refinement for coherent diffractive imaging. New Journal of Physics, 14:063004, 2012.

[233] Pierre Thibault, Martin Dierolf, Oliver Bunk, Andreas Menzel, and Franz Pfeiffer. Probe retrieval in ptychographic coherent diffractive imaging. Ultramicroscopy, 109:338–343, 2009.

[234] Pierre Thibault, Martin Dierolf, Andreas Menzel, Oliver Bunk, Christian David, and Franz Pfeiffer. High-resolution scanning x-ray diffraction microscopy. Science, 321:379–382, 2008.

[235] Pierre Thibault and Andreas Menzel. Reconstructing state mixtures from diffraction measurements. Nature, 494(7435):68–71, 2013.

[236] Samuel T. Thurman and James R. Fienup. Phase retrieval with signal bias. Journal of the Optical Society of America A, 26(4):1008–1014, 2009.

[237] August Toepler. Beobachtungen nach einer neuen optischen Methode ein Beitrag zur Experimental-Physik. Max Cohen & Sohn, Bonn, 1864.

[238] Emrah Turgut, Chan La-o-vorakiat, Justin M. Shaw, Patrik Grychtol, Hans T. Nembach, Dennis Rudolf, Roman Adam, Martin Aeschlimann, Claus M. Schneider, Thomas J. Silva, Margaret M. Murnane, Henry C. Kapteyn, and Stefan Mathias. Controlling the Competition between Optically Induced Ultrafast Spin-Flip Scattering and Spin Transport in Magnetic Multilayers. Physical Review Letters, 110:197201, 2013.

[239] A. Ulvestad, A. Singer, J. N. Clark, H. M. Cho, J. W. Kim, R. Harder, J. Maser, Y. S. Meng, and O. G. Shpyrko. Topological defect dynamics in operando battery nanoparticles. Science, 348(6241):1344–1347, 2015.

[240] Orlin D. Velev and Eric W. Kaler. Structured Porous Materials via Colloidal Crystal Templating: From Inorganic Oxides to Metals. Advanced Materials, 12(7):531–534, 2000.

[241] Adriaan Walther. The Question of Phase Retrieval in Optics. Optica Acta: International Journal of Optics, 10(1):41–49, 1963.

[242] Alan J. Walton. The Abbe theory of imaging: an alternative derivation of the resolution limit. European Journal of Physics, 7:62–63, 1986.

[243] R. F. Wang, C. Nisoli, R. S. Freitas, J. Li, W. McConville, B. J. Cooley, M. S. Lund, N. Samarth, C. Leighton, V. H. Crespi, and P. Schiffer. Artificial 'spin ice' in a geometrically frustrated lattice of nanoscale ferromagnetic islands. Nature, 439:303–306, 2006.

[244] L. W. Whitehead, G. J. Williams, H. M. Quiney, D. J. Vine, R. A. Dilanian, S. Flewett, K. A. Nugent, A. G. Peele, E. Balaur, and I. McNulty. Diffractive Imaging Using Partially Coherent X Rays. Physical Review Letters, 103:243902, 2009.

[245] R. N. Wilke, M. Priebe, M. Bartels, K. Giewekemeyer, A. Diaz, P. Karvinen, and T. Salditt. Hard X-ray imaging of bacterial cells : nano-diffraction and ptychographic reconstruction. Optics Express, 20(17):19232–19254, 2012.

[246] G. J. Williams, M. A. Pfeifer, I. A. Vartanyants, and I. K. Robinson. Three-Dimensional Imaging of Microstructure in Au Nanocrystals. Physical Review Letters, 90(17):175501, 2003.

[247] G. J. Williams, H. M. Quiney, B. B. Dahl, C. Q. Tran, A. G. Peele, K. A. Nugent, M. D. De Jonge, and D. Paterson. Curved beam coherent diffractive imaging. Thin Solid Films, 515:5553–5556, 2007.

[248] G. J. Williams, H. M. Quiney, B. B. Dhal, C. Q. Tran, K. A. Nugent, A. G. Peele, D. Paterson, and M. D. de Jonge. Fresnel coherent diffractive imaging. Physical Review Letters, 97:025506, 2006.

[249] Garth J. Williams, Harry M. Quiney, Andrew G. Peele, and Keith A. Nugent. Coherent diffractive imaging and partial coherence. Physical Review B, 75:104102, 2007.

[250] Peter Wochner, Miguel Castro-Colin, Stephanie N. Bogle, and Volodymyr N. Bugaev. Of fluctuations and cross-correlations: finding order in disorder. International Journal of Materials Research, 102(7):874–888, 2011.

[251] Peter Wochner, Christian Gutt, Tina Autenrieth, Thomas Demmer, Volodymyr Bugaev, Alejandro Díaz Ortiz, Agnès Duri, Federico Zontone, Gerhard Grübel, and Helmut Dosch. X-ray cross correlation analysis uncovers hidden local symmetries in disordered matter. Proceedings of the National Academy of Sciences, 106(28):11511–11514, 2009.

[252] Hans Wolter. Spiegelsysteme streifenden Einfalls als abbildende Optiken für Röntgenstralen. Annalen der Physik, 10:94–114, 1952.

[253] Amnon Yariv. Internal Modulation in Multimode Laser Oscillators. Journal of Applied Physics, 36(2):388–391, 1964.

[254] Gung-Chian Yin, Yen-Fang Song, Mau-Tsu Tang, Fu-Rong Chen, Keng S. Liang, Frederick W. Duewer, Michael Feser, Wenbing Yun, and Han-Ping D. Shieh. 30 nm resolution x-ray imaging at 8 keV using third order diffraction of a zone plate lens objective in a transmission microscope. Applied Physics Letters, 89:221122, 2006.

[255] Xianghui Zeng, Fred Duewer, Michael Feser, Carson Huang, Alan Lyon, Andrei Tkachuk, and Wenbing Yun. Ellipsoidal and parabolic glass capillaries as condensers for x-ray microscopes. Applied Optics, 47(13):2376–2381, 2008.

[256] Ahmed H. Zewail. Femtochemistry atomic-scale dynamics of the chemical bond using ultrafast lasers. Nobel Lecture, pages 274–367, 1999.

[257] Bosheng Zhang, Dennis F. Gardner, Matthew D. Seaberg, Elisabeth R. Shanblatt, Henry C. Kapteyn, Margaret M. Murnane, and Daniel E. Adams. High contrast 3D imaging of surfaces near the wavelength limit using tabletop EUV ptychography. Ultramicroscopy, 158:98–104, 2015.

[258] Bosheng Zhang, Dennis F. Gardner, Matthew H. Seaberg, Elisabeth R. Shanblatt, Christina Porter, Robert Karl Jr., Christopher A. Mancuso, Henry C. Kapteyn, Margaret M. Murnane, and Daniel E. Adams. Ptychographic hyperspectral spectromicroscopy with an extreme ultraviolet high harmonic comb. Optics Express, 24(16):18745–18754, 2016.

[259] Fucai Zhang, Isaac Peterson, Joan Vila-Comamala, Ana Diaz, Felisa Berenguer, Richard Bean, Bo Chen, Andreas Menzel, Ian K. Robinson, and John M. Rodenburg. Translation position determination in ptychographic coherent diffraction imaging. Optics Express, 21(11):13592–13606, 2013.

[260] Nikolay I. Zheludev. The Road Ahead for Metamaterials. Science, 328:582–583, 2010.

[261] J. Zhou, J. Peatross, M. M. Murnane, H. C. Kapteyn, and I. P. Christov. Enhanced High-Harmonic Generation Using 25 fs Laser Pulses. Physical Review Letters, 76(5):752–755, 1996.

[262] J. M. Zuo, I. Vartanyants, M. Gao, R. Zhang, and L. A. Nagahara. Atomic Resolution Imaging of a Carbon Nanotube from Diffraction Intensities. Science, 300(5624):1419–1421, 2003.

[263] Michael Zürch, Christian Kern, and Christian Spielmann. XUV coherent diffraction imaging in reflection geometry with low numerical aperture. Optics Express, 21(18):21131–21147, 2013.